

Summer 8-15-2017

MRI in Cancer: Improving Methodology for Measuring Vascular Properties and Assessing Radiation Treatment Effects in Brain

Chong Duan

Washington University in St. Louis

Follow this and additional works at: https://openscholarship.wustl.edu/art_sci_etds



Part of the [Chemistry Commons](#)

Recommended Citation

Duan, Chong, "MRI in Cancer: Improving Methodology for Measuring Vascular Properties and Assessing Radiation Treatment Effects in Brain" (2017). *Arts & Sciences Electronic Theses and Dissertations*. 1237.
https://openscholarship.wustl.edu/art_sci_etds/1237

This Dissertation is brought to you for free and open access by the Arts & Sciences at Washington University Open Scholarship. It has been accepted for inclusion in Arts & Sciences Electronic Theses and Dissertations by an authorized administrator of Washington University Open Scholarship. For more information, please contact digital@wumail.wustl.edu.

WASHINGTON UNIVERSITY IN ST. LOUIS

Department of Chemistry

Dissertation Examination Committee:

Joseph JH Ackerman, Chair

Joel R Garbow, Co-Chair

Alexander B Barnes

Dewey Holten

Christina I Tsien

MRI in Cancer: Improving Methodology for Measuring Vascular Properties and Assessing
Radiation Treatment Effects in Brain

by

Chong Duan

A dissertation presented to
The Graduate School
of Washington University in
partial fulfillment of the
requirements for the degree
of Doctor of Philosophy

August 2017
St. Louis, Missouri

© 2017, Chong Duan

Table of Contents

List of Figures	v
List of Tables	viii
Acknowledgments.....	ix
Abstract	xii
Chapter 1 Introduction.....	1
1.1 Motivation	1
1.2 State of Research.....	2
1.2.1 Magnetic Resonance Imaging Basics.....	2
1.2.2 Tumor Vasculature.....	9
1.2.3 MRI in Characterizing Tumor Vasculature.....	10
1.2.4 Radiation Treatment Effects	17
1.2.5 MRI in Characterizing Radiation Treatment Effects	23
1.3 Dissertation Overview	24
1.4 References	25
Chapter 2 Tracer Kinetic Model Selection in Dynamic-Contrast Enhanced MRI.....	29
2.1 Introduction	29
2.2 Methods.....	31
2.2.1 The DCE-MRI tracer kinetic models	31
2.2.2 Clinical DCE-MRI data	34
2.2.3 <i>In silico</i> DCE-MRI data	35
2.2.4 Bayesian-based model selection (and parameter estimation)	38
2.2.5 Statistical analysis	41
2.3 Results	41
2.4 Discussion	47
2.5 Acknowledgements	53
2.6 References	53
Chapter 3 Modeling Dynamic-Contrast Enhanced MRI data with a Constrained Local Arterial Input Function.....	59
3.1 Introduction	59
3.2 Materials and Methods	61

3.2.1	Clinical DCE-MRI Data.....	61
3.2.2	<i>In silico</i> DCE-MRI Data	62
3.2.3	DCE-MRI tracer kinetic modeling.....	63
3.2.4	A gamma-variate local-AIF model	64
3.2.5	A constrained local-AIF model.....	65
3.2.6	Data analysis	68
3.2.7	Bayesian model selection.....	69
3.3	Results	71
3.4	Discussion	76
3.5	Acknowledgements	81
3.6	References	81
Chapter 4	Anti-VEGF Treatment of Frank Radiation-Induced Necrosis in Brain.....	84
4.1	Introduction	84
4.2	Material and methods	85
4.2.1	Animal Model	85
4.2.2	Magnetic Resonance Imaging	86
4.2.3	Data Analysis	87
4.2.4	Histology and IHC	88
4.3	Results	89
4.4	Discussion	93
4.5	Acknowledgements	96
4.6	References	97
Chapter 5	Irradiated Brain Parenchyma Promotes Enhanced Tumor Growth and Invasion in a Mouse Model of Recurrent Glioblastoma.....	100
5.1	Introduction	100
5.2	Methods and Materials	101
5.3	Results	104
5.4	Discussion	108
5.5	Acknowledgments	111
5.6	References	111
Chapter 6	Summary and Future Research	114
6.1	Summary	114

6.2	Future Research.....	115
6.3	References	118
Appendix A: Hyperthermic Laser Ablation of Recurrent Glioblastoma Leads to Temporary Disruption of the Peritumoral Blood Brain Barrier		
		119
A.1	Introduction	119
A.2	Material and methods	122
A.3	Results	127
A.3.1	Patient characteristics and treatment course	127
A.3.2	Quantitative measurement of LITT-induced peritumoral BBB disruption by DCE-MRI	129
A.3.3	Quantitative measurement of LITT-induced peritumoral BBB disruption by serum BSE biomarker	133
A.4	Discussion	137
A.5	Acknowledgements	138
A.6	References	139
Appendix B: Effects of Off-Resonance on T_1 Saturation Recovery Measurement in inhomogeneous field.....		
		142
B.1	Introduction	142
B.2	Theory	144
B.2.1	Spin Dynamics in homogeneous field.....	144
B.2.2	Spin Dynamics in inhomogeneous field	145
B.3	Numerical Procedures	151
B.4	Experimental procedure	153
B.5	Results	154
B.5.1	Numerical and Analytical Results.....	154
B.5.2	Experimental Results	163
B.6	Discussion and Conclusions.....	167
B.7	References	170

List of Figures

Figure 1.1: Illustration of free induction decay and the generation of MR signal.....	4
Figure 1.2: Illustration of longitudinal relaxation post-RF disturbance of the thermal equilibrium condition.	6
Figure 1.3: Spin echo sequence showing the timing of each RF and gradient pulse.....	7
Figure 1.4: Structures, chemical and commercial names of four commonly used Gd-based MR contrast agents.....	9
Figure 1.5: Example transaxial, pre- and post-contrast, T_1 -weighted images collected for a healthy subject (left and middle panels), and for a patient diagnosed with glioblastoma (yellow arrow in the right panel).....	12
Figure 1.6: Dynamic contrast-enhanced MR images for brain tumor.	14
Figure 1.7: The vascular damage hypothesis of radiation necrosis development.....	21
Figure 2.1: Hierarchy of the four compartmental tracer kinetic models and their corresponding model parameters.	32
Figure 2.2: Example DCE-MRI contrast agent concentration vs. time curves.....	35
Figure 2.3: Range of kinetic parameter values	37
Figure 2.4: Distribution of baseline signals.	38
Figure 2.5: Bayesian DCE-MRI model-selection and parameter-estimation.	43
Figure 2.6: Pooled model selection results for in silico datasets created for each of the four DCE models.	44
Figure 2.7: Pooled model selection results for in silico datasets created for the 2CXM only.....	46
Figure 2.8: Bayesian DCE-MRI model selection results for a cohort of cervical cancer patients.	46
Figure 2.9: Pharmacokinetic parameters estimated using the optimal DCE-MRI kinetic models for all subjects.	47
Figure 2.10: Parametric estimates (left map of each pair) and corresponding uncertainties (right map of each pair).	48
Figure 3.1: Representative R-AIF and cL-AIF.	67

Figure 3.2: Simulation study comparing the accuracy and precision of CTUM parameter estimation.	72
Figure 3.3: Comparison of the use of R-AIF vs. ul-AIF vs. cL-AIF in modeling of a representative dataset.	73
Figure 3.4: Parametric maps (left map of each pair) and corresponding uncertainty maps.	75
Figure 3.5: Estimations of the delay time and scaling factor, and model selection.....	76
Figure 3.6: Modeling of a representative cervical cancer DCE-MRI dataset employing three AIFs.....	77
Figure 4.1: Illustration of the Gamma Knife irradiation scheme.....	86
Figure 4.2: Anti-VEGF treatment response detected by anatomic MRI.	90
Figure 4.3: Anti-VEGF treatment response detected by diffusion-weighted MRI.....	91
Figure 4.4: Anti-VEGF treatment as shown by H&E.....	92
Figure 4.5: Anti-VEGF treatment response as shown by immunohistochemistry.	93
Figure 5.1: Representative, post-contrast, transaxial T1-weighted images of mice with DBT tumors post-implantation day 17.	105
Figure 5.2: Prior Radiation Impacts Tumor Growth and Mouse Survival.	106
Figure 5.3: Prior irradiation of the brain with 30 Gy (middle column) or 40 Gy (right column) of GK radiation has a substantial effect on tumor growth patterns and progression histologically, compared to the control, non-irradiated brain (left column).....	108
Figure A.1: Consort flow diagram of the BBB disruption measurement portion of the pilot phase 2 study involving the first 20 enrolled patients.....	124
Figure A.2: Radiographic appearances of post-LITT changes.	131
Figure A.3: K^{trans} for each of the 14 included subjects in the study as a function of time in days from the LITT procedure.	133
Figure A.4: Optimization of the BSE ELISA assay for measuring BBB disruption.....	134
Figure A.5: BBB disruption induced by LITT as measured by serum biomarkers.	136
Figure B.1: Saturation – recovery pulse sequence considered in this study.....	144

Figure B.2: Effective weighting function $g(\omega_0)$ given in Eq.[8] for two different choices of amplitude extraction: (A) matched filter and (B) peak detection.	149
Figure B.3: Simulated spectra of longitudinal magnetization, M_z , at the end of the first CPMG sequence, normalized by the thermal magnetization M_0 for different normalized durations of the first CPMG sequence, N_{1tE}/T_2 as indicated.....	155
Figure B.4: Spectra of longitudinal magnetization, M_z , at the end of the first CPMG sequence, calculated from the analytical expression.	156
Figure B.5: Echo shapes and amplitudes as a function of $T_w = T_1$, $N_{1tE}=T_2$, and method of amplitude extraction.....	157
Figure B.6: Effect of phase alternation (PA) on echo shapes and amplitudes.....	159
Figure B.7: Spectra of normalized longitudinal magnetization at the end of first CPMG sequence for different T_1/T_2 ratio as indicated.	161
Figure B.8: Dependence of ϵ and $1/\epsilon$ on T_1/T_2	162
Figure B.9: Evaluation of the proposed new T_1 kernel (Equations 11 and 17) for various values of N_{1tE}/T_2 (Panel a) and T_1/T_2 (Panel b) in the presence of significant off-resonant effect. ..	163
Figure B.10: Comparison between experimentally measured and numerically simulated echoes for both frequency domain (left panel) and time domain (right panel).	164
Figure B.11: Experimental results for standard saturation-recovery measurement for doped water: measured in-phase components of echoes (left) and extracted echo amplitude using matched filtering (right) for different recovery wait time T_w (T_w/T_1 in the range of 0.01 to 5). ..	165
Figure B.12: The effect of phase alternation (PA) on the shape of the echoes at short wait times.	166
Figure B.13: Saturation recovery measurements for DI H_2O , $NiCl_2$ -doped H_2O , and skim milk.	167

List of Tables

Table 1.1: Relaxation time constants for various tissues at 1.5 T.....	5
Table 2.1: Impulse response functions for the four tracer kinetic models.....	33
Table 2.2: Prior ranges for all the parameters within the response functions.....	41
Table 3.1: Summary of Parameters Used in the cL-AIF Model.	65
Table A.1: Patient Baseline Demographics and Characteristics.....	128
Table B.1: Calculated values of α_1 and α_2	158
Table B.2: Effect of phase alternation of excitation pulse.....	160
Table B.3: Experimentally determined relaxation times for the three samples.....	164

Acknowledgments

Pursuing a Ph.D. 7492.92 miles from home is a tough road. Many people collectively have made the odyssey possible and worthwhile.

First, I would like to gratefully acknowledge my two advisors, Professors Joseph J.H. Ackerman and Joel R. Garbow, for their time, talents, patience and never-ending optimism. Without their guidance, this research would not have been possible. For many years to come the inspirations they have rendered to me will last.

The Biomedical Magnetic Resonance Laboratory (BMRL) affords a stimulating, challenging and also enjoyable research environment to work in. I thank Professor G. Larry Bretthorst for his help on Bayesian analysis with Markov chain Monte Carlo simulation. I thank Professors William Spees and James Quirk for their help on the Varian MRI system. I thank John A. Engelbach for his help on small-animal operations. Many thanks go to my fellow students and postdocs in BMRL, both past and current, for their help and friendship: Scott C. Beeman, Carlos J. Perez-Torres, Xiaoyu Jiang, Tsen-Hsuan (Abby) Lin, Donghan (Mo) Yang, Yue Zhao, Chenchen Liu, Biao Xiang, Ruimeng (Karen) Yang, Xia Ge, Cihat Eldeniz and Kelsey Meinerz.

I thank Professor Richard Loomis for interviewing me in 2012 and offering me the opportunity to pursue my graduate study at Washington University. I thank Dr. Kit Mao for her confidence in my qualification as a Teaching Assistant, even if I didn't get an adequate score in the English language exam when I first came to Saint Louis. I thank Robert Massa and Rachel Dunn for helping me to maneuver the less scientific side of my graduate study.

I would also like to thank my Dissertation Advisory and Examination Committee members: Professors Alexander B. Barnes, Dewey Holten, and Christina I. Tsien for their insightful

comments on my research, and for their reviews and edits of this dissertation. Many thanks go to my collaborators who have contributed to this dissertation. They are Christina I. Tsien, Keith M. Rich, Liya Yuan, Robert E. Schmidt, Joshua S. Shimony, Eric C. Leuthardt, David D. Tran, Jesper F. Kallehauge, and Kari Tanderup. I worked as a summer intern at Schlumberger-Doll Research in 2016. I thank my internship mentor and colleagues: Martin D. Hürlimann, Yi-Qiao Song, Shin Utsuzawa, and Yiqiao (Ray) Tang for helping me acquire knowledge in the oil & gas industry.

This thesis has been supported by NIH grant R01 CA155365 (JRG) and funding from the Alvin J. Siteman Cancer Center (NIH P30 CA91842). I acknowledge travel and educational support from the International Society of Magnetic Resonance in Medicine (ISMRM), the Gordon Research Conference (GRC), and the Practical Application of Nuclear magnetic resonance in Industry Conference (PANIC). I also acknowledge financial support from the Arts & Sciences Graduate School for my Dean's Dissertation Fellowship.

Finally, I would like to thank my family for their unyielding support throughout this endeavor. To them I owe my passion in life. Special thanks to Kesai for her exceptional cooking skills and continuous confidence in me.

This thesis is dedicated to my grandfather who had always been hoping to see me obtain the first doctorate degree in our family. If you can see this from heaven, I hope I am making you proud.

Chong Duan

Washington University in St. Louis

August 2017

Dedicated to my grandfather.

ABSTRACT OF THE DISSERTATION

MRI in Cancer: Improving Methodology for Measuring Vascular Properties and Assessing
Radiation Treatment Effects in Brain

by

Chong Duan

Doctor of Philosophy in Chemistry

Washington University in St. Louis, 2017

Professor Joseph J.H. Ackerman, Chair

Professor Joel R. Garbow, Co-Chair

Tumors cannot survive, progress and metastasize without recruiting new blood vessels. Vascular properties, including perfusion and permeability, provide valuable information for characterizing cancers and assessing therapeutic outcomes. Dynamic contrast-enhanced (DCE) MRI is a non-invasive imaging technique that affords quantitative parameters describing the underlying vascular structure of tissue. To date, the clinical application of DCE-MRI has been hampered by the lack of standardized and validated quantitative modeling approaches for data analysis.

From a therapeutic perspective, radiation therapy is a central component of the standard treatment for patients with cancer. Besides killing cancer cells, radiation also induces parenchymal and stromal changes in normal tissue, limiting radiation dose and complicating treatment response evaluation. Further, emerging evidence suggest that the radiation-modulated tumor microenvironment may also contribute to the enhanced tumor regrowth and resistance to therapy.

Given these clinical problems, the objectives of this dissertation were to: i) improve the DCE MRI-based measurements of vascular properties; and ii) assess the radiation treatment effects on normal

tissue (parenchyma) and the interaction between radiation-modulated parenchyma and tumor growth. For the first goal, Bayesian probability theory-based model selection was employed to evaluate four commonly employed DCE-MRI tracer kinetic models against both *in silico* DCE-MRI data and high-quality clinical data collected from patients with advanced-staged cervical cancer. Further, a constrained local arterial input function (cL-AIF) modeling approach was developed to improve the pharmacokinetic analysis of DCE-MRI data. For the second goal, a novel mouse model of radiation-mediated effects on normal brain was developed. The efficacy of anti-vascular endothelial growth factor (VEGF) antibody treatment of delayed, radiation-induced necrosis (RN) was evaluated. Also, the effects of radiation-modulated brain parenchyma on glioblastoma cell growth were studied.

It was found that 1) complex DCE-MRI signal models are more sensitive to noise than simpler models with respect to parameter estimation accuracy and precision. Caution is thus advised when considering application of complex DCE-MRI kinetic models. It follows that data-driven model selection is an important prerequisite to DCE-MRI data analysis; 2) the proposed cL-AIF method, which estimates an unique local-AIF amplitude and arrival time for each voxel within the tissue of interest, provides better measurements vascular properties than the conventional approach employing a single, remotely measured AIF; 3) anti-VEGF antibody decreased MR-derived RN lesion volumes, while large areas of focal calcification formed and the expression of VEGF remained high post-treatment. More effective therapeutic strategies for RN are still needed; 4) the radiation-modulated brain parenchyma promotes aggressive, infiltrative glioma growth. The histologic features of such tumors are consistent with those commonly observed in recurrent high-grade tumors in patients. These findings afford new insights into the highly aggressive tumor regrowth patterns observed following radiotherapy.

Chapter 1 Introduction

1.1 Motivation

Approximately 50% of all cancer patients receive radiotherapy during the course of their illness (1). It has been widely recognized that tumor response to radiation is determined not only by a tumor cell's phenotype, but also by its vascular properties (2). Thus, the temporal and spatial variations in vascular structure and pathology can provide valuable information on tumor characteristics and potential responses to therapeutics, leading to an increasing use of medical imaging in evaluating tumor vascularity. Among potential imaging methods, dynamic-contrast enhanced (DCE) magnetic resonance imaging (MRI), which monitors the pharmacokinetics of administrated paramagnetic contrast agents, has the unique advantages of wide availability without using ionizing radiation (3). Nevertheless, the extracted vascular parameters from DCE-MRI data depend heavily on the pharmacokinetic modeling approach, which is often complicated by the high heterogeneity of cancer tissues.

As a cancer treatment, radiotherapy has been classically viewed as exerting its therapeutic effect by killing tumor cells, though emerging evidence indicates that these effects extend beyond cancer cell death. Radiation induces vascular, stromal and immunological changes in the tumor microenvironment (4), leading to various treatment effects ranging from minimal change with no observable clinical symptoms to delayed devastating radiation necrosis. The radiotherapy-mediated effects on normal tissue limit the dose of radiation that can be used in cancer treatment, promotes, and complicates the diagnosis of, subsequent loco-regional tumor recurrence (5).

The objectives of this dissertation are thus twofold: 1) to improve DCE-MRI-based measurements of tumor vascular properties; 2) to assess the radiation-induced modulations on normal tissue, and

determine how those changes affect tumor recurrence, and evaluate possible therapeutic agents for the treatment of radiation effects.

1.2 State of Research

1.2.1 Magnetic Resonance Imaging Basics

Nuclear Spin

In classic physics, a rotating object possesses a property known as angular momentum. In quantum mechanics, particles (e.g., electrons, protons and whole nuclei) possess the inherent property of spin or spin angular momentum. The spin angular momentum is an intrinsic quantized property of particles, and can be described by a magnitude L and a direction m :

$$L = \frac{h}{2\pi} \sqrt{I(I+1)}$$

$$m = -I, -I+1, -I+2, \dots +I$$

where h is the Planck constant and I is the nuclear spin quantum number. The projection of the spin angular momentum on the z-axis (arbitrarily chosen) is then given by $m \frac{h}{2\pi}$. The spin quantum number takes values of the form $N/2$, where N can be any non-negative integer. The spin quantum number of ^1H , the most common signal source in MRI experiment, is $1/2$. This means the proton has two possible spin directions/states, $m = -1/2$ or $+1/2$. In the absence of an applied magnetic field, the two proton spin states are degenerate (i.e., they have the same energy). The application of an external magnetic field, \vec{B}_0 (assuming to be along the z-axis), splits the degenerate energy levels, and the resulting energy gap is given by:

$$\Delta E = \gamma h |\vec{B}_0|$$

where γ is the gyromagnetic ratio ($\gamma = 42.58 \text{ MHz T}^{-1}$ for ^1H). According to the Boltzmann statistical distribution, the population ratio of the two states (parallel vs. anti-parallel to the field) is determined by:

$$\frac{N_{anti-parallel}}{N_{parallel}} = e^{-\frac{\Delta E}{kT}}$$

in which $N_{anti-parallel}$ and $N_{parallel}$ represent the population of nuclei in the corresponding state, k is the Boltzmann constant, and T is the absolute temperature. More spins are in the lower energy state, which is parallel to the field. As a result, the population difference between $N_{anti-parallel}$ and $N_{parallel}$ generates a net magnetization parallel to the applied field, which is the source of MR signal. Note that this population difference is extremely small (on the order of ppm) given the biologically relevant temperature and currently available superconducting magnetic field strength (i.e., $|\vec{B}_0|$).

Free Precession

Similar to the manner in which a spinning top precesses around the gravitational field, nuclear spin precesses about the external magnetic field at a frequency of $\omega_0 = \gamma|\vec{B}_0|$, also known as Larmor frequency. As discussed in the previous section, the energy splitting results in a net equilibrium magnetization M_0 along the z direction (assuming \vec{B}_0 is along the z -axis). When excited with a 90° , resonant, radiofrequency (RF) pulse that is perpendicular to \vec{B}_0 , this net magnetization will be flipped into the transverse plane. In terms of energy, nuclear spins in lower energy state absorb the RF energy (when on resonance, the RF energy, $h\nu$, equals the energy gap between the two states) and transits to the higher energy state, thus changing the overall net magnetization (equivalent to rotate/flip the net magnetization in the vector description). Immediately after this pulse, all the

spins are in phase and the net magnetization, M_0 (Figure 1.1), continues to precess around the \vec{B}_0 field in the transverse plane. When a detection/receiver coil is placed perpendicular to the z-axis, the precessing magnetization will induce an oscillating voltage in the coil. This time-domain electric signal (oscillating voltage) is then digitized and Fourier transformed to obtain the MR signal. This process is also known as free induction decay (FID). Figure 1.1 illustrates FID and the generation of MR signal.

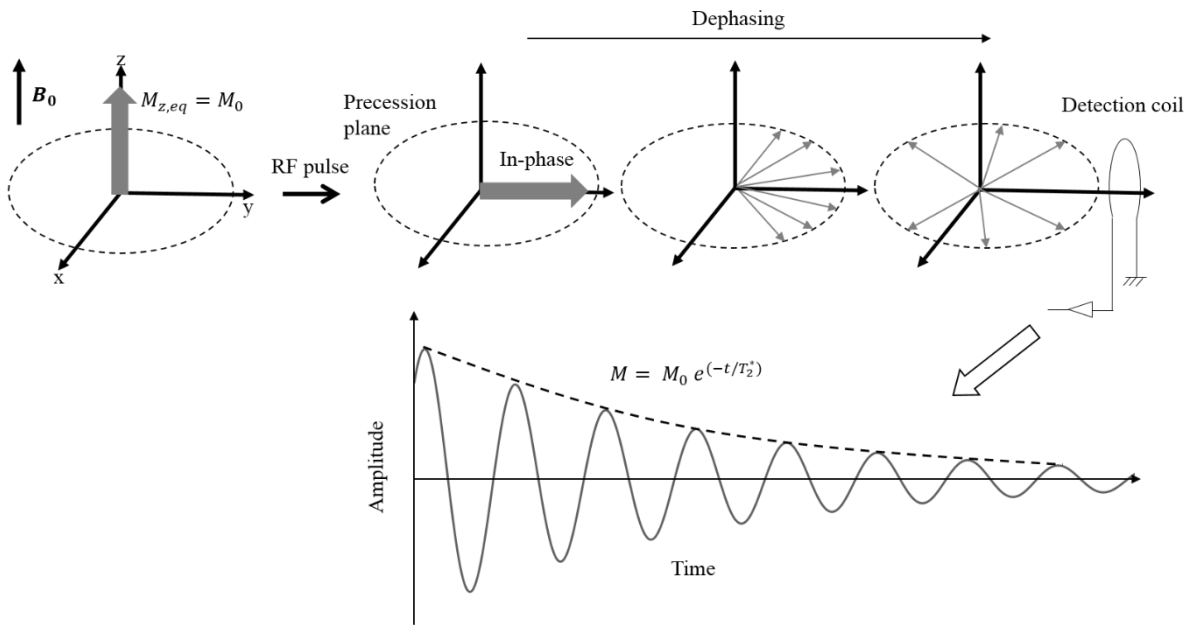


Figure 1.1: Illustration of free induction decay and the generation of MR signal.

Transverse Relaxation

Initially in phase (statistical phase coherence), the transverse components of magnetization, M_{xy} , begin to dephase as they precess about \vec{B}_0 following the 90° excitation pulse (Figure 1.1). This process is known as transverse relaxation. One of the most common contributions to this dephasing process is the local static field inhomogeneity, in addition to the main magnetic field \vec{B}_0 , experienced by a spin. Another major contribution to transverse relaxation occurs in a special form

of spin-spin coupling (flip-flop), in which a pair of spins simultaneously exchange their angular momentum (also known as spin diffusion). This results in no net longitudinal magnetization change but loss of phase coherence. The signal decay due to dephasing is conventionally described by an exponential curve, whose decay rate is characterized by the time constant T_2 , which is unique to every tissue (Table 1.1) and is determined primarily by its chemical/molecular environment, and is only weakly dependent on field strength. In practice, many experimental imperfections, such as imperfect shimming and field distortion resulting from air/tissue interfaces, create inhomogeneous magnetic fields that enhance the dephasing process. The sum total of all of these random and fixed effects is called T_2^* relaxation.

Table 1.1: Relaxation time constants for various tissues at 1.5 T

	T_1 (ms)	T_2 (ms)
Water	3000	3000
Gray matter	810	100
White matter	680	90
Liver	420	45
Fat	240	85

Longitudinal Relaxation

Longitudinal relaxation describes the process that a disturbed magnetization state returns/recovers back to the thermal equilibrium state *via* energy exchange (thermal mixing) between the spins and

the lattice. Taking the previous example, once the RF pulse is turned off, in addition to the free precession around B_0 and dephasing due to spin-spin relaxation, the energy absorbed by the excited spins is released back into the surrounding lattice (spin-lattice relaxation). This results in a recovery along the longitudinal direction to the initial thermal equilibrium condition (Figure 1.2). In many situations, this process can be described by a single exponential. The recovery rate is characterized by the time constant T_1 , which is unique to every tissue (Table 1.1) and varies with field strength. This time constant may also be affected by exogenous contrast agent tracers (*vide infra*).

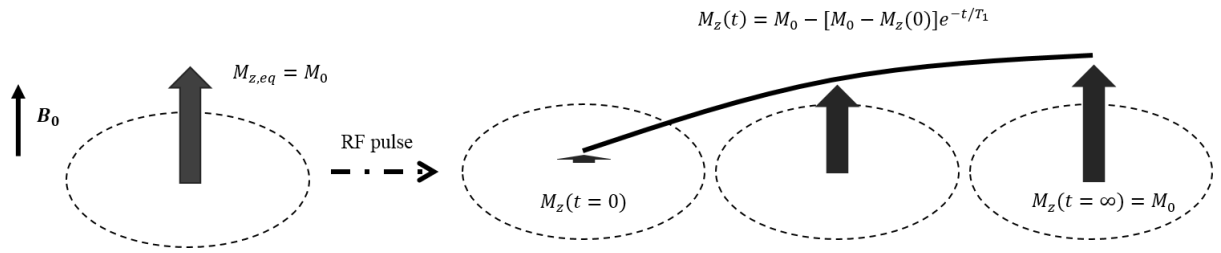


Figure 1.2: Illustration of longitudinal relaxation post-RF disturbance of the thermal equilibrium condition. $M_z(t=0)$ indicates the initial z -magnetization after the RF pulse, which equals zero for the case of 90° pulse.

Image Contrast

Endogenous Contrast: In conventional anatomic MRI, image contrast across tissues often arises directly from the tissue-specific relaxation time constants. For example, when a standard spin echo pulse sequence (Figure 1.3) is employed, the detected MR signal intensity is given by:

$$S = S_0 \cdot \exp\left(-\frac{TE}{T_2}\right) \cdot \left[1 - \exp\left(-\frac{TR}{T_1}\right)\right]$$

where S_0 is the proton density, TE is the echo time, and TR is the repetition time.

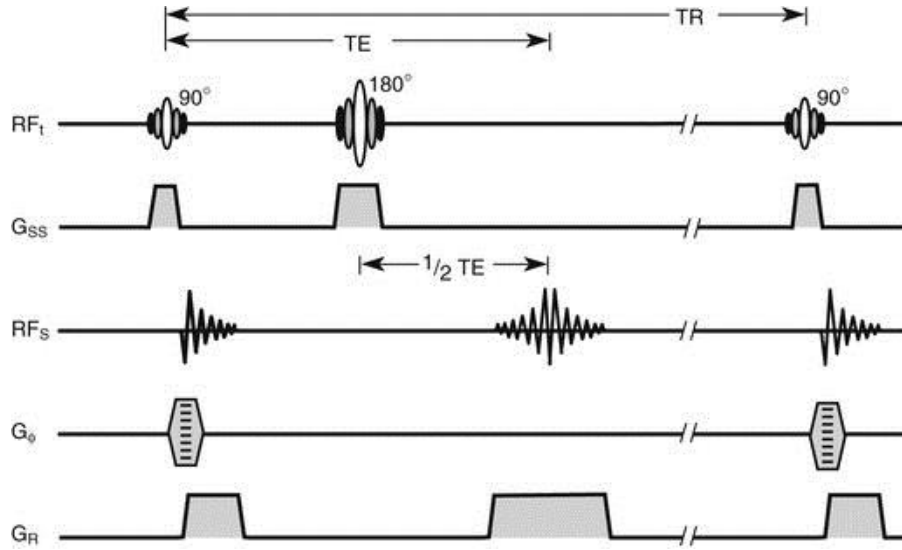


Figure 1.3: Spin echo sequence showing the timing of each RF and gradient pulse. RF_t and RF_s represent the transmitting RF pulses and received RF signal, respectively. G_{ss} , G_ϕ , and G_R represent the three gradients employed to encode spatial information.

This equation demonstrates that the detected MR signal for a specific type of tissue depends on its proton density and relaxation time constants (e.g., T_1 and T_2 for the case of spin echo sequence). Herein, T_1 -weighted, T_2 -weighted, and proton density (PD)-weighted (PD-weighted) images can be generated with an appropriate choice of TR and TE values. Short TR and short TE yield T_1 -weighted images; long TR and long TE yield T_2 -weighted images; long TR and short TE yield PD-weighted images.

Exogenous Contrast Agent: To further increase the imaging contrast between a tissue of interest and its surrounding tissue, exogenous MR contrast agents can be used. These contrast agents are often directly MR-invisible, but manifest their presence indirectly by enhancing the longitudinal relaxation (i.e., shorten the T_1) of nearby protons, thus increasing MR signal intensity in T_1 -weighted images. Most MR contrast agents are gadolinium (Gd)-based complexes (Figure 1.4). Gd is strongly paramagnetic, since it possesses seven unpaired electrons in its 4f shell. It typically

exhibits nine coordination sites for bonding. As shown in Figure 1.4, a group of ligands occupies eight of these sites, and the ninth is occupied by water molecule. The water-molecule relaxation enhancement caused by Gd arises from the fluctuating dipolar interactions near the Larmor frequency, due to the thermal-induced tumbling of contrast molecules and their surrounding water molecules, between water protons and Gd electrons. This enhancement (i.e., the longitudinal relaxation time constant change, ΔT_1) depends on the contrast agent concentration, [CA], and relaxivity r_1 :

$$\frac{1}{\Delta T_1} = \Delta R_1 = r_1 \cdot [CA]$$

It is worthwhile to note that Gd also shortens water proton T_2 . However, for a typical dose used in the routine MR imaging experiments (~ 0.1 mmol/kg) and for a T_1 -weighted pulse sequence, the MR signal is often overwhelmed by the dominant T_1 -shortening.

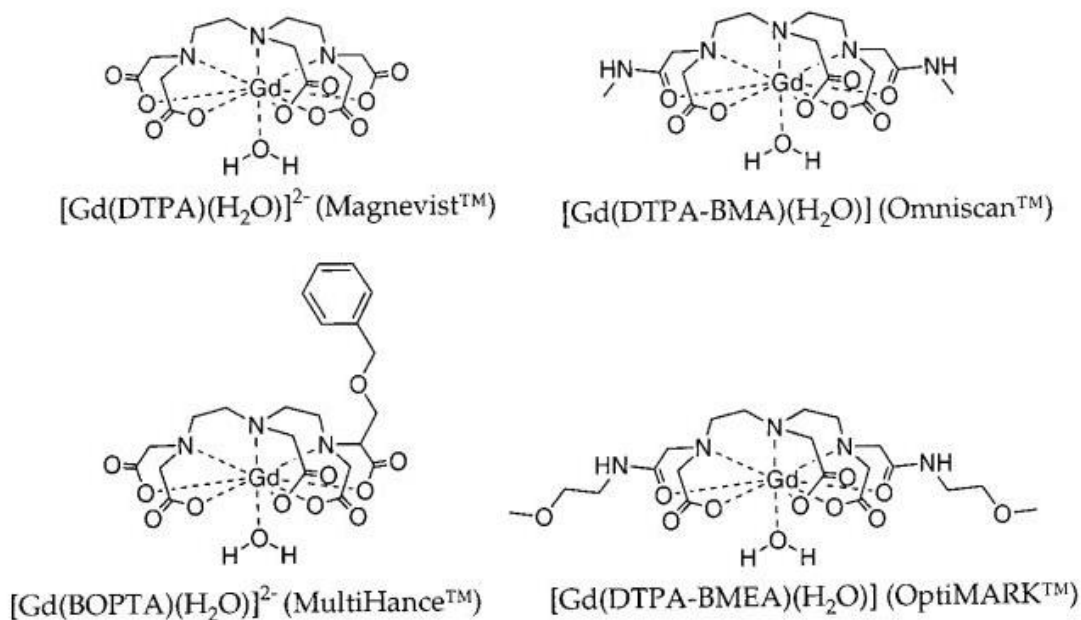


Figure 1.4: Structures, chemical and commercial names of four commonly used Gd-based MR contrast agents.

1.2.2 Tumor Vasculature

It is widely known that new blood vessels are normally formed by vasculogenesis, also referred as neovascularization, and angiogenesis, regulated by a balance between pro- and anti-angiogenic molecules. Vasculogenesis is the process of differentiation of precursor cells into endothelial cells and the *de novo* formation of a primitive vascular network, whereas angiogenesis is defined as the growth of new capillaries from pre-existing blood vessels (6). Tumor vessels mostly develop by sprouting from pre-existing vessels (i.e., angiogenesis). The circulating endothelial cells and precursors can also contribute to tumor angiogenesis (7). Various pro- and anti-angiogenesis molecules are involved in these mechanisms of vascular growth, including members of the vascular endothelial growth factor (VEGF) family and the VEGF-receptor family. The expression of these regulators are not as well coordinated, temporally and/or spatially, in tumors as in physiological angiogenesis, which results in structurally and functionally abnormal tumor vasculature (see below).

Chaotic Architecture and Blood Flow

When compared to normal vasculatures, tumor blood vessels are highly disorganized, tortuous, and have a haphazard interconnection. This is likely due to the spatial and temporal imbalance between pro- and anti-angiogenesis regulators as discussed in the previous section. As a result of the chaotic network structure, tumor blood flow is often highly inhomogeneous, and thus leads to local hypoxic and acidic (caused by acidic metabolites generated from anaerobic glycolysis in hypoxia) tumor regions. This explains the low therapeutic effectiveness due to the poor delivery of anti-cancer drugs, and motivates the large body of research focusing on “normalizing” the

abnormal structure and function of tumor blood vessels to make them more efficient for drug delivery (8).

High Vascular Permeability

Tumor blood vessels lack functional perivascular cells, which are necessary to protect vessels against environmental changes and provide mechanistic support (e.g., the pericytes within the blood brain barrier). Further, the tumor blood vessel wall is formed by an inhomogeneous layer of endothelial cells and has fenestrations and lacks a basement membrane. Consequently, these microstructural defects often lead to leaky tumor vasculature. However, it is worthwhile to note the high heterogeneity of tumor vessel leakiness over space and time, and some tumors may even have very low vascular permeability due to the overexpression anti-angiogenesis or underexpression of pro-angiogenesis regulators. Caution must be taken when designing and administering anti-cancer therapeutic drugs.

1.2.3 MRI in Characterizing Tumor Vasculature

The development of novel antivasular or antiangiogenic drugs has led to an increasing use of medical imaging in evaluating tumor vasculature. Several molecular and functional imaging techniques based on MRI (9), computed tomography (CT) (10) or positron emission tomography (PET) (11) have been developed to characterize the pathophysiologic changes of tumor vascular structure and functionality (12). Among these techniques, MRI-based methods have unique advantages including MRI's wide availability and lack of ionizing radiation. This section briefly reviews the commonly employed MRI methods for probing tumor vasculature.

Contrast-Enhanced T_1 -weighted MRI

As discussed in the previous section, Gd-based contrast agents shorten the T_1 of water protons that are accessible to the contrast agent. After intravenous injection, water-soluble Gd complexes initially distribute into the intravascular space and then rapidly diffuse across the capillary membranes into the extracellular extravascular space (i.e., interstitial space). Herein, highly perfused tissues appear bright on post-contrast T_1 -weighted images (i.e., short TR and short TE). Nevertheless, in the case of neuroimaging, there is no interstitial distribution of contrast agents due to the existence of blood brain barrier (BBB), which, when intact, is impermeable to the hydrophilic Gd chelates. As a result, only major blood vessels appear hyperintense on post-contrast T_1 -weighted images for brains. This is demonstrated in the left and middle panels of Figure 1.5.

Interestingly, for many brain pathologies (e.g., tumors and radiation-induced necrosis), the BBB is impaired and the vasculatures are leaky. Consequently, the injected contrast agent will leak out of the vasculature when it gets to the pathological tissue, resulting in a hyperintense lesion region (yellow arrow-head on Figure 1.5) on contrast-enhanced T_1 -weighted images. Herein, contrast-enhanced T_1 -weighted MRI is a commonly used technique to detect impaired vasculature, which is typical for most cancers and adjuvant treatment effects. In fact, a large number of studies have demonstrated the high sensitivity of contrast-enhanced T_1 -weighted images to the impaired vasculatures in various lesions (13,14).

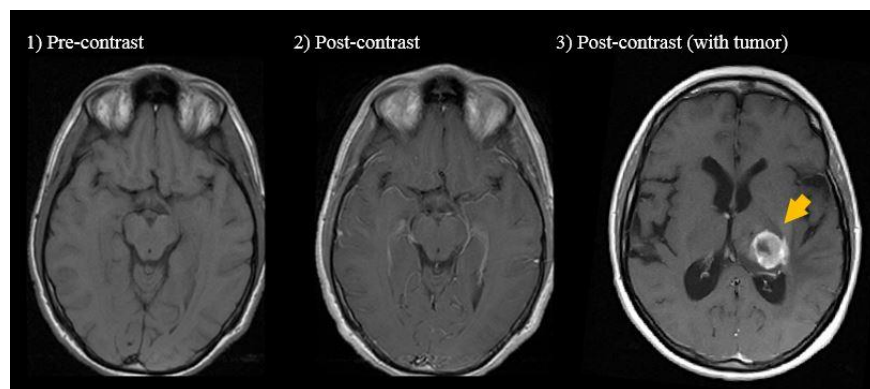


Figure 1.5: Example transaxial, pre- and post-contrast, T_1 -weighted images collected for a healthy subject (left and middle panels), and for a patient diagnosed with glioblastoma (yellow arrow in the right panel).

Dynamic Contrast-Enhanced (T_1 -weighted) MRI

Even though contrast-enhanced T_1 -weighted imaging is routinely used in the clinic, it only detects a steady-state MR signal enhancement for the tissue of interest. In other words, it only qualitatively describes the tissue vascularity (i.e., perfusion) and vascular permeability (BBB break down in the case of brain). Further, in contrast to the high sensitivity, the specificity is extremely poor. To address these problems, a highly quantitative method for characterizing tissue perfusion and vascular permeability is warranted.

Dynamic contrast-enhanced (DCE) MRI is a noninvasive quantitative method of investigating microvascular structure and function by tracking the tracer kinetics, also referred as pharmacokinetics, of a bolus of injected paramagnetic contrast agent as it passes through the lesion capillary bed. This technique is sensitive to alterations in vascular permeability, fractional interstitial and vascular volumes, and blood flow.

In DCE measurement, a series of T_1 -weighted images are acquired in rapid succession (on the order of seconds per image) following the intravenous administration of a Gd contrast agent bolus. Figure 1.6 illustrates examples of dynamic contrast-enhanced T_1 -weighted images and corresponding time courses acquired for a patient with malignant glioblastoma. Note the high enhancement of the tumor tissue due to the hyperpermeable BBB, compared to that of the contralateral healthy tissue.

Both semi-quantitative and quantitative analyses of the time-course DCE datasets have been used to derive information about tumor microcirculation and microvasculature. Semi-quantitative

analyses, which derive measures directly from MR signal intensities, depend on MR hardware and the pulse sequences used to acquire the data, making it challenging to compare results between studies. In addition, the derived parameters, including signal-intensity plateau, contrast-enhancement ratio, and area under the curve, have no clear physiological meaning. By contrast, quantitative analysis employing tracer kinetic models yields physiological parameters related to tissue perfusion and capillary permeability.

To quantitatively model time-resolved DCE dataset, a T_1 map must be constructed before contrast-agent administration, allowing conversion of DCE-MRI signal intensity into contrast-agent concentration. Tracer kinetic modeling of vascular leakage and conservation of mass allow the calculated tissue contrast-agent concentration, C_t , obtained following the administration of a contrast agent bolus, to be written as:

$$C_t(t) = C_p(t) \otimes I(t), \quad (1)$$

where $C_p(t)$ is the concentration of the contrast agent in the plasma of the capillary inlet of any region-of-interest (ROI), commonly approximated by a measured upstream arterial input function (AIF), and $I(t)$ is the tissue impulse-response function to the contrast agent input, which depends on the specific DCE-MRI tracer kinetic model. In this expression, " \otimes " denotes the convolution operation.

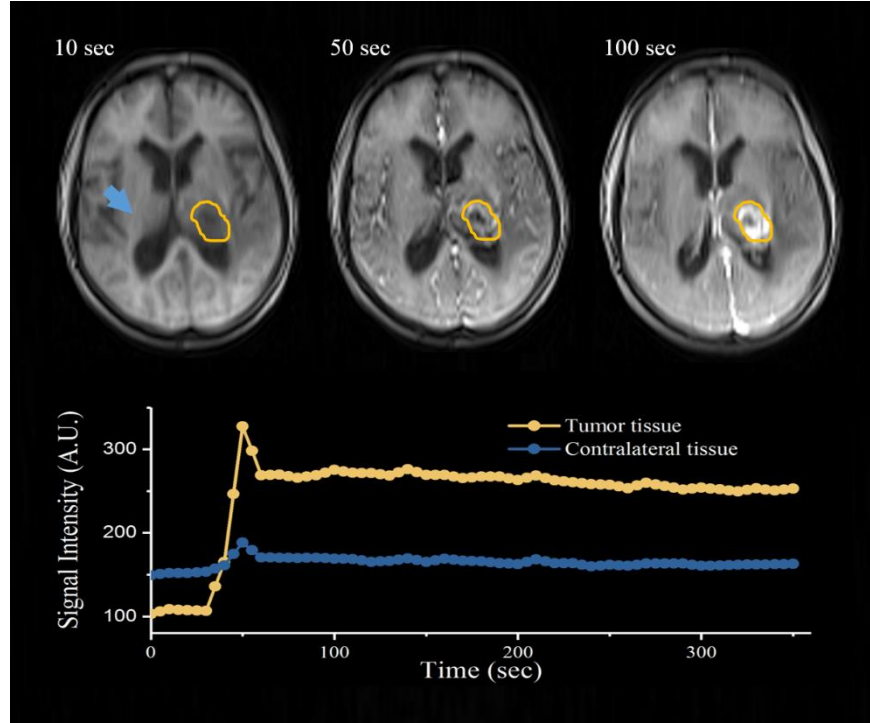


Figure 1.6: Dynamic contrast-enhanced MR images for brain tumor. The top row shows an example transaxial slice acquired at 10 sec, 50 sec, and 100 sec following the contrast agent administration. The bottom row demonstrates the signal intensity vs. time curves for tumor tissue (yellow) and healthy tissue (blue).

Since the proposal of the concept of dynamic MRI, many tracer kinetic models have been applied to describe the behavior of administered contrast agent in DCE-MRI experiments. The first generation of DCE-MRI models, including the widely used Tofts model (TM), was designed for tissues with negligible blood volume, and the models were used to characterize the permeability of the tissue vasculature. To account for intravascular signal contributions, the Extended Tofts Model (ETM) was introduced for highly-perfused tissues, including tumors. Improvements in scanner hardware and software, which have led to higher-quality DCE-MRI data, have motivated the development of models with greater complexity that more fully describe tissue perfusion and capillary permeability. Such models are physiologically more accurate (fewer assumptions/constraints regarding tissue structure) compared to reduced, simpler models that

make physiological assumptions or introduce constraints that may not be appropriate for the tissue of interest and will, thus, generate bias in kinetic parameter estimates. However, in practice, it remains unknown whether these more complex models are supported by a given clinical DCE-MRI dataset with specific data quality (e.g., time resolution, acquisition time window, and contrast-to-noise ratio (CNR)).

In addition to the determination of an optimal tracer kinetic model, quantitative analysis of DCE-MRI is challenging because of difficulties in obtaining an accurate and appropriate AIF for tracer kinetic modeling. Furthermore, given CA bolus delay and dispersion, and the structurally and functionally abnormal vasculature characteristic of cancer, a single remotely measured AIF is unlikely to approximate well the contrast agent input for every voxel within the tumor tissue. Further work on appropriate AIFs for voxel-wise tracer kinetic modeling of DCE-MRI data is still necessary.

Dynamic Susceptibility Contrast MRI

Dynamic Susceptibility Contrast (DSC) MRI relies on imaging the passage of a contrast agent bolus to measure perfusion. Similar to DCE-MRI, a bolus of gadolinium-based or superparamagnetic iron oxide particle contrast agent is injected intravenously in dynamic susceptibility contrast (DSC) MRI experiment, and rapid repeated imaging of the tissue of interest (TOI) is performed during the first pass of the contrast agent bolus. In contrast to the signal enhancement caused by the T_1 -shortening effect in DCE-MRI, DSC-MRI relies on the susceptibility induced signal loss on heavily T_2 - or T_2^* -weighted images (i.e., long TE) caused when the contrast agent bolus passes through the capillary bed of the tissue of interest.

One major caveat of DSC-MRI is that it is often difficult to distinguish changes in blood volume from changes in vascular permeability. In other words, for tissues with leaky vasculature, the extravasated contrast agent molecules will enhance the acquired MR signal by reducing T_1 of the extravascular water, which counteracts the susceptibility induced signal loss upon which the DSC experiment mainly relies. As a result, DSC-MRI is often used for perfusion measurements in brain tissue having an intact blood brain barrier (i.e., the blood vessels are not leaky when the BBB is intact). By performing pharmacokinetic analysis of the generated signal intensity vs. time curve, $S(t)$, several vascular parameters, including cerebral blood volume (CBV), cerebral blood flow (CBF), and mean transit time (MTT), can be calculated (15):

$$C_T(t) = CBF \cdot \int_0^t e^{-\frac{t-\tau}{MTT}} C_a(\tau) d\tau$$

in which $C_a(t)$ is the arterial input function and $C_T(t)$ can be calculated *via* equation:

$$S(t) = S_0 \cdot \exp[-k \cdot C_T(t)]$$

Arterial Spin Labeling MRI

While DCE-MRI and DSC-MRI track the intravenously injected *exogenous* contrast agent, arterial spin labeling (ASL) MRI utilizes magnetically labelled endogenous blood water as a tracer (16), and is, thus, completely non-invasive. In ASL MRI, two images are collected: a blood-flow sensitized, or “labelled”, image and a “control” image, in which the static tissue signals are identical, but the magnetization of the inflowing blood differs. The signal difference between these two images, ΔM , directly reflects the local perfusion, because MR signal from the static tissue is completely eliminated. Saturation with a 90° RF pulse or inversion with a 180° RF pulse are both commonly employed as labeling methods. As ΔM is very small ($< 5\%$ of the total

signal), multiple repetitions are often necessary to ensure enough signal to noise ratio (SNR). In addition to the blood flow, the computed signal difference also depends on T_1 of the blood and the time interval between labelling and acquisition of the actual image.

1.2.4 Radiation Treatment Effects

Despite the new advances in oncology, including recent encouraging responses in a number of neoplasms to targeted and/or immune-modulated therapies, surgical resection combined with chemo-radiation remains the cornerstone of standard treatment for brain tumors. While radiotherapy has been classically viewed as exerting its therapeutic effect by killing tumor cells, emerging evidence indicates that these effects extend beyond cancer cell death. Despite the use of sophisticated, fractionated, high-dose radiation or radiosurgery methods designed to spare normal tissue (e.g., 3D conformal radiotherapy, intensity modulated radiation therapy and stereotactic body radiation therapy), various treatment side effects/complications, ranging from minimal change with no observable clinical symptoms, to delayed devastating effects, including radiation-induced necrosis and second malignancies (17), may occur depending on the type of the cancer and the tissue/organ affected. The following are brief discussions on 1) the radiation-modulated brain tumor microenvironment; and 2) radiation-induced necrosis in the brain.

Radiation-modulated Tumor Microenvironment

It is increasingly recognized that radiation affects not only tumor cells, but also the tumor microenvironment (TME), especially the tumor-associated microglia and macrophages (18), that may contribute significantly to the resistance and recurrence of gliomas (5). Irradiation induces vascular, stromal, and immunological changes in the TME that may enhance the migration and invasiveness of tumor cells (19). This section brief summaries the effects of radiation on vasculature, stroma, and the immune system.

Vasculature: Radiation induces direct endothelial cell dysfunction, which is characterized by increased permeability, detachment of pericytes from the underlying basement membrane, and decrease of vascular density. The impaired vasculature and decreased vascular density indicate that some parenchymal tissue is not well perfused, which leads to long-term post-irradiation hypoxia, inflammation and fibrosis. These radiation-induced vascular changes are dependent on total dose, fraction size, and the location of the tumor. In extreme cases, the late time-to-onset radiation necrosis, as described in the following section, eventually develops as a result of the radiation-induced vascular damage.

Immune System: Following radiotherapy, both direct (i.e., the damage is a result of the ionizing radiation itself) and indirect (i.e., damage is a result of the radiation-induced cellular changes, including reactive oxygen species) radiation effects activate inflammatory cytokine signaling and the recruitment of immune cells. An increase in the number of locally suppressive cells after radiotherapy (e.g., tumor-associated macrophages, myeloid-derived suppressor cells, and regulatory T cells) is counterbalanced by the recruitment of circulating immune cells and increased antigen exposure. These changes affect the immune compartment of the TME in a complex manner, and may potentially prime the TME for an adaptive immune response, and contribute to radio-resistance and recurrence of tumor.

Stroma: Cancer-associated fibroblasts (CAFs) constitute the major cell type within the stroma in many cancers. In contrast to myofibroblasts that result from normal inflammation or wound healing processes, CAFs can be resistant to apoptosis and irreversibly activated (20). Hellevik, et al. (21) proposed that radiation induces increased integrin expression, and the formation of integrin-mediated attachments facilitates CAF survival following radiation therapy. Further, multiple preclinical studies have implicated $\beta 1$ integrin in tumor survival after radiation (22,23).

Therefore, malignancies with inherent radio-resistance may be due, in part, to the integrin-mediated interactions between tumor cells and the stromal cells.

Radiation-Induced Necrosis

A series of clinical syndromes/complications may occur following radiotherapy to the central nervous system (CNS). Based on the chronologic occurrence order, these complications are classified into three groups: 1) acute encephalopathy, due to disruption of the blood brain barrier; 2) early delayed complication, characterized by white matter injury; 3) radiation-induced necrosis (RN) that occur from months to decades from radiation treatment (24). Early effects are transient, and most of them resolve after a few weeks, while RN leads to irreversible, progressive damage to blood vessels with subsequent necrosis and white matter demyelination. It is worthwhile to note that the term “necrosis” is used loosely to refer to any vascular and parenchymal abnormalities that represents treatment effects rather than recurrent tumor. In the other words, pathology of RN is not limited to necrosis, but includes a spectrum of injury patterns. In the following, the pathophysiology and management of RN are reviewed.

Pathophysiology: The pathophysiology of RN remains incompletely understood. The current consensus views RN as a continuous, complex process from endothelial-cell dysfunction to tissue hypoxia and necrosis. Two major hypotheses have been proposed to explain the mechanism of RN following radiotherapy to the CNS. The first one postulates that RN arises from direct injury the glial cells of the brain parenchyma. This injury leads to secondary damage to the blood vessels, resulting in typical RN histopathological characteristics, including telangiectasia (small dilated blood vessels) and fibrinoid necrosis, a form of necrosis in which there is accumulation of amorphous, basic, proteinaceous material in tissue matrix. Nevertheless, this hypothesis is not supported by the observation that low-dose radiation, which can decrease the number of glial cells,

never induces RN in the brain (25). Consequently, the other hypothesis re direct injury to the blood vessels (i.e., the vascular hypothesis) has recently become increasingly widely supported.

In the vascular hypothesis (26), as shown in Figure 1.7, the first step in the development of RN following radiotherapy is direct blood vessel damage, which leads to hypoxia and ischemia in tissue within the irradiated field. As a result of the local hypoxia, hypoxia inducible factor-1 alpha (HIF-1 α) is upregulated. Since HIF-1 α is a widely known transactivator of vascular endothelial growth factor (VEGF) and the C-X-C motif chemokine 12 (CXCL12)/C-X-C chemokine receptor type 4 (CXCR4) signaling pathway, the expression of both VEGF and CXCR12 are augmented. Upregulated VEGF generates immature (leaky and fragile) neovascularization and results in subsequent perilesional edema and hemorrhage. On the other hand, CXCR12 expression attracts the CXCR4-expressing microglia and lymphocytes to the irradiated region, and produces a series of pro-inflammatory cytokines, including interleukin (IL)-1, IL-6, and tumor necrosis factor (TNF)- α . The resulting chronic inflammation within the irradiation field further contributes to the perilesional edema and, thus, aggregates radiation necrosis.

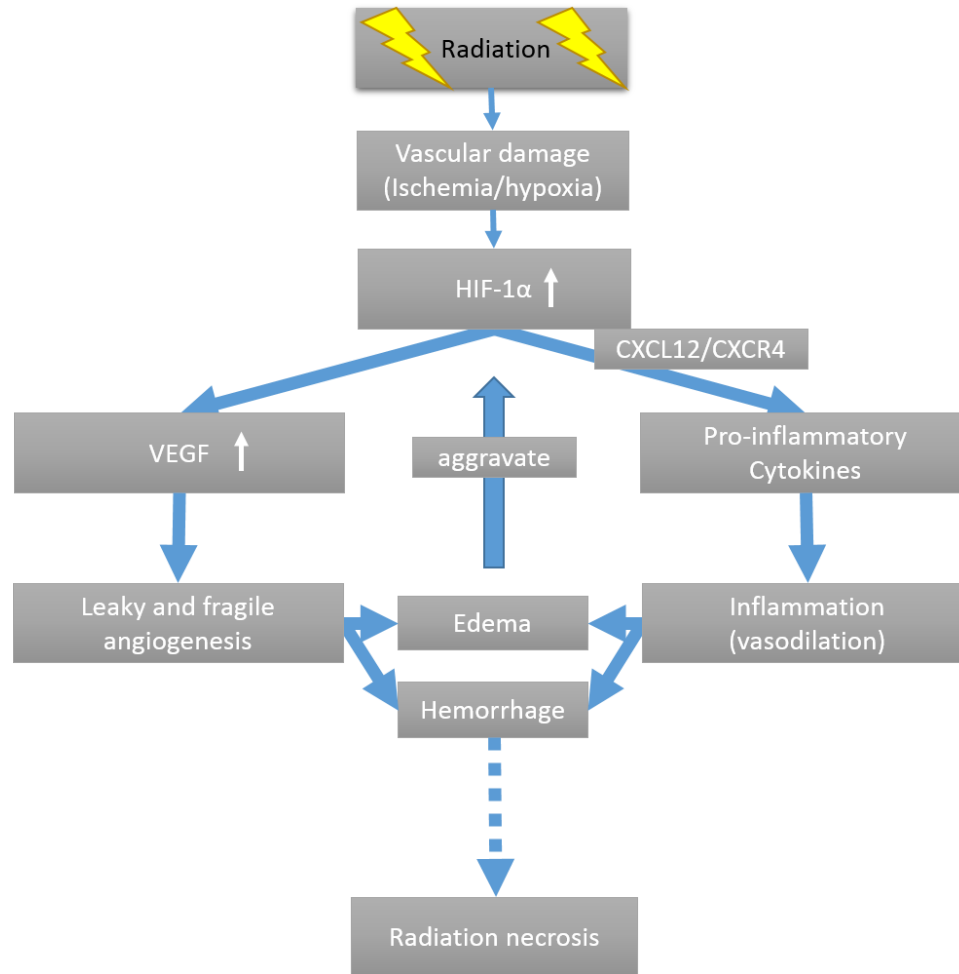


Figure 1.7: The vascular damage hypothesis of radiation necrosis development.

Management of RN: Surgical resection, MRI-guided laser interstitial thermal therapy, and medical treatments have been used to manage/mitigate RN following radiotherapy to the CNS. Currently, there is no well accepted standard of care for RN.

Surgical resection of necrotic tissue has been a gold-standard treatment of symptomatic RN. It reduces mass effect and edema, and lowers intracranial pressure, resulting in lasting clinical improvement in the majority of patients (27). Nevertheless, it is often not possible due to the location of the necrosis, as radiotherapy is often applied to surgically inaccessible lesions. Surgical

interventions in these regions may affect patients' neurological condition, and is reserved for use only if the lesion is refractory.

Laser interstitial thermal therapy (LITT) is a minimally invasive technique for treating “inoperable” primary and secondary brain tumors. It delivers focal laser energy selectively to the target tissue and exhibits a sharp ablation boundary zone. Recently, Rahmathulla et al. (28) and Smith et al. (29) reported the successfully use of LITT for the treatment of focal RN, and suggest that LITT may be an effective treatment modality for patients with medically refractory RN. However, these are both retrospective reports and a well-designed, randomized, double-blind study is necessary for the evaluation of the treatment efficacy.

Traditionally, RN has been treated with corticosteroids (30) to control edema and lessen inflammatory responses. However, the long-term use of corticosteroids is associated with chronic side effects, including hyperglycemia and immunosuppression. Anticoagulants agents (e.g., heparin and warfarin) (31) and hyperbaric oxygen therapy (32) have also been used in an attempt to heal microvasculature impairments and improve regional cerebral blood supply, but results have been inconsistent and disappointing (33). Recently, bevacizumab (Avastin[®], Genentech, San Francisco, CA), an anti-vascular endothelial growth factor (VEGF) antibody hypothesized to restore blood brain barrier (BBB) function and, thereby, to repair vascular leakage, has been reported to substantially decrease MR-derived RN lesion volume in the brain (33–35). Nevertheless, in the clinic it is generally not possible to correlate MR imaging result with gold-standard histology, and the possible complications of recurrent tumor. Therefore, further studies are still necessary to evaluate the treatment efficacy with gold-standard histology in animal models.

1.2.5 MRI in Characterizing Radiation Treatment Effects

Imaging radiation treatment effects poses a diagnostic challenge because of the possibility of disease/tumor progression post-therapy. Because of the equivocal conventional MR findings between recurrent tumor and radiation treatment effects, a spectrum of advanced techniques, including the MR methods for probing microvasculature introduced in the previous section, have been investigated. The following is an introduction to two other advanced MR techniques that are used in the diagnosis and characterization of radiation treatment effects. As MRI is not sensitive enough to detect the RT-induced cellular and molecular changes discussed previously in section 1.2.4, especially for those at the early stages, the following discussion will be limited to late time-to-onset radiation-induced necrosis.

Diffusion MRI

In biological tissue, structural barriers such as cell membranes and myelin can restrict the mobility of water molecules or favor the movement of water molecules in a specific direction. The magnitude and direction of water movement in tissue are quantified in diffusion MRI by calculating the apparent diffusion coefficient (ADC) for magnitude and the diffusion tensor for direction. Tumors and recurrent tumors are often associated with high cell-density, which slows the movement of interstitial water molecules and leads to reduced diffusivities, while radiation necrosis often presents enhanced water molecule diffusivity, due to cell necrosis and tissue loss. Several small cohort studies showed the potential of ADC measurement for differentiating between tumor and necrosis (36). However, the presence in both lesions of edema, which has a high ADC, complicates the use of diffusion measurement (37). Further work is still necessary to elucidate the sensitivity and specificity of diffusion MRI in characterizing radiation necrosis.

MR Spectroscopy

MR-based spectroscopic methods provide measurements on a biochemical level. Specific molecular changes that occur in radiation necrosis, including a decrease in N-acetylaspartate (NAA) and creatine (Cr) in tissue (38), and an increase in lipid content (at ~ 1.3 ppm), have been reported. In contrast, tumor tissues present high concentrations of choline (Cho). Herein, the ratios of Cho/Cr and Cho/NAA have been employed as biomarkers for the characterization of radiation necrosis and for the differentiation between from recurrent tumor (39). Nevertheless, these ratios depend on radiation dose, disease stage, and may also be complicated in the cases of mixed lesions. Currently, there is no consensus in the clinic regarding ratio calculations and the accuracy of MR spectroscopy in diagnosing and characterizing radiation necrosis following therapy.

1.3 Dissertation Overview

In this dissertation, Chapter 2 - 3 focus on improving tumor vascular property measurements by dynamic contrast-enhanced MRI. Clinical DCE-MRI data collected from patients with locally advanced-staged cervical cancer, pre- and post-radiotherapy, are analyzed.

Chapter 2 deals with the important question of which tracer kinetic model (i.e., the tissue response function) is optimal for the quantitative analysis of any given DCE-MRI data. A Bayesian probability theory-based model selection approach is applied to determine the most probable model from a pool of competing models.

Chapter 3 demonstrates the feasibility of using a voxel-specific, inferred constrained local-AIF (cL-AIF), based on fixed parameterization of the AIF measured from a large, feeding ("remote") artery with inclusion of two additional free parameters, bolus time-delay, Δt , and amplitude-scaling, s , to better model the DCE-MRI data on a voxel-by-voxel basis.

Following the discussion on quantifying vascular properties in Chapters 2 - 3, Chapters 4 - 5 focus on radiation treatment effects on normal brain tissue.

Chapter 4 evaluates the use of an anti-VEGF antibody in the treatment of developed, frank, radiation-induced necrosis in a mouse model. Both MRI and gold standard histology were used to assess the treatment response.

Chapter 5 assesses the effects of radiation-modulated normal brain parenchyma on the growth of naïve, non-irradiated, tumor cells in a novel mouse model simulating recurrent glioblastoma.

Finally, Chapter 6 closes out the dissertation by summarizing the specific accomplishments of these studies, and also proposes several interesting follow-up studies that are beyond the scope of the present work.

In Appendix A, an application of DCE-MRI in quantifying the temporary disruption of peritumoral blood brain barrier post-laser interstitial thermal therapy for patients with glioblastoma is presented. This work was performed in collaboration with Drs. Eric C Leuthardt, David D Tran, and Joshua S Shimony at Washington University School of Medicine.

Appendix B describes a project, on a different topic, designed to analyze the off-resonance effects on the longitudinal relaxation time measurements in grossly inhomogeneous fields (e.g., oil-well logging). This was an internship project supervised by Dr. Martin D. Hürlimann at Schlumberger-Doll Research, Cambridge, MA.

1.4 References

1. Bentzen SM. Preventing or reducing late side effects of radiation therapy: radiobiology meets molecular pathology. *Nat. Rev. Cancer* 2006;6:702–713. doi: 10.1038/nrc1950.

2. Garcia-Barros M, Paris F, Cordon-Cardo C, Lyden D, Rafii S, Haimovitz-Friedman A, Fuks Z, Kolesnick R. Tumor Response to Radiotherapy Regulated by Endothelial Cell Apoptosis. *Science* 2003;300:1155–1159. doi: 10.1126/science.1082504.
3. Jackson A, Buckley DL, Parker GJ, Ah-See MW. Dynamic contrast-enhanced magnetic resonance imaging in oncology. Springer; 2005.
4. Good JS, Harrington KJ. The Hallmarks of Cancer and the Radiation Oncologist: Updating the 5Rs of Radiobiology. *Clin. Oncol.* 2013;25:569–577. doi: 10.1016/j.clon.2013.06.009.
5. Barker HE, Paget JTE, Khan AA, Harrington KJ. The tumour microenvironment after radiotherapy: mechanisms of resistance and recurrence. *Nat. Rev. Cancer* 2015;15:409–425. doi: 10.1038/nrc3958.
6. Risau W. Mechanisms of angiogenesis. *Nature* 1997;386:671.
7. Rafii S. Circulating endothelial precursors: mystery, reality, and promise. *J. Clin. Invest.* 2000;105:17–19. doi: 10.1172/JCI8774.
8. Jain RK. Normalization of Tumor Vasculature: An Emerging Concept in Antiangiogenic Therapy. *Science* 2005;307:58–62. doi: 10.1126/science.1104819.
9. Jackson A, O'Connor JPB, Parker GJM, Jayson GC. Imaging Tumor Vascular Heterogeneity and Angiogenesis using Dynamic Contrast-Enhanced Magnetic Resonance Imaging. *Clin. Cancer Res.* 2007;13:3449–3459. doi: 10.1158/1078-0432.CCR-07-0238.
10. Cao M, Liang Y, Shen C, Miller KD, Stantz KM. Developing DCE-CT to quantify intra-tumor heterogeneity in breast tumors with differing angiogenic phenotype. *IEEE Trans. Med. Imaging* 2009;28:861–871.
11. De Langen AJ, Van Den Boogaart VE, Marcus JT, Lubberink M. Use of H215O-PET and DCE-MRI to measure tumor blood flow. *The oncologist* 2008;13:631–644.
12. Neeman M, Dafni H. Structural, functional, and molecular MR imaging of the microvasculature. *Annu. Rev. Biomed. Eng.* 2003;5:29–56.
13. Duan C, Perez-Torres CJ, Yuan L, Engelbach JA, Beeman SC, Tsien CI, Rich KM, Schmidt RE, Ackerman JJH, Garbow JR. Can anti-vascular endothelial growth factor antibody reverse radiation necrosis? A preclinical investigation. *J. Neurooncol.* 2017;1–8. doi: 10.1007/s11060-017-2410-3.
14. Perez-Torres CJ, Engelbach JA, Cates J, Thotala D, Yuan L, Schmidt RE, Rich KM, Drzymala RE, Ackerman JJH, Garbow JR. Toward Distinguishing Recurrent Tumor From Radiation Necrosis: DWI and MTC in a Gamma Knife-Irradiated Mouse Glioma Model. *Int. J. Radiat. Oncol.* 2014;90:446–453. doi: 10.1016/j.ijrobp.2014.06.015.
15. Kiselev V g. On the theoretical basis of perfusion measurements by dynamic susceptibility contrast MRI. *Magn. Reson. Med.* 2001;46:1113–1122. doi: 10.1002/mrm.1307.

16. Petersen ET, Zimine I, Ho Y-CL, Golay X. Non-invasive measurement of perfusion: a critical review of arterial spin labelling techniques. *Br. J. Radiol.* 2006;79:688–701. doi: 10.1259/bjr/67705974.
17. Allan JM, Travis LB. Mechanisms of therapy-related carcinogenesis. *Nat. Rev. Cancer* 2005;5:943–955. doi: 10.1038/nrc1749.
18. Hambardzumyan D, Gutmann DH, Kettenmann H. The role of microglia and macrophages in glioma maintenance and progression. *Nat. Neurosci.* 2016;19:20–27. doi: 10.1038/nn.4185.
19. Ohuchida K, Mizumoto K, Murakami M, Qian L-W, Sato N, Nagai E, Matsumoto K, Nakamura T, Tanaka M. Radiation to Stromal Fibroblasts Increases Invasiveness of Pancreatic Cancer Cells through Tumor-Stromal Interactions. *Cancer Res.* 2004;64:3215–3222. doi: 10.1158/0008-5472.CAN-03-2464.
20. Li H, Fan X, Houghton J. Tumor microenvironment: The role of the tumor stroma in cancer. *J. Cell. Biochem.* 2007;101:805–815. doi: 10.1002/jcb.21159.
21. Hellevik T, Pettersen I, Berg V, et al. Cancer-associated fibroblasts from human NSCLC survive ablative doses of radiation but their invasive capacity is reduced. *Radiat. Oncol.* 2012;7:59. doi: 10.1186/1748-717X-7-59.
22. Park CC, Zhang HJ, Yao ES, Park CJ, Bissell MJ. β 1 Integrin Inhibition Dramatically Enhances Radiotherapy Efficacy in Human Breast Cancer Xenografts. *Cancer Res.* 2008;68:4398–4405. doi: 10.1158/0008-5472.CAN-07-6390.
23. Cordes N, Seidler J, Durzok R, Geinitz H, Brakebusch C. β 1-integrin-mediated signaling essentially contributes to cell survival after radiation-induced genotoxic injury. *Oncogene* 2006;25:1378–1390.
24. Anon. Radiation Necrosis: Background, Pathophysiology, Epidemiology. 2017.
25. Fike JR, Cann CE, Turowski K, Higgins RJ, Chan ASL, Phillips TL, Davis RL. Radiation dose response of normal brain. *Int. J. Radiat. Oncol.* 1988;14:63–70. doi: 10.1016/0360-3016(88)90052-1.
26. Miyatake S-I, Nonoguchi N, Furuse M, Yoritsune E, Miyata T, Kawabata S, Kuroiwa T. Pathophysiology, Diagnosis, and Treatment of Radiation Necrosis in the Brain. *Neurol. Med. Chir. (Tokyo)* 2015;55:50–59. doi: 10.2176/nmc.ra.2014-0188.
27. Mou Y, Sai K, Wang Z, Zhang X, Lu Y, Wei D, Yang Q, Chen Z. Surgical management of radiation-induced temporal lobe necrosis in patients with nasopharyngeal carcinoma: report of 14 cases. *Head Neck* 2011;33:1493–1500. doi: 10.1002/hed.21639.
28. Rahmathulla G, Recinos PF, Valerio JE, Chao S, Barnett GH. Laser Interstitial Thermal Therapy for Focal Cerebral Radiation Necrosis: A Case Report and Literature Review. *Stereotact. Funct. Neurosurg.* 2012;90:192–200. doi: 10.1159/000338251.

29. Smith CJ, Myers CS, Chapple KM, Smith KA. Long-Term Follow-up of 25 Cases of Biopsy-Proven Radiation Necrosis or Post-Radiation Treatment Effect Treated With Magnetic Resonance-Guided Laser Interstitial Thermal Therapy: Neurosurgery 2016;79:S59–S72. doi: 10.1227/NEU.0000000000001438.
30. Shaw PJ, Bates D. Conservative treatment of delayed cerebral radiation necrosis. J. Neurol. Neurosurg. Psychiatry 1984;47:1338–1341.
31. Glantz MJ, Burger PC, Friedman AH, Radtke RA, Massey EW, Schold SC. Treatment of radiation-induced nervous system injury with heparin and warfarin. Neurology 1994;44:2020–2020.
32. Bui Q-C, Lieber M, Withers HR, Corson K, van Rijnsoever M, Elsaleh H. The efficacy of hyperbaric oxygen therapy in the treatment of radiation-induced late side effects. Int. J. Radiat. Oncol. 2004;60:871–878. doi: 10.1016/j.ijrobp.2004.04.019.
33. Gonzalez J, Kumar AJ, Conrad CA, Levin VA. Effect of bevacizumab on radiation necrosis of the brain. Int. J. Radiat. Oncol. Biol. Phys. 2007;67:323–326. doi: 10.1016/j.ijrobp.2006.10.010.
34. Torcuator R, Zuniga R, Mohan YS, et al. Initial experience with bevacizumab treatment for biopsy confirmed cerebral radiation necrosis. J. Neurooncol. 2009;94:63–68.
35. Bölke E, Nawatny J, Hoffmann TK, Peiper M, Orth K, Gerber PA, Rusnak E, others. Bevacizumab as a treatment option for radiation-induced cerebral necrosis. Strahlenther. Onkol. 2011;187:135–139.
36. Hein PA, Eskey CJ, Dunn JF, Hug EB. Diffusion-weighted imaging in the follow-up of treated high-grade gliomas: tumor recurrence versus radiation injury. Am. J. Neuroradiol. 2004;25:201–209.
37. Castillo M, Smith JK, Kwok L, Wilber K. Apparent diffusion coefficients in the evaluation of high-grade cerebral gliomas. Am. J. Neuroradiol. 2001;22:60–64.
38. Sundgren PC. MR Spectroscopy in Radiation Injury. Am. J. Neuroradiol. 2009;30:1469–1476. doi: 10.3174/ajnr.A1580.
39. Zeng Q-S, Li C-F, Zhang K, Liu H, Kang X-S, Zhen J-H. Multivoxel 3D proton MR spectroscopy in the distinction of recurrent glioma from radiation injury. J. Neurooncol. 2007;84:63–69. doi: 10.1007/s11060-007-9341-3.

Chapter 2 Tracer Kinetic Model Selection in Dynamic-Contrast Enhanced MRI¹

2.1 Introduction

Dynamic Contrast Enhanced (DCE) MRI is being used increasingly in the assessment of cancer, both pre- and post-therapy (1–9). Both semi-quantitative (1–4) and quantitative analyses (4–9) of time-resolved DCE-MRI data are used to derive information about tumor microcirculation and microvasculature. Semi-quantitative analyses, which derive measures directly from MR signal intensities, depend on MR hardware and the pulse sequences used to acquire the data, making it challenging to compare results between studies. In addition, the derived parameters, including signal-intensity plateau, contrast- enhancement ratio, and area under the curve, have no clear physiological meaning (4,10). By contrast, quantitative analysis employing tracer kinetic models yields physiological parameters related to tissue perfusion and capillary permeability.

Many tracer kinetic models have been applied to describe the behavior of administered contrast agent in DCE-MRI experiments. The first generation of DCE-MRI models, including the widely used Tofts model (TM) (11), were designed for tissues with negligible blood volume, and were used to characterize the permeability of the tissue vasculature. To account for intravascular signal contributions, the Extended Tofts Model (ETM) (12,13) was introduced for highly-perfused tissues, including tumors. Improvements in scanner hardware and software, which have led to higher-quality DCE-MRI data, have motivated the development of models with greater complexity (14,15) that more fully describe tissue perfusion and capillary permeability. Such models are

¹ All contents in this chapter have been published in Duan C, Kallehauge JF, Bretthorst GL, Tanderup K, Ackerman JJH, Garbow JR. Are Complex DCE-MRI Models Supported by Clinical Data? *Magn. Reson. Med.* 77:1329–1339 (2017)

physiologically more accurate (fewer assumptions/constraints regarding tissue structure) compared to reduced, simpler models that make physiological assumptions or introduce constraints that may not be appropriate for the tissue of interest and will, thus, generate bias in kinetic parameter estimates. However, in practice, it remains unknown whether these more complex models are supported by a given clinical DCE-MRI dataset with specific data quality (e.g., time resolution, acquisition time window, and contrast-to-noise ratio (CNR)). Thus, it is important to apply model selection, a data-driven process that balances the goodness of the fit and the stability of parameter estimation, to choose which kinetic model within a family of competing models best characterizes (is best supported by) the data.

The importance of selecting an appropriate DCE tracer kinetic model for measurement of tissue perfusion and capillary permeability has been examined in previous reports from other laboratories (16,17). Model selection algorithms, including Chi-square (18), Akaike information criterion (AIC) (18–20), F-test (21–23), and the Durbin-Watson statistic (18), have been applied to evaluate tracer kinetic models commonly used in DCE-MRI data analyses. However, very few of these studies have tested the stability of complex models as a function of data quality in the context of a pool of competing models. Luybaert et al. (25), and Murase et al. (26), investigated the effect of noise on the parameter estimation of individual DCE-MRI tracer kinetic models, but did not compare the accuracy and uncertainty of parameter estimation between models.

Bayesian probability theory (27) provides a rigorous statistical formalism for performing model-selection calculations. Advances in computational power and the development of Markov-chain Monte Carlo (MCMC) methods have greatly increased the applicability of Bayesian inference to a range of problems. Using a Bayesian approach, the model-selection problem is addressed by

treating the model itself as a parameter, for which the posterior probability, given the data and prior information, is computed.

The goal of this study was to test four compartmental tracer kinetic models against generically representative DCE-MRI data. Both *in silico* DCE-MRI data -- simulated based on each of the four models -- and clinical DCE-MRI cervical cancer data acquired pre-treatment and two-to-three weeks following the start of radiotherapy (RT) were utilized. Bayesian-based model selection and parameter estimation algorithms were applied to evaluate the noise tolerance to data analysis for each kinetic model and the dependence of the accuracy and uncertainty of parameter estimation on both model complexity and signal contrast-to-noise. Finally, applying model selection to clinical DCE-MRI cervical cancer data on a voxel-by-voxel basis, optimal models for the data were determined and then employed to estimate physiological parameters, including perfusion metrics and vascular permeability.

2.2 Methods

2.2.1 The DCE-MRI tracer kinetic models

Tracer kinetic modeling of vascular leakage and conservation of mass allow the tissue contrast-agent concentration (C_t) obtained following the administration of a contrast agent bolus to be written as:

$$C_t(t) = C_p(t) \otimes I(t), \quad (1)$$

where $C_p(t)$ is the concentration of the contrast agent in the plasma of the capillary inlet of any region-of-interest (ROI), commonly approximated by a measured upstream arterial input function (AIF), and $I(t)$ is the tissue impulse-response function to the contrast agent input, which depends

on the specific DCE-MRI tracer kinetic model. In this expression, “ \otimes ” denotes the convolution operation.

Springer and colleagues (28) have pointed out that, *in principle*, “tracer kinetic” models are inappropriate for DCE-MRI data because C_t is not directly measured. Rather, it is the tissue water ^1H relaxation enhancement caused by the agent that is monitored. Under some circumstances, the relaxation enhancement will be a non-linear function of C_t , requiring consideration of additional parameters not generally included in tracer kinetic models, e.g., the rate constant(s) governing water exchange across the relevant compartment boundaries. Such models are more complex than those considered herein. *In practice*, under conditions that approximate the MR-relaxation fast-exchange limit (29), the relaxation enhancement reasonably approximates a linear function of C_t , and tracer kinetic models are appropriate simplifications of a more complex system. Data described herein are consistent with this simplification.

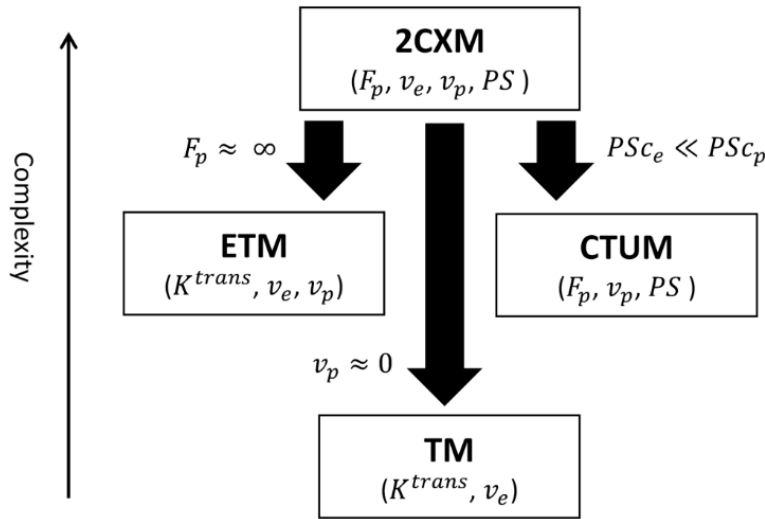


Figure 2.1: Hierarchy of the four compartmental tracer kinetic models and their corresponding model parameters. Under various physiological conditions, the general 2CXM, in which contrast agent is distributed into two separate compartments (vascular and extracellular-extravascular spaces), reduces to the simpler ETM, CTUM and TM. PS_{c_p} is the permeability-surface area

product of the vascular wall multiplied by the concentration of contrast agent in the blood plasma; and PSc_e is the permeability-surface area product of the vascular wall multiplied by the concentration of contrast agent in the extracellular-extravascular space.

Four compartmental DCE tracer kinetic models were included in this model selection study: (i) the four-parameter (F_p , v_e , v_p , and PS) Two-Compartment Exchange Model (2CXM), (ii) the three-parameter (F_p , v_p , and PS) Compartmental Tissue Uptake Model (CTUM); (iii) the three-parameter (K^{trans} , v_e , and v_p) Extended Tofts Model (ETM); and (iv) the two-parameter (K^{trans} and v_e) Tofts Model (TM). In these models, F_p is blood flow, v_e is the extracellular-extravascular volume fraction, v_p is the plasma volume fraction, PS is the permeability-surface area product, and K^{trans} is the forward volume transfer-rate constant. *Table 2.1* and *Figure 2.1* summarize the hierarchy and impulse response functions of these models. Further details about the relationships among these models are given in Sourbron et al. (16). In addition to the DCE tracer kinetic models, a “no signal” model, in which the data are assumed to consist only of noise, was also included, by default, in the model-selection calculation.

Table 2.1: Impulse response functions for the four tracer kinetic models.

	Impulse response function
2CXM ²	$I(t) = F_p * (A * \exp(-\alpha t) + (1 - A) * \exp(-\beta t))$
CTUM ³	$I(t) = F_p * ((1 - E) * \exp(-\gamma t) + E)$
ETM	$I(t) = K^{trans} * \exp(-K^{trans} * t) + v_p * \delta(t)$
TM	$I(t) = K^{trans} * \exp(-K^{trans}/v_e * t)$

² For the 2CXM, the impulse response function parameters A , α , and β are fully characterized by F_p , v_e , v_p , and PS .

³ For the CTUM, the impulse response function parameters E and γ are fully characterized by F_p , v_p and PS .

2.2.2 Clinical DCE-MRI data

De-identified clinical DCE-MRI cervical cancer data were acquired from patients enrolled in the EMBRACE study (<https://www.embracestudy.dk>), an international study of MRI-guided brachytherapy in locally advanced cervical cancer. All protocols were approved by the local medical ethics research board. Ten patients with advanced-stage cervical tumors (International Federation of Gynecology and Obstetrics: IIA/IIB/IIIB/IVA – 1/5/3/1) were scanned prior to, and two-to-three weeks after, the start of RT. This patient population was previously described in Kallehauge et al. (19).

Data were acquired on a 3-T Philips Achieva scanner *via* a 3D, saturation-recovery spoiled gradient-echo sequence (TR = 2.9 ms, TE = 1.4 ms, saturation time = 25 ms, flip angle = 10°, centric k-space sampling, matrix size = 176 X 176). A total of 120 dynamic scans (18 baseline scans, SNR \approx 5) for 20-to-24 5-mm-thick slices were obtained with 2.1 sec temporal resolution and 2.3 mm x 2.3 mm in-plane resolution.

Each DCE-MRI dataset consisted of two dynamic MRI sub-datasets: (i) the AIF dataset obtained from monitoring the external iliac artery and (ii) the tissue response dataset obtained from monitoring the cervix. An AIF for each patient (pre- and post-RT) was obtained by averaging multiple contrast agent concentration *vs.* time curves measured in the external iliac artery. All concentration *vs.* time curves were inspected manually to exclude curves that were affected by partial-volume effects.

Following the work of Fram et al. (30), a T_1 relaxation time-constant map was constructed using the variable flip angle method (flip angles = 5°, 10°, 15°, 20°, and 25°) *via* a 3D, spoiled gradient-echo sequence before contrast-agent administration, allowing conversion of DCE-MRI signal

intensity into contrast-agent concentration as described in Kallehauge et al. (31). Because a short echo time ($TE = 1.4$ ms) was used to collect the data, T_2^* dephasing was ignored for this conversion. To avoid the inflow artefacts in the iliac artery, a literature value of 1660 ms (32) for pre-contrast blood T_1 was used. Tumor tissue was identified and segmented on T_2 -weighted images by an experienced radiologist. Figure 2 shows four representative single tumor-voxel DCE datasets.

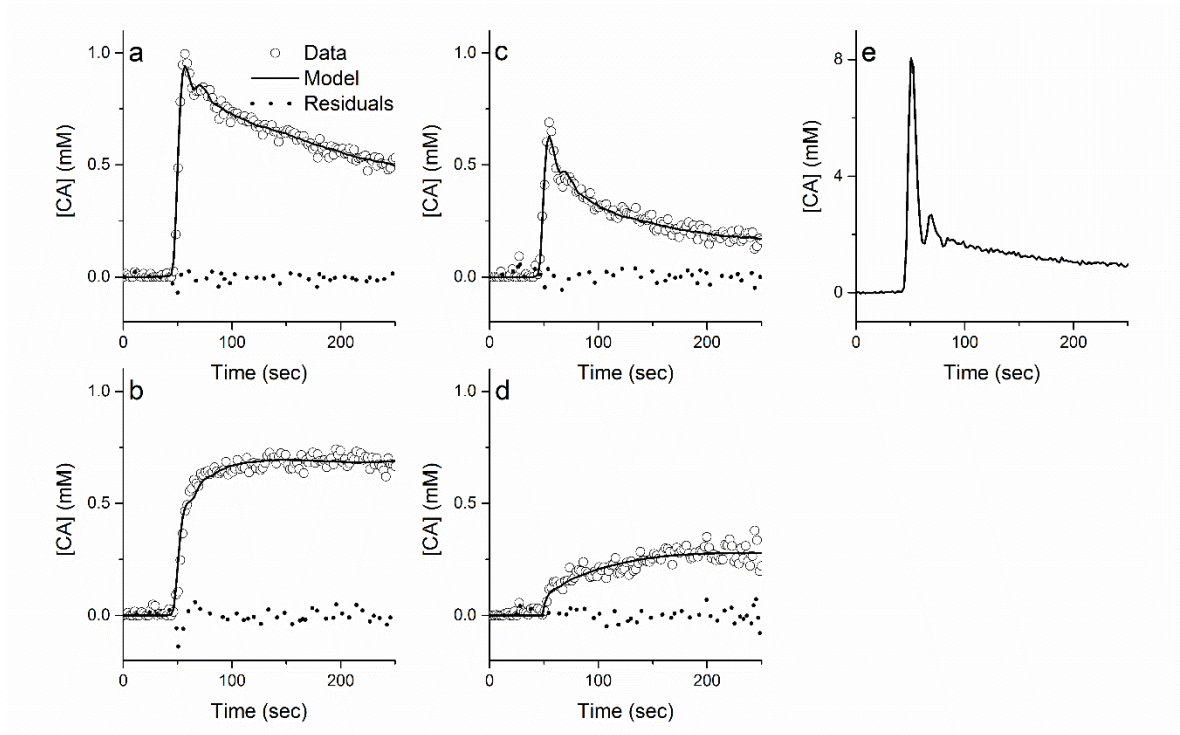


*Figure 2.2: Example DCE-MRI contrast agent concentration vs. time curves. The data is shown with circle, while the optimal model fitting is shown with solid line. For these example voxel-specific data sets, the optimal models were 2CXM (**Panel a**), CTUM (**Panel b**), ETM (**Panel c**), and TM (**Panel d**). Residuals are shown as dotted lines. All four kinetic models were selected as preferred models for some individual voxels within one cervical tumor. The measured AIF for this patient is shown in **Panel e** (note the change of the y-axis scale).*

2.2.3 *In silico* DCE-MRI data

In silico DCE-MRI data were generated based upon clinical pre-treatment DCE-MRI data from four cervical cancer patients. Both whole-tumor average (mean C_t across all voxels) and single-

voxel DCE time courses (one tumor voxel from each patient) were examined for these four patients (eight DCE time course datasets in total). The four whole-tumor average DCE datasets provided high contrast-to-noise at the expense of averaging DCE responses from a heterogeneous tissue (cancer). The four single-voxel DCE datasets provided a local DCE response at the expense of reduced contrast-to-noise. These two data-analysis strategies (region-of-interest and voxel-wise) are common to literature reports. Together with the measured upstream AIFs for each patient, these eight different DCE datasets -- a whole-tumor ROI and a single tumor-voxel from each of four patients -- were then each modeled by Bayesian-based algorithms (*vide infra*) using each of the four tracer kinetic models (eight DCE datasets x four DCE kinetic models).

For each of the eight DCE datasets, the estimated parameter values obtained for each of the four DCE kinetic models (2CXM, CTUM, ETM, TM; see Figure 2.3 for parameter ranges) were then used to generate four noiseless *in silico* DCE datasets, corresponding to each of the four kinetic models. Summarizing, based on analysis of the clinical data, eight, noiseless, differently parameter-valued, *in silico*, DCE datasets were generated for each of the four DCE kinetic models.

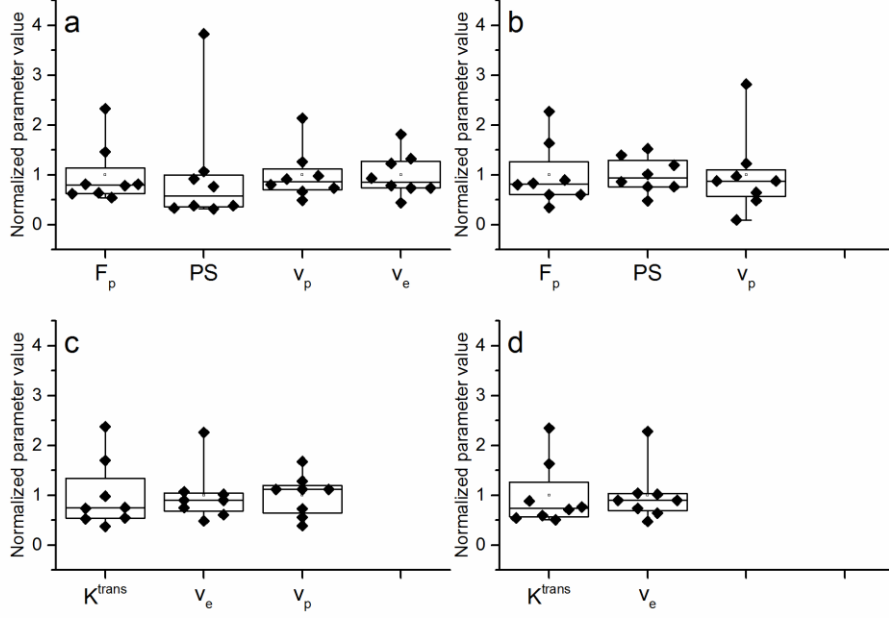


Figure 2.3: Range of kinetic parameter values (**Panel a:** 2CXM, **Panel b:** CTUM, **Panel c:** ETM and **Panel d:** TM) employed in the simulation studies. For the purpose of visual display, each kinetic parameter value is normalized by the mean of parameter values extracted from the eight sets of sample data. These mean values are: 1) 2CXM: $F_p = 0.74 \text{ min}^{-1}$; $PS = 0.16 \text{ min}^{-1}$, $v_p = 0.29$; $v_e = 0.20$; 2) CTUM: $F_p = 0.66 \text{ min}^{-1}$; $PS = 0.04 \text{ min}^{-1}$; $v_p = 0.31$; 3) ETM: $K^{trans} = 0.53 \text{ min}^{-1}$, $v_e = 0.41$; $v_p = 0.02$; 4) TM: $K^{trans} = 0.59 \text{ min}^{-1}$, $v_e = 0.42$.

For each of the simulated datasets, the temporal resolution, T_s (2.1 sec), and total acquisition time, T_{acq} (250 sec), were identical to those of the clinical DCE-MRI data-acquisition protocol. Normally distributed (Gaussian) noise (standard deviation from 0 to 0.2 mM in 0.005 mM steps) was then added to each of the simulated noise-free dataset. As such, the contrast-to-noise ratio (CNR), defined as the ratio of the *maximum* contrast-agent concentration to the noise standard deviation, ranges from infinity (no noise added) to approximately three. For each noise power, 100 different noise representations were simulated. Gaussian noise was used for two reasons. First, Gudbjartsson and Patz (33) have shown that MRI data noise distributions are nearly Gaussian for SNR larger than 2, which is very likely to be true for most DCE-MRI scans. Second, the distribution of baseline

signal, i.e., “baseline contrast agent concentration” (essentially pure noise), calculated for all of the cervical tumor voxels was well fit by a Gaussian model (see Figure 2.4).

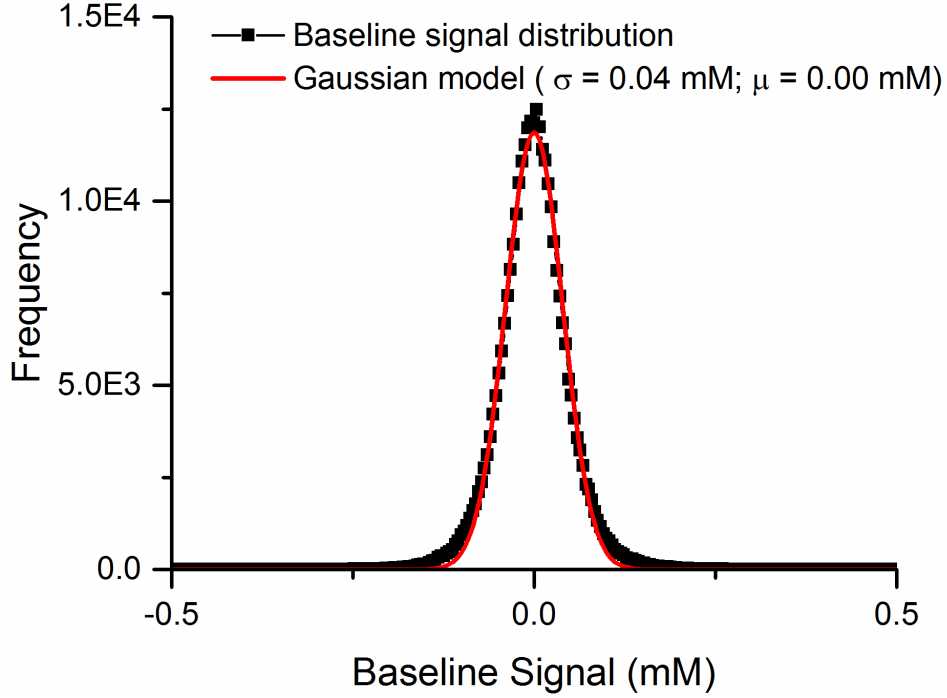


Figure 2.4: Distribution of baseline signals.

2.2.4 Bayesian-based model selection (and parameter estimation)

Bayesian probability theory was used to compute the posterior probabilities for all models on a voxel-by-voxel basis, using Bayes’ Theorem (27),

$$P(M|DI) = \frac{P(M|I)P(D|MI)}{P(D|I)} \quad (2)$$

where $P(M|DI)$ is the posterior probability for the M' th model, given the data, D , and all of the prior information, I . On the right-hand side of this equation, $P(M|I)$ is the prior probability for the M' th model and $P(D|MI)$ is the marginal direct probability for the data, given the model and the

prior information. Finally, $P(D|I)$ is the direct probability for the data, given the prior information, and serves as a normalization constant.

In Eq. (2), $P(D|MI)$ is a marginal direct probability because no kinetic model parameter appears in this probability. To compute this direct probability, the parameters appearing in the M' th model must be reintroduced into this equation. Taking the Tofts Model, with parameters K^{trans} and v_e as an example, equation (2) can be rewritten as,

$$P(M|DI) \propto P(M|I) \int dK^{trans} dv_e P(K^{trans}v_e|MI)P(D|K^{trans}v_eMI) \quad (3)$$

where the normalization constant has been dropped. $P(K^{trans}v_e|MI)$ is the joint prior probability for K^{trans} and v_e , given the model M (in this case, the TM) and the prior information; and $P(D|K^{trans}v_eMI)$ is the direct probability for the data (the likelihood function), given K^{trans} , v_e , the model M , and the prior information. A key feature of Bayesian-based model selection is that it integrates over the joint posterior probability for all of the parameters, thereby taking into account all of the possible parameter-value combinations. The importance/weight (“penalty”) assigned to each parameter derives naturally from that parameter’s contribution to the likelihood function of the modeled data (i.e., its posterior probability), which distinguishes the Bayesian approach from other constrained optimization methods.

The posterior probability for the model indicator, given the data and the prior information, $P(M|DI)$, was approximated using a MCMC calculation with simulated annealing (i.e., the MCMC calculation and simulated annealing were used to approximate the complex, analytically intractable, multidimensional integral in Eq. [3]). Initial values for all of the parameters, including the model indicator, were sampled from the prior probabilities for each parameter and the model indicator. Uniformly distributed prior probabilities, bounded by

appropriate physiologic ranges, were assigned to all of the parameters (see Table 2.2) and to the model indicators (i.e., all four models were assumed to be equally likely). In simulated annealing, an annealing parameter, β , which varies from 0 to 1, is introduced by raising the direct probability of the data to the β power. When $\beta = 0$, the direct probability of the data is zero and the priors are sampled independent of the data. The data are then slowly brought into the simulation as β increases and, when $\beta = 1$, the full joint posterior probability for the parameters and model indicators is sampled. In this MCMC calculation, the model is varied by proposing a new model indicator and then simulating (i.e., drawing samples for) the new model parameters. After this new proposed model has reached equilibrium, i.e., the distributions of the drawn model parameter values in MCMC are stationary, the proposed model is either accepted or rejected using the Metropolis-Hastings acceptance criteria (34). If the proposed model is accepted, the annealing step is complete. However, if the proposed model is rejected, the calculation returns to the original model and new values for the model parameters are proposed. At the completion of the calculation, the posterior probabilities for all the models and their parameters are approximated by the distributions of the Markov chain samples.

All model-selection calculations for in silico and clinical DCE-MRI data were performed using a Bayes Data-Analysis Toolbox (<http://bayesiananalysis.wustl.edu>) developed by G. Larry Bretthorst. All DCE-MRI contrast agent concentration signal models were written in Fortran and then loaded into the Image Model Selection package within this Toolbox. Computations were carried out on Dell PowerEdge R900 servers (Dell, Inc., Round Rock, TX), vintage 2008. All MCMC calculations were performed with 48 simulations and 50 repetitions; a total of 2400 simulations were run for each dataset (one voxel). For each simulation, a minimum of 50 annealing

steps was employed. Using a server with 24 CPUs, the average computation time for one patient was about 12 hours.

Table 2.2: Prior ranges⁴ for all the parameters within the response functions

TM		ETM		CTUM		2CXM	
K^{trans} (min ⁻¹)	0 - 60	K^{trans} (min ⁻¹)	0 - 60	E_p (min ⁻¹)	0 - 60	E_p (min ⁻¹)	0 - 60
v_e	0 - 1	v_e	0 - 1	E	0 - 1	A^5	0.5 - 1
		v_p	0 - 1	γ (min ⁻¹)	0 - 6	α (min ⁻¹)	0 - 6
						β (min ⁻¹)	0 - 6

2.2.5 Statistical analysis

All traditional (frequentist) statistical analyses were performed in Matlab (The Mathworks, Inc., Natick, MA). For changes in gross tumor volume, model selection, and parameter estimation on the clinical DCE-MRI data, a paired, two-sided Wilcoxon signed rank test was used to compare the pre- and post-RT time points in a matched fashion. Statistical significance was set at $P = 0.05$.

2.3 Results

In silico data were generated based on the clinical cervical cancer DCE-MRI data from four different patients. Figure 2.5 summarizes the model selection and parameter estimation results for in silico data simulated based on the whole-tumor average DCE-MRI data of patient #1. In Figure 2.5a, model selection was employed to analyze in silico data simulated based on each of the four

⁴ All the priors are uniformly distributed within the given range.

⁵ A is forced to be larger than 0.5 to separate the two exponential components in the response function of the 2CXM.

DCE models. At each noise power, 100 independent simulations (i.e., different noise sets) were performed and the number of “correct” selections, in which model selection chose the model used to simulate the data, were recorded. The number of correct model selections varied as a function of both model complexity and noise power (i.e., CNR). When the added noise standard deviation (SD) < 0.015 mM (i.e., $\text{CNR} > 36$), which is small compared to our clinical data (baseline noise SD = 0.04 mM, as shown in Figure 2.4), Bayesian model selection always chose the correct model, independent of the complexity of the model. However, as the CNR decreased, simpler data representations were preferred relative to more complex models. For data created based on the 2CXM, the number of correct selections dropped when the noise SD > 0.015 mM. For data created based on the ETM, the number of correct selections dropped when the noise SD > 0.055 mM (i.e., $\text{CNR} < 10$); for data based on the CTUM, the threshold was a noise SD > 0.10 mM (i.e., $\text{CNR} < 5$). By contrast, for the TM, the simplest model, model selection chose the correct model even when the noise SD increased to 0.2 mM (i.e., $\text{CNR} = 3$). For CNR much lower than 3, model selection chose the “no signal” model (data not shown). Figure 3b shows the model selection results for in silico data created based on the 2CXM. The number of correct model selections dropped rapidly as noise SD > 0.015 mM, with a concomitant increase in the selection of the CTUM, a simplified version of the 2CXM. However, with decreasing CNR ($\text{CNR} < 7$, Noise SD > 0.08 mM), Bayesian model selection most often chose the TM, the simplest model. Figure 2.5c-d show how the accuracy and uncertainty of estimations of v_e , the only common parameter between the simplest model, the TM (Figure 2.5c), and the most complex model, the 2CXM (Figure 2.5d), varied as Gaussian noise was added to each noiseless in silico dataset. While the accuracy of the v_e estimation for each model remained stable as CNR decreased, the uncertainties

(i.e., error bars) of the estimated v_e were much smaller for the TM relative to the more complex 2CXM.

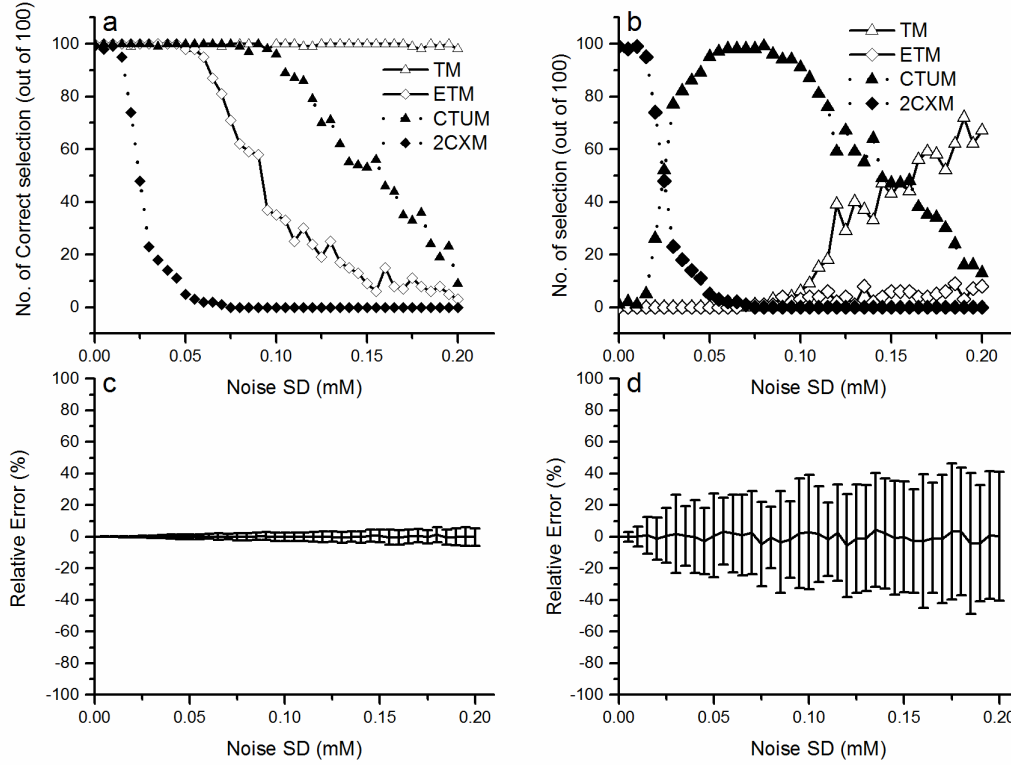


Figure 2.5: Bayesian DCE-MRI model-selection and parameter-estimation. Panel a: for each of the four *in silico* DCE-MRI data models, the number of “correct” model-selections (out of 100 different noise representations), as a function of the noise standard deviation (SD). **Panel b:** for the two-compartment exchange *in silico* DCE-MRI data model (the most complex model of the four models examined), the number of times a given model was selected (out of 100 different noise representations) as a function of the noise SD. **Panels c & d:** relative percent error of v_e estimated from initially noiseless simulated TM (**Panel c**) and 2CXM (**Panel d**) as a function of added noise.

Similar to Figure 2.5a&b, Figure 2.6 and Figure 2.7 illustrate graphically the model selection results for the 32 *in silico* datasets (eight differently parameter-valued datasets x four DCE kinetic models). The general qualitative trends are the same as shown in Figure 2.5a&b (Qualitatively similar results are also obtained for kinetic parameter values extracted from the perfusion literature, and for a different set of DCE models). As CNR decreased, the number of correct model selections varied as a function of both CNR and model complexity. Consistently, correct selection

of complex models required higher CNR (lower noise power) than simpler models. CTUM and ETM, despite having the same number of model parameters, behaved consistently differently. As CNR decreased, the complex 2CXM was replaced by the simpler CTUM, and, eventually, by the simplest TM. However, for each model, the specific noise power at which the number of correct selections started to decrease depended on the kinetic model's parameter values, which were derived from the original clinical DCE data used to simulate the *in silico* data. Note that the kinetic model's parameter values affect the MRI contrast agent entering the tissue, which also influence the CNR of the acquired DCE-MRI data.

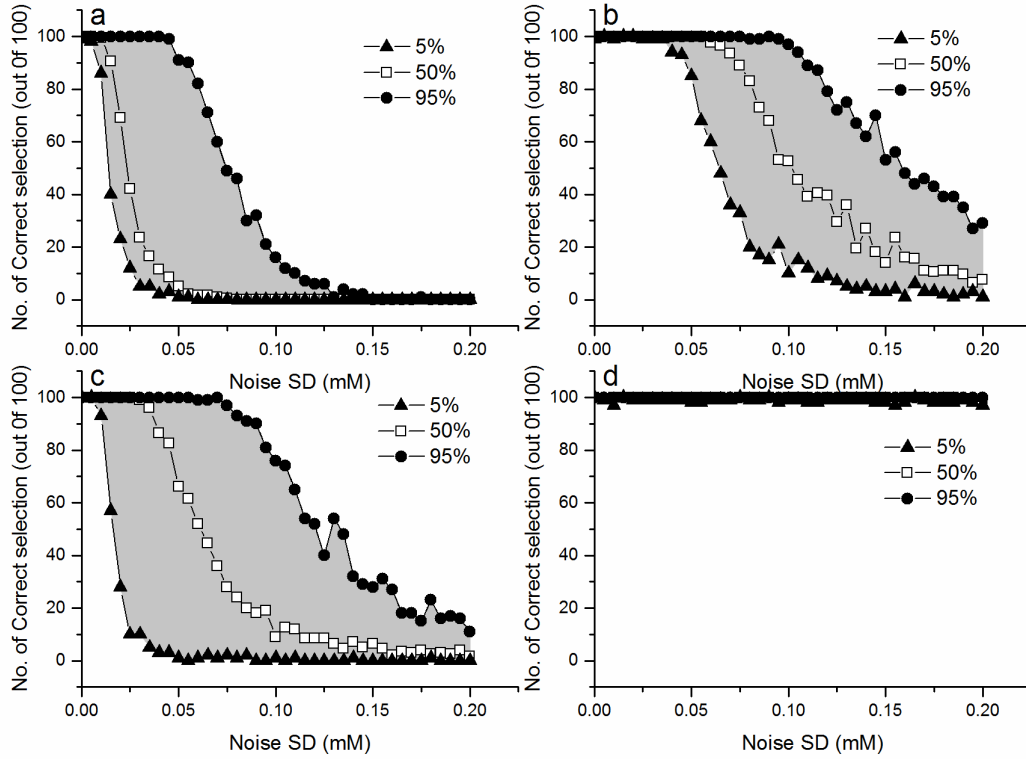


Figure 2.6: Pooled model selection results for *in silico* datasets created for each of the four DCE models. Panel a: 2CXM; Panel b: CTUM; Panel c: ETM; and Panel d: TM. For each model, the 5th, 50th, and 95th percentiles of numbers of correct selections are plotted.

Bayesian model selection was then applied to the full set of clinical DCE-MRI cervical cancer data acquired from ten patients. Figure 2.2 illustrates example contrast-agent concentration *vs.* time curves from four individual voxels within a single cervical tumor (Patient #1), in which the 2CXM (Figure 2.2a), CTUM (Figure 2.2b), ETM (Figure 2.2c), or TM (Figure 2.2d), respectively, are the Bayesian-preferred tracer kinetic models. While each of the four models was preferred in some individual voxels, Figure 2.8a shows that the TM and CTUM were overwhelmingly selected as best representing cervical cancer DCE-MRI data acquired both pre-treatment and two-to-three weeks following the start of RT. After two-to-three weeks of therapy, the percentage of voxels best fit by the TM dropped by 19% ($P = 0.16$), while the percentage of voxels best fit by the CTUM increased by 14% ($P = 0.19$). Based upon a paired, two-sided Wilcoxon signed rank test, neither of these changes is statistically significant. Defining CNR as the ratio of the *maximum* contrast-agent concentration to the baseline noise standard deviation (calculated prior to the arrival of the main contrast-agent bolus), Figure 2.8b-c illustrate the CNR distributions of voxels across ten subjects (pre-treatment in Figure 2.8b, and two-to-three weeks following the start of RT in Figure 2.8c), in which either the TM or CTUM were the optimal models. For cervical cancer data collected both pre-treatment and two-to-three weeks following the start of RT, the median CNRs for data best modeled by the CTUM were larger than for data best modeled by the TM (18.9 *vs.* 14.3, and 21.4 *vs.* 15.0, respectively).

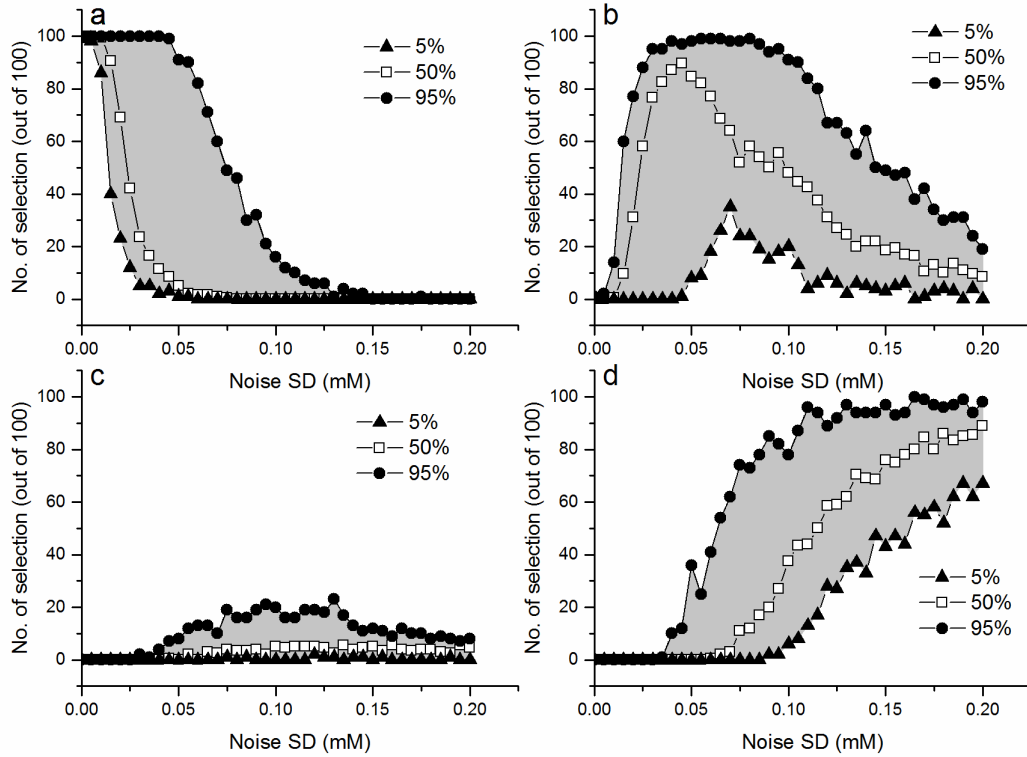


Figure 2.7: Pooled model selection results for *in silico* datasets created for the 2CXM only. The numbers of selections for each model are shown in **Panel a**: 2CXM; **Panel b**: CTUM; **Panel c**: ETM; and **Panel d**: TM, respectively. Similar to Figure 4, the 5th, 50th, and 95th percentiles of the numbers of selection for each model are plotted.

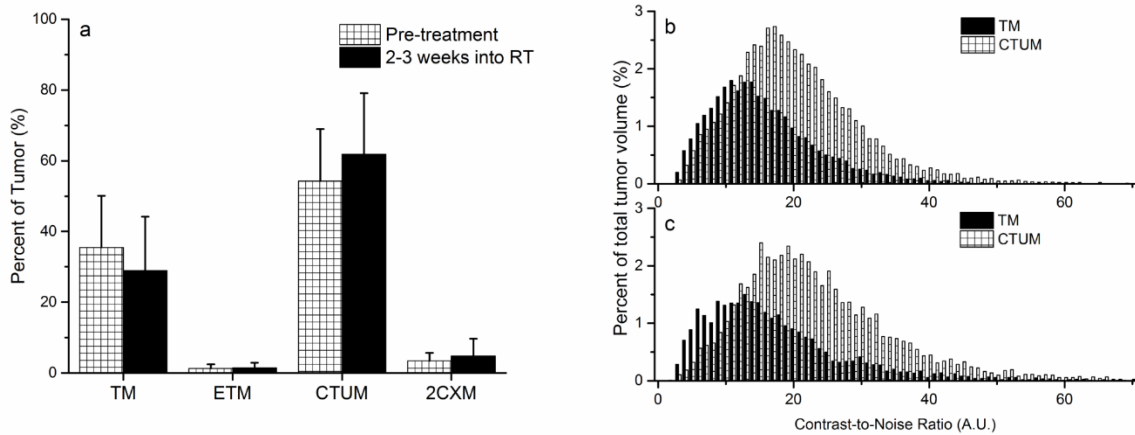


Figure 2.8: Bayesian DCE-MRI model selection results for a cohort of cervical cancer patients. **Panel a**: The average percent distribution of the optimal DCE-MRI model from the cohort of ten patients (39,365 total tumor voxels). The uncertainty bars indicate the standard deviation of the model distribution across all ten subjects. **Panel b & c**: Pooled CNR distribution of pre-treatment

(Panel b) and two-to-three weeks following the start of RT (Panel c) tumor voxels that are best represented by TM (solid black) or CTUM (crosshatch) DCE-MRI models.

Next, the two dominant models, TM and CTUM, were used to estimate pharmacokinetic parameters for cervical tumor voxels in which each was preferred. Three pharmacokinetic parameters (K^{trans} from the TM, and F_p and PS from the CTUM) relating to tissue perfusion and capillary permeability increased two-to-three weeks into RT. Figure 2.9 shows that K^{trans} increased (mean \pm SD) from $0.60 \pm 0.48 \text{ min}^{-1}$ to $1.56 \pm 1.08 \text{ min}^{-1}$ ($P = 0.004$), F_p increased from $0.69 \pm 0.37 \text{ min}^{-1}$ to $1.46 \pm 0.95 \text{ min}^{-1}$ ($P = 0.002$), and PS increased from $0.058 \pm 0.024 \text{ min}^{-1}$ to $0.078 \pm 0.024 \text{ min}^{-1}$ ($P = 0.014$). Representative parametric maps and corresponding uncertainty maps were shown in Figure 2.10.

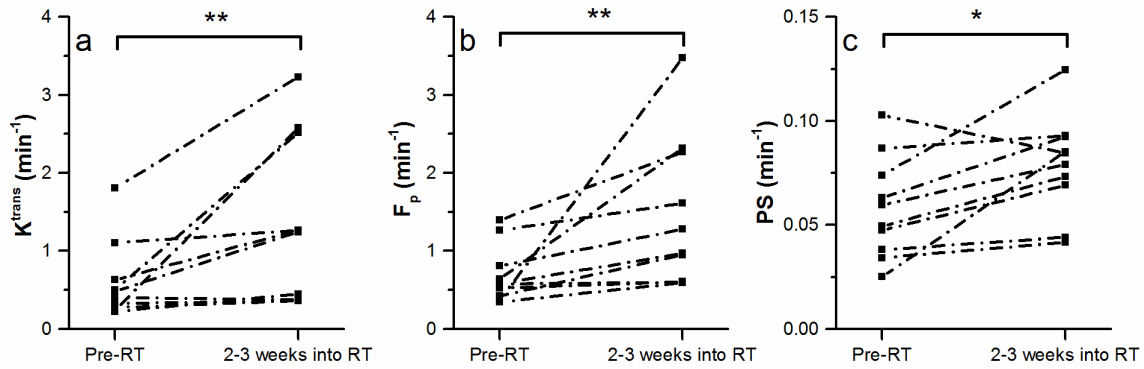


Figure 2.9: Pharmacokinetic parameters estimated using the optimal DCE-MRI kinetic models for all subjects. **Panels a-c:** Paired scatter plots of median pharmacokinetic parameter estimates, both pre-treatment and two-to-three weeks following the start of RT, for tumor voxels in which the TM is the optimal model (K^{trans} in **Panel a**) and those in which the CTUM is the optimal model (F_p in **Panel b** and PS in **Panel c**). Here, * indicates $P < 0.05$, and ** indicates $P < 0.01$, as calculated by a paired, two-sided Wilcoxon signed rank test.

2.4 Discussion

The central goal of this study was to test the performance of complex DCE-MRI models in the context of a pool of competing models against: (i) in silico DCE-MRI data simulated based on

each of the four models and (ii) clinical DCE-MRI data acquired prior to and two-to-three weeks following the initiation of RT in a cohort ($n = 10$) of advanced-stage, cervical cancer patients. For the clinical data, parameters were estimated, on a voxel-by-voxel basis, employing the selected, optimal kinetic model for each voxel.

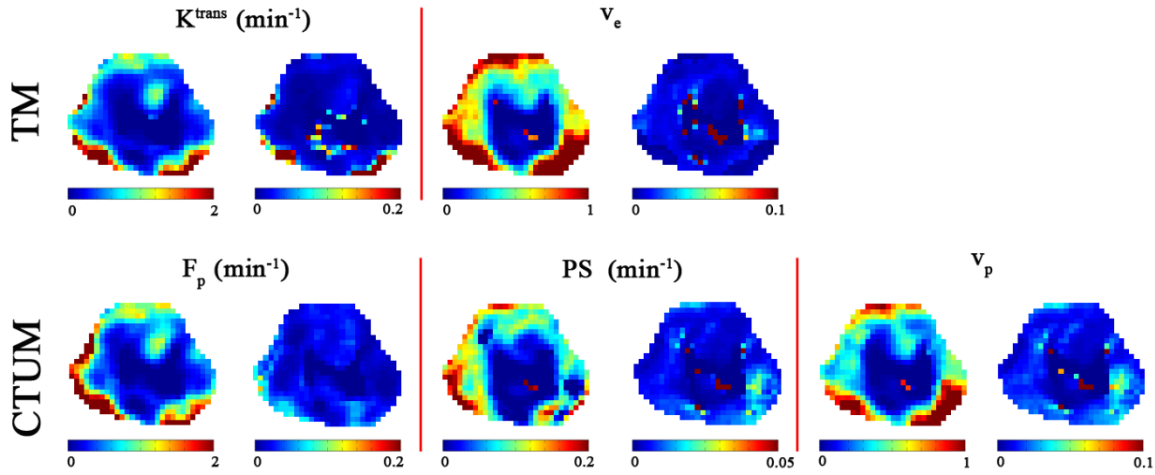


Figure 2.10: Parametric estimates (left map of each pair) and corresponding uncertainties (right map of each pair).

The determination of an appropriate kinetic model is essential for extracting quantitative tissue perfusion and vascular permeability parameters from DCE-MRI data. Complex models (i.e., those with more parameters) will always provide better fits in terms of residuals alone (e.g., Chi-square). However, the inclusion of additional parameters may not be well supported by the acquired DCE-MRI data, and may, consequently, increase the uncertainty (variance) in the estimation of the parameters within the model.

Our simulation study shows that complex DCE-MRI models are more sensitive to CNR than simpler models with respect to both model selection (Figure 2.5a-b, Figure 2.6&Figure 2.7) and parameter estimation (Figure 2.5c-d). As noise standard deviation increases (i.e., CNR decreases),

Bayesian model selection chooses simpler data representations (Figure 2.5b and Figure 2.7), a statistically rigorous manifestation of Occam's razor. Similarly, as CNR decreases, uncertainties in parameter estimates for highly parameterized models increase much more rapidly than for simpler models and Bayesian model selection chooses simpler models. For two models having the same complexity (i.e., the same number of model parameter), the CTUM is more robust than the ETM for the data examined herein.

Although each of the four models is preferred in some individual tumor voxels, the TM and CTUM are the two dominant models for the acquired cervical cancer DCE-MRI data. The 2CXM and ETM were seldom selected, a finding that agrees well with our *in silico* results. As shown in Figure 2.5b and Figure 2.7, as CNR decreases, the general 2CXM reduces to the CTUM and eventually to the TM. Amongst the two preferred kinetic models, selection of the three-parameter CTUM generally requires higher CNR than the two-parameter TM. However, choice of the optimal (most probable) model also depends on other factors beyond CNR, including kinetic/compartmental constraints imposed by physiological conditions, which explains the overlap of CNR distributions between the TM and CTUM in Figure 2.8b-c. For example, when the total acquisition time course is short or the extracellular extravascular space (EES) is large, the forward contrast-agent flux from plasma to EES is much larger than the contrast-agent backflux from EES to plasma. Under such conditions, the CTUM, which ignores the backflux, is the physiologically more appropriate model (16) and, thus, better represents the acquired dynamic curves.

In heterogeneous tissue such as cancer, DCE model selection poses the “mixed tissue conundrum”. This is illustrated in the current case where different tumors, the same tumors at different times (e.g., before and after treatment), different tumor regions, and different tumor voxels support different DCE models, making it difficult to compare modeling results (e.g., intermodal

comparison of estimated model-specific parameter values). However, in highly heterogeneous tissues such as cancer, this is not an unexpected result. Different tumors, different tumor regions, and different tumor voxels possess different physiologic and microstructural characteristics. Indeed, to a large extent, it is the competing models themselves that provide the desired tissue discrimination/characterization. In this light, transformation from one model to another in the face of therapy or other physiologic challenge may provide an important metric for patient care.

Choosing one commonly used “simpler” pharmacokinetic tracer model (without model selection justification) for data analysis would not avoid but hide the underlying mixed tissue conundrum by losing information and biasing parameter estimates. Whether DCE voxel-wise data of sufficient quality could be obtained such that a “more complex” model would be the most probable for all (or the substantial majority of) voxels in a truly heterogeneous tissue such as cancer is an interesting but open question. However, data from voxels that are well-fit by a simple model are likely to be inadequate to support a more complex model vis-à-vis Occam’s razor.

In addition to CNR investigated in this study, both temporal resolution and acquisition time window will also affect the ability of the kinetic models to fit the data, which will consequently affect model selection results. An extensive examination of how each of these factors affects model selection results is beyond the scope of this study. Therefore, it is impossible to draw universal conclusions regarding whether a given DCE model can be supported or not at a specific noise power (or temporal resolution or acquisition time). For each individual DCE-MRI dataset, data-driven model selection must be performed for the identification of voxel-specific optimal (most probable) models.

Biophysical properties not investigated in this study, but which may also affect the signal response in clinical DCE-MRI studies, include T_2^* dephasing, water exchange, inter-voxel convection (contrast agent flux from highly leaky voxel to less leaky voxels), and AIF accuracy (bolus dispersion and partial volume effects). All of these effects may influence the acquired DCE signal and, thus, affect the tracer kinetic modeling and model selection. Models that fully account for these effects, which were not included in this study, must incorporate more free parameters and thus have higher model complexity. Even though such models are physiologically more correct and more general in terms of applicability, it is likely that data quality would have to be exceptionally high to justify their use *vs.* less complex models. In this context, for any given DCE-MRI dataset, data-driven model selection is a necessary prerequisite.

It is worth stressing here that there is no substitute for a well-considered data acquisition protocol, i.e., high quality data. Without such a protocol, even the most sophisticated post-acquisition analysis is left with effects that cannot be estimated in a reasonably small set of model parameters, but which will influence parameter estimates. Importantly, DCE signal effects related to T_2^* dephasing, water exchange, and AIF bolus dispersion and partial voluming can be minimized by optimizing the data acquisition protocol. For instance, T_2^* dephasing can be computed *via* a dual-echo sequence (35), and the water exchange effect can be suppressed by a careful selection of flip angle (36). In addition, the AIF accuracy can be improved by the selection of a reference region (37).

We note here that the estimated values for parameter shared amongst these DCE models are different from model to model, and that some of the computed values in some models are apparently non-physical (e.g., large 2CXM and CTUM v_p). The model selection and parameter

estimation algorithms described herein are not the source of such biases. Our in silico simulation study, in which parameter values were estimated accurately, but with decreasing precision, as contrast-to-noise decreased, provides *prima facie* evidence that parametric biases in our study are not due to the modeling algorithms. Rather, the models are unavoidably wrong (i.e., are simplifications of a very complex tissue physiology), the data collection is unavoidably constrained/compromised by scanner capabilities, and the clinically achievable contrast-to-noise is unavoidably modest. Thus, while the estimation procedure is unbiased, the models and the data are biased. Therefore, that some parameter estimates seem physiologically implausible is not surprising and is not limited to this study but occurs throughout the literature. For example, while the ETM (also known as the Extended Patlak Model) usually produce v_p less than 0.1, studies (19,21,38–41) employing the newer 2CXM produce substantially higher v_p (up to 0.44). Whether the parameters so obtained are of clinical value in cancer detection and management is beyond the scope of this investigation. Nevertheless, the continued presence of such studies in the peer-reviewed literature suggests that the DCE-MR community feels such studies do have value, a manifestation of Box’s dictum (42).

The use of quantitative pharmacokinetic parameters to evaluate the therapeutic response of tumors has been demonstrated in several studies (43–46). Our data showed that F_p , PS , and K^{trans} , which is a mixture of F_p and PS (16), increased during the early stages (two-to-three weeks) of RT (Figure 7). These changes are consistent with DCE-MRI results from previous studies (44,45) on pre- and post-radiotherapy cervical cancer. We caution that changes observed herein are only for voxels defined as tumor based on T2-weighted images. Further, it has been shown that possible underlying biological processes that are secondary to the radiotherapy (47), such as inflammation, may confound quantitative DCE-MRI measures of tumor perfusion and permeability, especially

at early stages of treatment. Monitoring long-term patient outcomes, including both MR and clinical tumor indices, is necessary before making inferences regarding therapeutic response.

In conclusion, we have applied Bayesian-based algorithms to DCE-MRI tracer kinetic model selection and parameter estimation. Both DCE-MRI model selection and parameter estimation are sensitive to model complexity and data quality. Highly parameterized, complex models require higher data quality for accurate and stable model parameter estimation. In the absence of performing a model-selection calculation, these complex models should be employed cautiously. The two-parameter TM and the three-parameter CTUM were found to be the two dominant models for the clinical DCE-MRI cervical cancer data examined herein. Beyond other physiological factors, the three-parameter CTUM required higher CNR than the two-parameter TM. Significant changes in tumor perfusion and permeability (K^{trans} , F_p , and PS) were found during the early stages of RT. Correlating pre-treatment pharmacokinetic parameters with long-term treatment outcomes, such as local control and disease-specific survival, will be the subject of future work.

2.5 Acknowledgements

This project was supported by funding from the Alvin J. Siteman Comprehensive Cancer Center (P30 CA091842), research grants from CIRRO – the Lundbeck Foundation Centre for Interventional Research in Radiation Oncology, and funding from the Danish Research Council. We gratefully acknowledge the anonymous reviewers for their helpful comments.

2.6 References

1. Mayr NA, Yuh WTC, Jajoura D, Wang JZ, Lo SS, Montebello JF, Porter K, Zhang D, McMeekin DS, Buatti JM. Ultra-early predictive assay for treatment failure using functional magnetic resonance imaging and clinical prognostic parameters in cervical cancer. *Cancer* 2010;116:903–912. doi: 10.1002/cncr.24822.

2. Woolf DK, Padhani AR, Taylor NJ, Gogbashian A, Li SP, Beresford MJ, Ah-See M-L, Stirling J, Collins DJ, Makris A. Assessing response in breast cancer with dynamic contrast-enhanced magnetic resonance imaging: are signal intensity-time curves adequate? *Breast Cancer Res. Treat.* 2014;147:335–343. doi: 10.1007/s10549-014-3072-x.
3. Røe K, Mikalsen LT, van der Kogel AJ, Bussink J, Lyng H, Ree AH, Marignol L, Olsen DR. Vascular responses to radiotherapy and androgen-deprivation therapy in experimental prostate cancer. *Radiat. Oncol. Lond. Engl.* 2012;7:75. doi: 10.1186/1748-717X-7-75.
4. Zahra MA, Tan LT, Priest AN, Graves MJ, Arends M, Crawford RAF, Brenton JD, Lomas DJ, Sala E. Semiquantitative and Quantitative Dynamic Contrast-Enhanced Magnetic Resonance Imaging Measurements Predict Radiation Response in Cervix Cancer. *Int. J. Radiat. Oncol.* 2009;74:766–773. doi: 10.1016/j.ijrobp.2008.08.023.
5. Loncaster JA, Carrington BM, Sykes JR, et al. Prediction of radiotherapy outcome using dynamic contrast enhanced MRI of carcinoma of the cervix. *Int. J. Radiat. Oncol.* 2002;54:759–767. doi: 10.1016/S0360-3016(02)02972-3.
6. Hawighorst H, Knapstein PG, Knopp MV, Weikel W, Brix G, Zuna I, Schönberg SO, Essig M, Vaupel P, Kaick G van. Uterine Cervical Carcinoma: Comparison of Standard and Pharmacokinetic Analysis of Time-Intensity Curves for Assessment of Tumor Angiogenesis and Patient Survival. *Cancer Res.* 1998;58:3598–3602.
7. Lazanyi KS, Abramyuk A, Wolf G, Tokalov S, Zöphel K, Appold S, Herrmann T, Baumann M, Abolmaali N. Usefulness of dynamic contrast enhanced computed tomography in patients with non-small-cell lung cancer scheduled for radiation therapy. *Lung Cancer Amst. Neth.* 2010;70:280–285. doi: 10.1016/j.lungcan.2010.03.004.
8. Craciunescu OI, Yoo DS, Cleland E, Muradyan N, Carroll MD, MacFall JR, Barboriak DP, Brizel DM. Dynamic contrast-enhanced MRI in head-and-neck cancer: the impact of region of interest selection on the intra- and interpatient variability of pharmacokinetic parameters. *Int. J. Radiat. Oncol. Biol. Phys.* 2012;82:e345–350. doi: 10.1016/j.ijrobp.2011.05.059.
9. Barrett T, Gill AB, Kataoka MY, et al. DCE and DW MRI in monitoring response to androgen deprivation therapy in patients with prostate cancer: a feasibility study. *Magn. Reson. Med. Off. J. Soc. Magn. Reson. Med. Soc. Magn. Reson. Med.* 2012;67:778–785. doi: 10.1002/mrm.23062.
10. Walker-Samuel S, Leach MO, Collins DJ. Evaluation of response to treatment using DCE-MRI: the relationship between initial area under the gadolinium curve (IAUGC) and quantitative pharmacokinetic analysis. *Phys. Med. Biol.* 2006;51:3593–3602. doi: 10.1088/0031-9155/51/14/021.
11. Tofts PS, Brix G, Buckley DL, et al. Estimating kinetic parameters from dynamic contrast-enhanced T(1)-weighted MRI of a diffusable tracer: standardized quantities and symbols. *J. Magn. Reson. Imaging JMRI* 1999;10:223–232.
12. Tofts PS. Modeling tracer kinetics in dynamic Gd-DTPA MR imaging. *J. Magn. Reson. Imaging JMRI* 1997;7:91–101.

13. Sourbron SP, Buckley DL. On the scope and interpretation of the Tofts models for DCE-MRI. *Magn. Reson. Med. Off. J. Soc. Magn. Reson. Med. Soc. Magn. Reson. Med.* 2011;66:735–745. doi: 10.1002/mrm.22861.
14. Brix G, Kiessling F, Lucht R, Darai S, Wasser K, Delorme S, Griebel J. Microcirculation and microvasculature in breast tumors: Pharmacokinetic analysis of dynamic MR image series. *Magn. Reson. Med.* 2004;52:420–429. doi: 10.1002/mrm.20161.
15. de Bazelaire C, Siauve N, Fournier L, Frouin F, Robert P, Clement O, de Kerviler E, Cuenod CA. Comprehensive model for simultaneous MRI determination of perfusion and permeability using a blood-pool agent in rats rhabdomyosarcoma. *Eur. Radiol.* 2005;15:2497–2505. doi: 10.1007/s00330-005-2873-z.
16. Sourbron SP, Buckley DL. Classic models for dynamic contrast-enhanced MRI. *NMR Biomed.* 2013;26:1004–1027. doi: 10.1002/nbm.2940.
17. Ewing JR, Bagher-Ebadian H. Model selection in measures of vascular parameters using dynamic contrast-enhanced MRI: experimental and clinical applications. *NMR Biomed.* 2013;26:1028–1041. doi: 10.1002/nbm.2996.
18. Li X, Welch EB, Chakravarthy AB, et al. Statistical comparison of dynamic contrast-enhanced MRI pharmacokinetic models in human breast cancer. *Magn. Reson. Med. Off. J. Soc. Magn. Reson. Med. Soc. Magn. Reson. Med.* 2012;68:261–271. doi: 10.1002/mrm.23205.
19. Kallehauge JF, Tanderup K, Duan C, Haack S, Pedersen EM, Lindegaard JC, Fokdal LU, Mohamed SMI, Nielsen T. Tracer kinetic model selection for dynamic contrast-enhanced magnetic resonance imaging of locally advanced cervical cancer. *Acta Oncol. Stockh. Swed.* 2014;53:1064–1072. doi: 10.3109/0284186X.2014.937879.
20. Naish JH, Kershaw LE, Buckley DL, Jackson A, Waterton JC, Parker GJM. Modeling of contrast agent kinetics in the lung using T1-weighted dynamic contrast-enhanced MRI. *Magn. Reson. Med.* 2009;61:1507–1514. doi: 10.1002/mrm.21814.
21. Donaldson SB, West CML, Davidson SE, Carrington BM, Hutchison G, Jones AP, Sourbron SP, Buckley DL. A comparison of tracer kinetic models for T1-weighted dynamic contrast-enhanced MRI: application in carcinoma of the cervix. *Magn. Reson. Med. Off. J. Soc. Magn. Reson. Med. Soc. Magn. Reson. Med.* 2010;63:691–700. doi: 10.1002/mrm.22217.
22. Bagher-Ebadian H, Jain R, Nejad-Davarani SP, et al. Model selection for DCE-T1 studies in glioblastoma. *Magn. Reson. Med. Off. J. Soc. Magn. Reson. Med. Soc. Magn. Reson. Med.* 2012;68:241–251. doi: 10.1002/mrm.23211.
23. Chwang WB, Jain R, Bagher-Ebadian H, Nejad-Davarani SP, Iskander ASM, VanSlooten A, Schultz L, Arbab AS, Ewing JR. Measurement of rat brain tumor kinetics using an intravascular MR contrast agent and DCE-MRI nested model selection. *J. Magn. Reson. Imaging JMIR* 2014;40:1223–1229. doi: 10.1002/jmri.24469.
24. Draper NR, Smith H. *Applied regression analysis* 2nd ed. 1981.

25. Luyyaert R, Sourbron S, Makkat S, de Mey J. Error estimation for perfusion parameters obtained using the two-compartment exchange model in dynamic contrast-enhanced MRI: a simulation study. *Phys. Med. Biol.* 2010;55:6431.
26. Murase K. Efficient method for calculating kinetic parameters using T1-weighted dynamic contrast-enhanced magnetic resonance imaging. *Magn. Reson. Med.* 2004;51:858–862.
27. Jaynes ET. *Probability Theory: The Logic of Science*. Cambridge University Press; 2003.
28. Landis CS, Li X, Telang FW, Coderre JA, Micca PL, Rooney WD, Latour LL, Véték G, Pályka I, Springer CS. Determination of the MRI contrast agent concentration time course in vivo following bolus injection: Effect of equilibrium transcytolemmal water exchange. *Magn. Reson. Med.* 2000;44:563–574. doi: 10.1002/1522-2594(200010)44:4<563::AID-MRM10>3.0.CO;2-#.
29. Buckley DL, Kershaw LE, Stanisiz GJ. Cellular-interstitial water exchange and its effect on the determination of contrast agent concentration in vivo: Dynamic contrast-enhanced MRI of human internal obturator muscle. *Magn. Reson. Med.* 2008;60:1011–1019. doi: 10.1002/mrm.21748.
30. Fram EK, Herfkens RJ, Johnson GA, Glover GH, Karis JP, Shimakawa A, Perkins TG, Pelc NJ. Rapid calculation of T1 using variable flip angle gradient refocused imaging. *Magn. Reson. Imaging* 1987;5:201–208.
31. Kallehauge J, Nielsen T, Haack S, et al. Voxelwise comparison of perfusion parameters estimated using dynamic contrast enhanced (DCE) computed tomography and DCE-magnetic resonance imaging in locally advanced cervical cancer. *Acta Oncol.* 2013;52:1360–1368. doi: 10.3109/0284186X.2013.813637.
32. Sharma P, Socolow J, Patel S, Pettigrew RI, Oshinski JN. Effect of Gd-DTPA-BMA on blood and myocardial T1 at 1.5T and 3T in humans. *J. Magn. Reson. Imaging* 2006;23:323–330. doi: 10.1002/jmri.20504.
33. Gudbjartsson H, Patz S. The Rician Distribution of Noisy MRI Data. *Magn. Reson. Med. Off. J. Soc. Magn. Reson. Med. Soc. Magn. Reson. Med.* 1995;34:910–914.
34. Metropolis N, Rosenbluth AW, Rosenbluth MN, Teller AH, Teller E. Equation of State Calculations by Fast Computing Machines. *J. Chem. Phys.* 1953;21:1087–1092. doi: 10.1063/1.1699114.
35. Quarles CC, Gore JC, Xu L, Yankeelov TE. Comparison of dual-echo DSC-MRI- and DCE-MRI-derived contrast agent kinetic parameters. *Magn. Reson. Imaging* 2012;30:944–953. doi: 10.1016/j.mri.2012.03.008.
36. Li X, Huang W, Rooney WD. Signal-to-noise ratio, contrast-to-noise ratio and pharmacokinetic modeling considerations in dynamic contrast-enhanced magnetic resonance imaging. *Magn. Reson. Imaging* 2012;30:1313–1322. doi: 10.1016/j.mri.2012.05.005.
37. Yankeelov TE, Luci JJ, Lepage M, Li R, Debusk L, Lin PC, Price RR, Gore JC. Quantitative pharmacokinetic analysis of DCE-MRI data without an arterial input function: a reference region model. *Magn. Reson. Imaging* 2005;23:519–529.

38. Ledsam JR, Hodgson R, Moots RJ, Sourbron SP. Modeling DCE-MRI at low temporal resolution: A case study on rheumatoid arthritis. *J. Magn. Reson. Imaging* 2013;38:1554–1563. doi: 10.1002/jmri.24061.
39. Lim SW, Chrysochou C, Buckley DL, Kalra PA, Sourbron SP. Prediction and assessment of responses to renal artery revascularization with dynamic contrast-enhanced magnetic resonance imaging: a pilot study. *Am. J. Physiol. - Ren. Physiol.* 2013;305:F672–F678. doi: 10.1152/ajprenal.00007.2013.
40. Donaldson SB, Bonington SC, Kershaw LE, Cowan R, Lyons J, Elliott T, Carrington BM. Dynamic contrast-enhanced MRI in patients with muscle-invasive transitional cell carcinoma of the bladder can distinguish between residual tumour and post-chemotherapy effect. *Eur. J. Radiol.* 2013;82:2161–2168. doi: 10.1016/j.ejrad.2013.08.008.
41. Bains LJ, McGrath DM, Naish JH, Cheung S, Watson Y, Taylor MB, Logue JP, M. Parker GJ, Waterton JC, Buckley DL. Tracer kinetic analysis of dynamic contrast-enhanced MRI and CT bladder cancer data: A preliminary comparison to assess the magnitude of water exchange effects. *Magn. Reson. Med.* 2010;64:595–603. doi: 10.1002/mrm.22430.
42. Box GE, Draper NR. Empirical model-building and response surfaces. Wiley New York; 1987.
43. George ML, Dzik-Jurasz ASK, Padhani AR, Brown G, Tait DM, Eccles SA, Swift RI. Non-invasive methods of assessing angiogenesis and their value in predicting response to treatment in colorectal cancer. *Br. J. Surg.* 2001;88:1628–1636. doi: 10.1046/j.0007-1323.2001.01947.x.
44. Park JJ, Kim CK, Park SY, Simonetti AW, Kim E, Park BK, Huh SJ. Assessment of early response to concurrent chemoradiotherapy in cervical cancer: value of diffusion-weighted and dynamic contrast-enhanced MR imaging. *Magn. Reson. Imaging* 2014;32:993–1000. doi: 10.1016/j.mri.2014.05.009.
45. Kim J-H, Kim CK, Park BK, Park SY, Huh SJ, Kim B. Dynamic contrast-enhanced 3-T MR imaging in cervical cancer before and after concurrent chemoradiotherapy. *Eur. Radiol.* 2012;22:2533–2539.
46. Semple SIK, Harry VN, Parkin DE, Gilbert FJ. A Combined Pharmacokinetic and Radiologic Assessment of Dynamic Contrast-Enhanced Magnetic Resonance Imaging Predicts Response to Chemoradiation in Locally Advanced Cervical Cancer. *Int. J. Radiat. Oncol.* 2009;75:611–617. doi: 10.1016/j.ijrobp.2009.04.069.
47. Lim K, Chan P, Dinniwell R, et al. Cervical Cancer Regression Measured Using Weekly Magnetic Resonance Imaging During Fractionated Radiotherapy: Radiobiologic Modeling and Correlation With Tumor Hypoxia. *Int. J. Radiat. Oncol.* 2008;70:126–133. doi: 10.1016/j.ijrobp.2007.06.033.
48. Gandhi D, Hoeffner EG, Carlos RC, Case I, Mukherji SK. Computed tomography perfusion of squamous cell carcinoma of the upper aerodigestive tract: initial results. *J. Comput. Assist. Tomogr.* 2003;27:687–693.

49. Zhu AX, Holalkere NS, Muzikansky A, Horgan K, Sahani DV. Early antiangiogenic activity of bevacizumab evaluated by computed tomography perfusion scan in patients with advanced hepatocellular carcinoma. *The oncologist* 2008;13:120–125.
50. Hansen ML, Fallentin E, Lauridsen C, Law I, Federspiel B, Bæksgaard L, Svendsen LB, Nielsen MB. Computed tomography (CT) perfusion as an early predictive marker for treatment response to neoadjuvant chemotherapy in gastroesophageal junction cancer and gastric cancer-a prospective study. *PloS One* 2014;9:e97605.
51. Yang C, Stadler WM, Karczmar GS, Milosevic M, Yeung I, Haider MA. Comparison of quantitative parameters in cervix cancer measured by dynamic contrast-enhanced MRI and CT. *Magn. Reson. Med.* 2010;63:1601–1609.
52. Parker GJM, Roberts C, Macdonald A, Buonaccorsi GA, Cheung S, Buckley DL, Jackson A, Watson Y, Davies K, Jayson GC. Experimentally-derived functional form for a population-averaged high-temporal-resolution arterial input function for dynamic contrast-enhanced MRI. *Magn. Reson. Med.* 2006;56:993–1000. doi: 10.1002/mrm.21066.

Chapter 3 Modeling Dynamic-Contrast Enhanced MRI data with a Constrained Local Arterial Input Function¹

3.1 Introduction

Dynamic contrast-enhanced (DCE)-MRI, which involves monitoring the MRI signal dynamically after intravenous injection of a paramagnetic contrast agent (CA) bolus, is widely employed in the evaluation of tissue perfusion and vascular permeability [1–3]. Tracer kinetic modeling of the acquired MRI signal time-course provides parameters describing the underlying physiology of the tissue of interest [4]. The estimated physiological parameters, including forward volume transfer constant (K^{trans}), permeability-surface area product (PS), tissue-volume-normalized volumetric blood plasma flow rate (F_p), hereafter “blood plasma flow”, plasma volume fraction (v_p), and extracellular-extravascular volume fraction (v_e) have been successfully employed in the characterization of cancerous tissues and the assessment of therapeutic response [5, 6].

Quantitative tracer kinetic modeling of DCE-MRI data requires modeling of the tissue response function and knowledge of the CA concentration in the blood plasma at the capillary inlet of any region of interest (ROI), referred to as the arterial input function (AIF) [4]. AIFs can be difficult to measure experimentally and population-averaged AIFs are sometimes used to circumvent these difficulties [7]. However, due to inter-individual variability of the vascular bed, the use of a directly measured AIF for each subject is often the preferred approach for clinical studies [8].

¹ All contents in this chapter have been published in Duan C, Kallehauge JF, Pérez-Torres CJ, Bretthorst GL, Beeman SC, Tanderup K, Ackerman JJH, and Garbow JR. Modeling Dynamic Contrast-Enhanced MRI data with a Constrained Local AIF. *Mol Imaging Biol* (2017). doi:10.1007/s11307-017-1090-x.

The actual AIF at the capillary inlet of any given tissue of interest is both delayed and dispersed relative to the remote-AIF measured directly from a major feeding (upstream) vessel [9]. In what follows, the directly measured remote-AIF is hereafter referred to as the R-AIF. Significant error in quantitative kinetic parameter estimation can be introduced if AIF bolus delay and dispersion are not taken into account [10–13]. Methods to account for delay include aligning the tissue response curve and the R-AIF to a common bolus arrival time [14] or incorporating an arrival time delay (offset time) parameter within the tracer kinetic model’s tissue response function [15]. Nevertheless, accounting for dispersion remains a challenge for quantitative DCE-MRI data analysis. In the case of tumor tissue, in which the vasculature is widely known to be structurally and functionally abnormal (i.e., leaky, tortuous, dilated, and saccular, with a haphazard pattern of interconnections and large holes in vessel walls), a single global R-AIF is likely to be a poor approximation to the desired voxel-specific AIF. Further, due to MRI experimental limitations (e.g., practically achievable spatial and temporal resolution), partial volume and other effects can also lead to a significant error in correctly assessing the time-dependent amplitude of the R-AIF [16]. Nonetheless, while imperfect, the R-AIF represents a “best possible” first approximation to the “true” AIF. Employing an inferred local-AIF for each individual voxel, one that can correct the R-AIF for voxel-specific bolus amplitude error and arrival-time delay, should improve quantitative modeling of DCE-MRI data.

The goal of this study was to compare DCE-MRI data modeling employing (i) a R-AIF and (ii) an inferred, constrained local-AIF (cL-AIF, *vide infra*) against both *in silico* DCE-MRI data and clinical cervical cancer DCE-MRI data. Herein, we describe a flexible analytical function that models well the measured R-AIFs obtained from the external iliac artery of patients with advanced stage cervical cancer. A Bayesian-based, Markov chain Monte Carlo (MCMC) parameter

estimation approach is employed to infer each tumor’s voxel-specific cL-AIFs based on the patient’s R-AIF. Our work builds on AIF modeling reported previously by Fluckiger *et al.* [17, 18] and Lee *et al.* [19]. A key difference herein is that the cL-AIF model (functional form) is constrained based on an empirical fixed-parameterization of the R-AIF measured for each patient – to reduce the model complexity, only cL-AIF bolus amplitude and arrival time are free parameters – allowing for precise (i.e., stable) tracer kinetic model parameter estimation.

3.2 Materials and Methods

3.2.1 Clinical DCE-MRI Data

All Clinical cervical cancer DCE-MRI data were acquired from patients enrolled in EMBRACE (<https://www.embracestudy.dk/>), an international study on MRI-guided brachytherapy in locally advanced cervical cancer. All studies were approved by the local medical ethics research board. Sixteen patients with locally advanced-stage cervical tumor were scanned prior to radiotherapy. All DCE-MRI data were acquired on a 3T Philips Achieva scanner using a 3D, saturation-recovery, spoiled gradient-echo sequence (TR/TE = 2.9/1.4 ms, saturation time = 25 ms, flip angle = 10°). A bolus of 0.1 mmol/kg Dotarem® (gadoterate meglumine; Guerbet, France) was injected at 4 ml/s, followed by a 50 ml saline flush. For each patient, 120 dynamic axial scans (18 baseline scans, baseline signal-to-noise \approx 5:1) were obtained with 2.1 seconds temporal resolution and 2.3 x 2.3 mm² in-plane resolution (matrix size = 176 x 176, FOV = 405 x 405 mm², 20-24 slices with a slice thickness of 5 mm) following the administration of CA. The acquired MR images were smoothed as described in Korporaal *et al.* [15]. A pre-contrast T₁ map was produced *via* the variable flip angle method (5°, 10°, 15°, 20°, and 25°), using a spoiled gradient echo sequence (TR/TE = 20/1.7 ms), with the same resolution and orientation as the DCE scans. MR signal intensities were then converted to CA concentration using the T₁ map, as described in Kallehauge

et al. [20]. Because of the short TE, effects of T_2^* dephasing are minimal and were ignored in the conversion. Cervical tumor tissues were segmented based upon TSE T_2 -weighted images (TR/TE = 4236/100 ms, Flip angle = 90° , Slice thickness = 3 mm, In-plane resolution = $0.94 \times 0.94 \text{ mm}^2$, matrix size = 320×320) by an experienced radiologist. An R-AIF was obtained experimentally for each patient by averaging multiple CA-concentration *vs.* time curves measured in the external iliac artery. The chosen measurement locations were unaffected by flow disturbances near the bifurcation of the external/internal artery. A literature value of 1660 ms [21] was used for the pre-contrast blood T_1 .

3.2.2 *In silico* DCE-MRI Data

In silico DCE-MRI data were simulated based on clinical DCE-MRI data from a representative cervical cancer patient. For this patient, a whole-tumor, average DCE-MRI CA concentration *vs.* time curve was calculated and then modeled using the corresponding R-AIF for that patient. The estimated parameter values, together with the measured R-AIF, were used to simulate a noiseless DCE-MRI curve. Thus, for the noiseless simulated data, the correct (true) AIF is known.

In this representative simulation, the temporal resolution (2.1 s) and the total acquisition time (250 s) were identical to those of the clinical DCE-MRI data. Normally distributed Gaussian noise, with standard deviation (SD) ranging from 0 mM to 0.05 mM with a step size of 0.002 mM, was added to the initially noiseless simulated data. For each noise SD, 100 different noise representations were simulated. As reference, the baseline noise SD of the DCE-MRI data for the sixteen cervical cancer patients is $\sim 0.04 \text{ mM}$.

While only one set of representative CTUM parameter values was employed in the simulation study, the global findings regarding accuracy and precision of parameter estimation are instructive,

and not subtle. Further, considering the voxel-wise analysis of clinical cervical cancer data, Bayesian-based model selection and parameter estimation naturally compares the cL-AIF and traditional R-AIF approaches over the entire parametric range representative of heterogeneous tumor tissue. Clinical cervical cancer DCE-MRI data were acquired from patients enrolled in EMBRACE (<https://www.embracestudy.dk/>), an international study on MRI-guided brachytherapy in locally advanced cervical cancer. All studies were approved by the local medical ethics research board. Sixteen patients with locally advanced-stage cervical tumor were scanned prior to radiotherapy. All DCE-MRI data were acquired

3.2.3 DCE-MRI tracer kinetic modeling

Tracer kinetic modeling of the administrated CA assumes that the tissue CA concentration $C_t(t)$ can be expressed as:

$$C_t(t) = F_p \cdot \int_0^t R(t - \tau) \cdot C_a(\tau) d\tau, \quad [1]$$

where F_p is blood plasma flow (s^{-1}), $R(t)$ is the tissue impulse response residue function, and $C_a(t)$ is the AIF.

Many tracer kinetic models (i.e., the tissue response residue function, $R(t)$) have been applied to describe the behavior of administrated CA in DCE-MRI experiment. In a previous study [22], the three-parameter compartmental tissue uptake model (CTUM) was found to be the most probable model for the same advanced stage cervical cancer patient population, and was, thus, employed in this study. The impulse response residue function for the CTUM is:

$$R(t) = (1 - E) \cdot e^{-\gamma t} + E, \quad [2]$$

where E is the CA extravasation fraction, and γ is the inverse of the plasma mean transit time, i.e., γ is the governing rate constant. Plasma volume (v_p) and permeability-surface-area-product (PS) can be calculated from F_p , E and γ . Further details are provided in Sourbron *et al.* [4].

3.2.4 A gamma-variate local-AIF model

Recently, Lee *et al.* [19] introduced a strategy for inferring the voxel-specific local-AIF in dynamic susceptibility contrast (DSC)-MRI employing a three-component local-AIF model. The CA concentrations of the primary and first recirculation bolus were each modeled (empirically parameterized) with a normalized gamma distribution function, Eq. [3]. An additional (third) term, which accounts for a steady-state circulation phase, completed the local-AIF model, Eq. [4]:

Gamma
distribution:

$$G(\alpha, \beta, t_1, t) = \frac{1}{\beta^{\alpha+1} \times \Gamma(\alpha + 1)} \times (t - t_1)^\alpha \times e^{-\frac{t-t_1}{\beta}} \quad [3]$$

Local-AIF
model:

$$C_a(t) = \sum_{i=1}^2 C_i G(\alpha, \beta, t_i, t) + C_3 (1 - e^{-r(t-t_1)}) \quad [4]$$

Note: the shape of the primary and recirculation CA boluses in this local-AIF are the same, i.e., they are defined by the same-valued gamma-distribution parameters (α and β), but have different amplitudes, C_i , and arrival times, t_i . We have extended this strategy to DCE-MRI data and modified the local-AIF model of Lee *et al.* [19] by adding an exponential decay term, with decay-rate constant δ , to account for renal clearance of CA over time, which is not negligible for DCE-MRI due to the much longer acquisition time compared to DSC-MRI:

$$C_a(t) = \left(\sum_{i=1}^2 C_i G(\alpha, \beta, t_i, t) + C_3 (1 - e^{-r(t-t_1)}) \right) \times e^{-\delta(t-t_1)} \quad [5]$$

Table 3.1 summarizes all the parameters introduced in Eqs. [3-5].

Table 3.1: Summary of Parameters Used in the cL-AIF Model.

Parameter	Description	Unit
α	Gamma distribution shape parameter	None
β	Gamma distribution rate parameter	None
t_1	Main CA bolus arrival time	sec
t_2	Recirculated CA bolus arrival time	sec
C_1	Main CA bolus amplitude	mM
C_2	Recirculated CA bolus amplitude	mM
C_3	Steady-state circulation amplitude	mM
r	Steady-state circulation rate constant	sec ⁻¹
δ	CA renal-clearance rate constant	sec ⁻¹

3.2.5 A constrained local-AIF model

A widely-acknowledged weakness of much reported DCE modeling is that the obtained AIF is generally remote from the tissue of interest. Given that the voxel-specific local AIF must *a priori* differ substantially from an AIF measured from a major, remote, upstream artery and that, to first order, this will be reflected in bolus arrival time and amplitude of an analytical representation of the measured AIF, a constrained local-AIF model was derived based on empirical parameterization, *via* Eq. [5], of the patient-specific R-AIF:

- i. First, the modified gamma-variate formulation, Eq. [5], was employed to model the R-AIF for each patient, yielding estimates of all model parameters.
- ii. Second, the patient-specific R-AIF model was constrained by accepting and fixing the values of all model parameters to the estimates obtained in (i).
- iii. Third, the formulation of the local-AIF model was completed by introducing two free parameters: a bolus delay, Δt , and a scaling factor, s . These two free parameters provide, respectively, for a patient-voxel-specific shift in the two bolus arrival times (same time shift for the primary and recirculation boluses) and for a scaling of the two bolus amplitudes (same amplitude scaling for the primary and recirculation boluses):

$$t'_1 = t_1 + \Delta t; t'_2 = t_2 + \Delta t; C'_1 = s \times C_1; C'_2 = s \times C_2 \quad [6]$$

Note that the scaling factor, s , modifies only the two bolus amplitudes (C_1 and C_2), rather than the whole local-DCE-AIF. C_3 is a global term representing the long-term, steady-state CA concentration throughout the entire vascular system and is, thus, left unchanged (i.e., when t is large, $C_a(t)$, Eq [5], reduces to C_3 , ignoring renal clearance). Thus, C_3 is a patient-specific global parameter; it is not voxel-specific.

Possible variation in the bolus shape (e.g., broadening) is neglected in the local-AIF formulation to reduce model complexity (i.e., inclusion of possible voxel-specific bolus shape changes by estimating voxel-specific values for α and β in the local-AIF model would introduce more free parameters than are supported by data quality, see the modeling results employing the unconstrained local-DCE-AIF approach, *vide infra*).

- iv. Finally, the constrained local-AIF model, including bolus delay, Δt , and scaling factor, s , as voxel-specific free parameters, hereafter referred to as cL-AIF, and Eq. [2] were substituted into Eq. [1], and the convolution was evaluated numerically. Posterior probabilities for all free parameters were computed voxel-by-voxel using Bayesian probability theory [23].

Figure 1a shows the modeling of a representative R-AIF from a cervical cancer patient employing the modified gamma-variate formulation, Eq. [5]. Figure 1b, an expansion of the plot in panel a, shows a sample cL-AIF, illustrating the effects of the two free additional parameters, bolus delay, Δt , and amplitude scaling factor, s , introduced to complete the cL-AIF model.

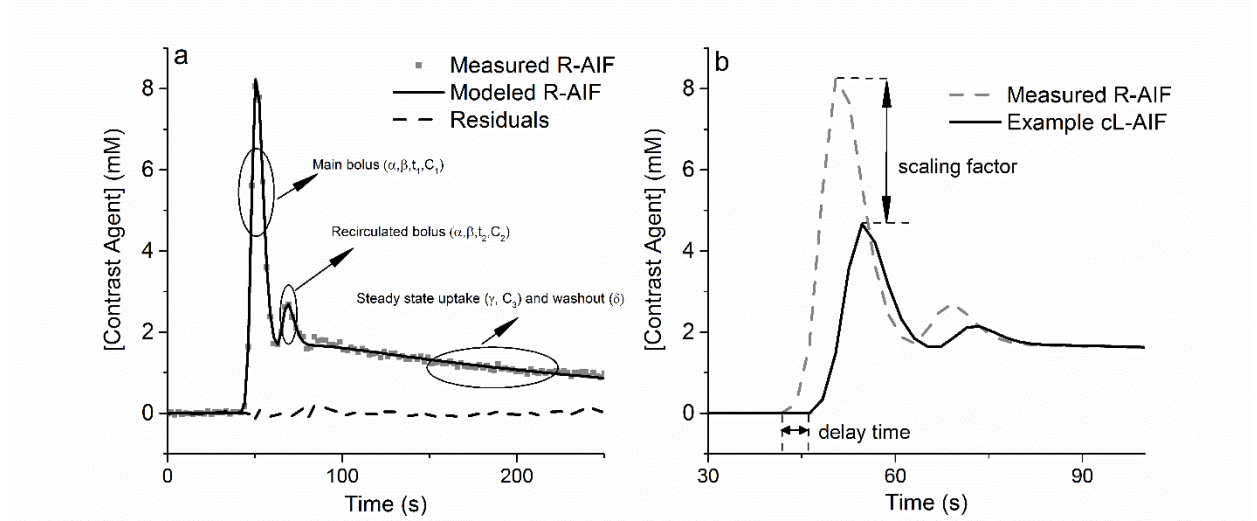


Figure 3.1: Representative R-AIF and cL-AIF. Panel a: Modeling of an example R-AIF measured from the external iliac artery of a cervical cancer patient. The arrows indicate the three components in the local-DCE-AIF model, Eq. [5]. **Panel b:** Expansion of the measured R-AIF shown in Panel a (dashed line) and an example cL-AIF (solid black line) based on this measured R-AIF. The arrows indicate the bolus delay time, Δt , and scaling factor, s , in the cL-AIF model (Eq. [6]).

3.2.6 Data analysis

Both clinical cervical cancer DCE-MRI data and *in silico* DCE-MRI data were modeled with three representations of the AIF:

- i. The R-AIF: As is often done in conventional DCE modeling, an offset time constant was incorporated into the tracer kinetic tissue response function (i.e., the CTUM, Eq. [2]), to account for bolus delay (i.e., a total of four parameters). However, in the simulation study, the same R-AIF employed in the generation of the *in silico* data was also used for CTUM parameter estimation (i.e., by definition, the correct AIF was “known”). Thus, in the simulation studies, the bolus delay was zero.
- ii. The uL-AIF: An unconstrained local-DCE-AIF model, described by the Eq. [5] formulation with all parameters considered as “free” (requiring estimation), was directly substituted into Eq. [1]. All of the parameters in the uL-AIF model (α , β , t_1 , t_2 , C_1 , C_2 , C_3 , γ , and δ) and in the CTUM (F_p , PS and v_p) were estimated simultaneously from the CA concentration *vs.* time curves (i.e., a total of 12 parameters). Note: the free parameters t_1 and t_2 in the uL-AIF eliminate the need for an additional bolus delay parameter, as is employed with the R-AIF.
- iii. The cL-AIF: Free parameters Δt and s represent bolus arrival time delay and amplitude of the cL-AIF, designed to be voxel-specific, which was otherwise constrained by fixed parameterization *via* Eq. [5] modeling of the R-AIF. The cL-AIF was substituted into Eq. [1], and Δt and s , and the parameters in the CTUM (F_p , PS and v_p) were estimated (i.e., a total of five parameters).

For the cervical cancer DCE-MRI data, a data-driven Bayesian probability theory-based model selection algorithm (*vide infra*) was employed to compare use of the R-AIF and cL-AIF on a voxel-by-voxel basis. Traditional (frequentist) statistical analyses were performed using Matlab (The Mathworks, Inc., Natick, MA). A two-sided Wilcoxon signed rank test was used to compare kinetic parameters estimated employing the R-AIF and the cL-AIF. Statistical significance was established by $P < 0.05$.

3.2.7 Bayesian model selection

For the cervical cancer DCE-MRI data, a data-driven Bayesian model selection algorithm was employed to compare use of the R-AIF and cL-AIF, on a voxel-by-voxel basis. The posterior probability of a model, M , given the data, D , and all of the prior information, I , is given by Bayes' theorem:

$$P(M|DI) = \frac{P(M|I)P(D|MI)}{P(D|I)} \quad [1]$$

where $P(M|DI)$ is the posterior probability for the model, M , given the data, D , and all of the prior information, I . On the right-hand side of this equation, $P(M|I)$ is the prior probability for the M' th model and $P(D|MI)$ is the marginal direct probability for the data, given the model and the prior information. Finally, $P(D|I)$ is the direct probability for the data, given the prior information, and serves as a normalization constant.

The prior probability for the model, $P(M|I)$, is assigned as a uniform prior in this calculation:

$$P(M|I) = \frac{1}{m} \quad [2]$$

in which m is the number of models. In Eq. [1], $P(D|MI)$ is a marginal direct probability because none of the parameters from model M appear. This marginal direct probability can be computed if we reintroduce the model parameters, Ω (a vector):

$$P(D|MI) = \int d\Omega P(D|\Omega MI) = \int d\Omega P(\Omega|MI)P(D|\Omega MI) \quad [3]$$

where $P(\Omega|I)$ is the joint prior probability for the model parameters Ω , and $P(D|\Omega MI)$ is the direct probability for the data (i.e., the likelihood function), given the model parameters, Ω , the model, M , and the prior information, I .

The joint prior probability for the model parameters can be factored into an independent prior probability for each parameter (v is the number of parameters in the current model):

$$P(\Omega|I) = \prod_{k=1}^v P(\Omega_k|I) \quad [4]$$

The direct probability for the data, $P(D|\Omega MI)$, is the likelihood function for the data D . Each data set consists of N data values, so $D \equiv \{d(t_1), \dots, d(t_N)\}$, where $d(t_i)$ is a data item sampled at abscissa value t_i . This direct probability is assigned using a Gaussian prior probability for the noise; the likelihood for a single dataset then becomes:

$$P(D|\sigma\Omega MI) = (2\pi\sigma^2)^{-\frac{N}{2}} \times \exp\left(-\frac{Q^2}{2\sigma^2}\right) \quad [5]$$

where the standard deviation, σ , has been added. The total squared residual, Q^2 , is defined as:

$$Q^2 = \sum_{i=1}^N [d(t_i) - M(t_i, \Omega)]^2 \quad [6]$$

Finally, substituting Eqs. [2-6] into Eq. [1], one obtains:

$$P(M|DI) \propto \int \frac{1}{m} \times \prod_{k=1}^v P(\Omega_k|I) \times (2\pi\sigma^2)^{-\frac{N}{2}} \times \exp\left(-\frac{\sum_{i=1}^N [d(t_i) - M(t_i, \Omega)]^2}{2\sigma^2}\right) d\Omega \quad [7]$$

in which the normalization constant, $P(D|I)$, has been dropped. All model selection calculations were performed using a custom-written Bayesian Data-Analysis Toolbox (documentation available at <http://bayesiananalysis.wustl.edu>). Markov chain Monte Carlo (MCMC) simulation was employed to numerically approximate this multi-dimensional integral, Eq. [7]. Initial values

for all of the parameters, including the model indicator, were sampled from the prior probabilities for each parameter and the model indicator. Uniformly distributed prior probabilities (see Supplementary Figure S1 for a model selection sensitivity analysis investigating the effect of prior distribution parameters on the model selection result) were assigned to each of the parameters, bounded by appropriate physiological ranges.

In this MCMC calculation, the model is varied by proposing a new model indicator and then simulating (i.e., drawing samples for) the new model parameters. After this new proposed model has reached equilibrium, i.e., the distributions of the drawn model parameter values in MCMC are stationary, the proposed model is either accepted or rejected using the Metropolis-Hastings acceptance criteria. If the proposed model is accepted, that simulation step is complete. However, if the proposed model is rejected, the calculation returns to the original model and new values for the model parameters are proposed. At the completion of the calculation, the posterior probabilities for all of the models and their parameters are approximated by the distributions of the Markov chain samples.

3.3 Results

The simulation study (Figure 3.2) evaluates the accuracy (mean relative error, i.e., mean of the absolute error divided by the exact value), and precision (variance of the relative error) of CTUM parameter estimation for the simulated data employing: (i) the correct AIF, i.e., the R-AIF used to generate the *in silico* data, (ii) the uL-AIF, and (iii) the cL-AIF.

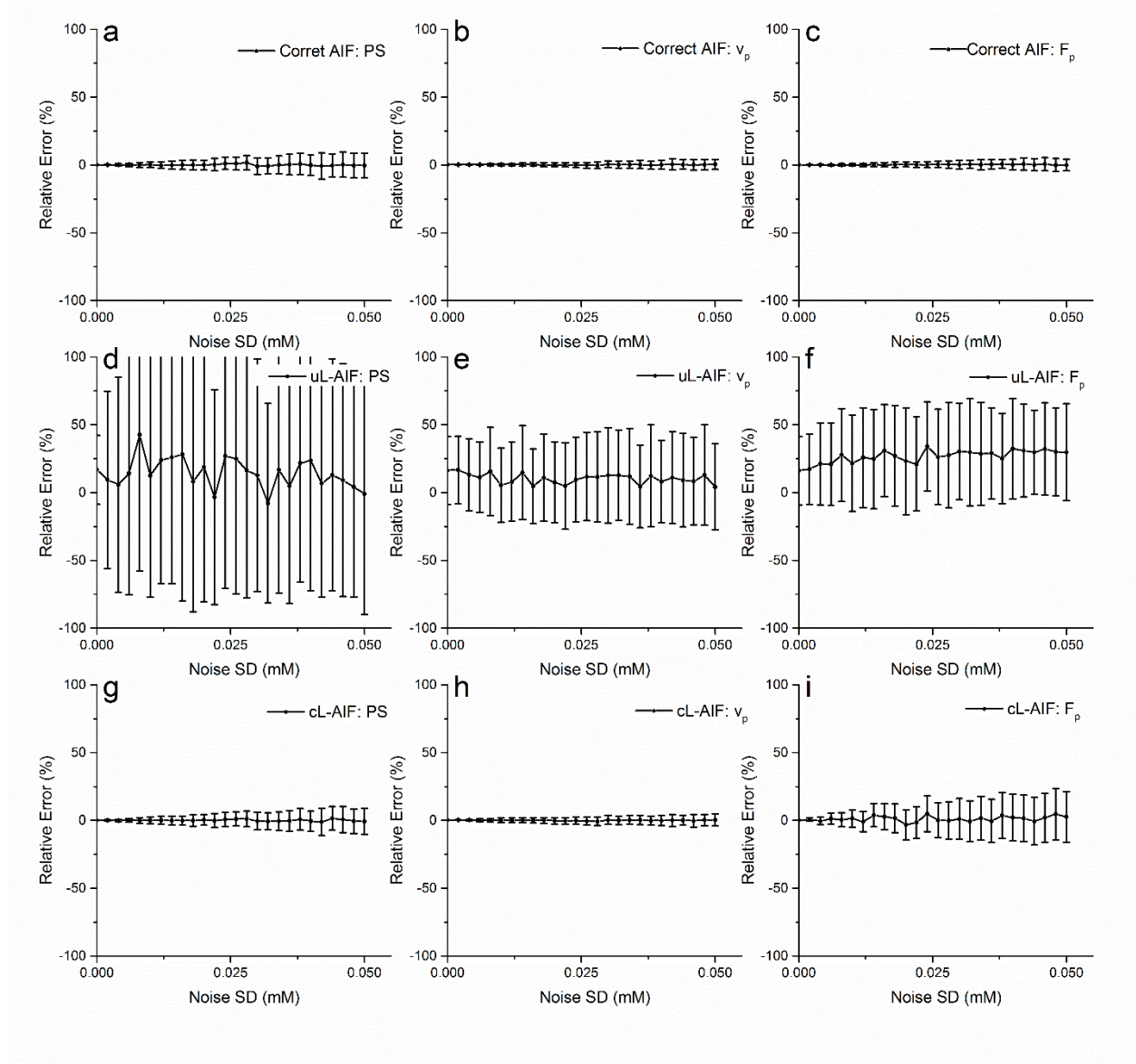
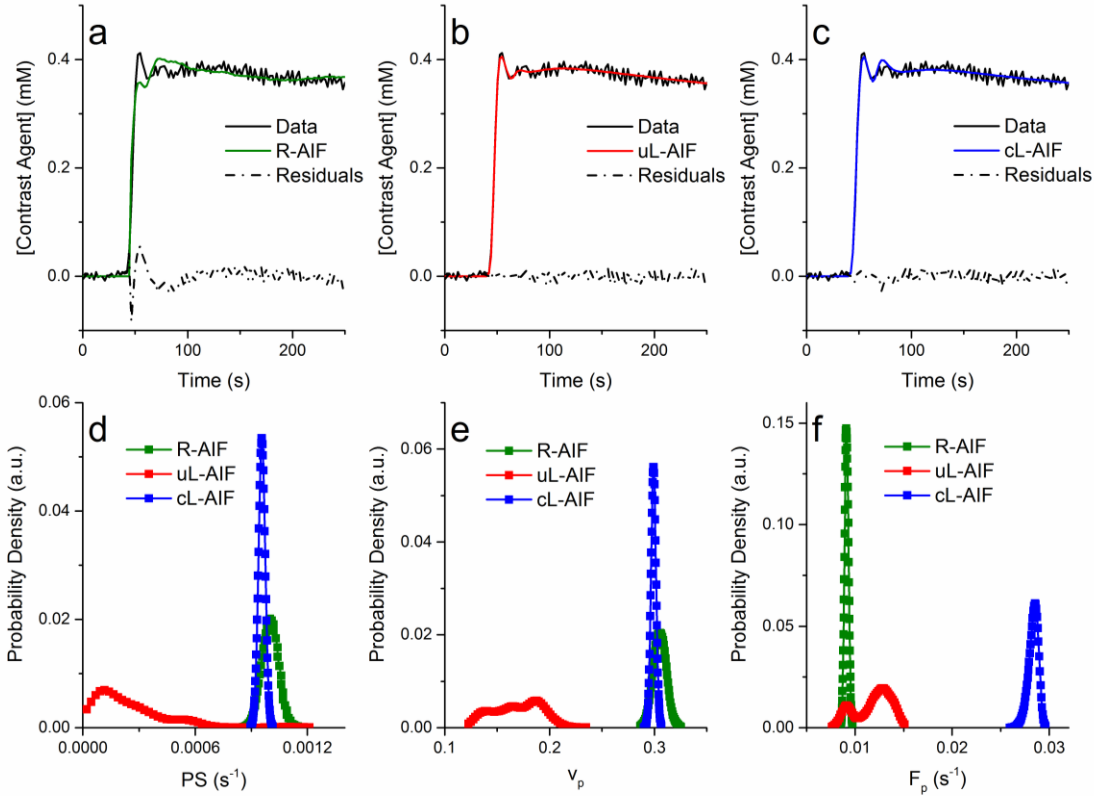


Figure 3.2: Simulation study comparing the accuracy and precision of CTUM parameter estimation. Three AIF modeling approaches ((i) the correct AIF (**Panels a - c**), (ii) the uL-AIF (**Panels d - f**), and (iii) the cL-AIF (**Panels g - i**.) were compared. Relative error is defined as the difference between the estimated value and the true value divided by the true value. Error bars indicate the standard deviation of the relative errors from 100 different noise representations at a given noise standard deviation.

When the correct AIF was used, the accuracy of estimation of all three CTUM parameters (PS , v_p and F_p) was relatively insensitive to added noise power, while precision decreased slowly (and linearly) as signal-to-noise decreased. However, when the uL-AIF model was employed in the data

analysis, despite minimal residuals, the correct CTUM parameter values could not be estimated accurately and the variance of the parameter estimation was large (precision was low), even for very small added noise power. By contrast, the accuracy of CTUM parameter estimation remains stable as noise level increases when the data are modeled using the cL-AIF and the precision of the parameter estimates approaches that derived using the correct AIF. In this scenario, the estimated scaling factor and delay time have the correct mean values of one and zero, respectively, with increasing uncertainty as contrast-to-noise ratio decreases.



*Figure 3.3: Comparison of the use of R-AIF vs. uL-AIF vs. cL-AIF in modeling of a representative dataset. **Panels a - c:** Tracer kinetic modeling (CTUM) of a representative single-voxel cervical cancer DCE-MRI dataset employing: (i) the R-AIF (**Panel a**), (ii) the uL-AIF (**Panel b**), and (iii) the cL-AIF (**Panel c**). The tissue CA concentration curves (data) are shown in black, the models in green, red, and blue (Panels a, b, and c, respectively), and the residuals (the difference between model and data) as black dashed-dotted lines. **Panels d - f:** corresponding posterior probability functions for PS (**Panel d**), v_p (**Panel e**), and F_p (**Panel f**), estimated from the modeling shown in **Panels a - c**. Probability density functions (PDFs) for parameters estimated using the R-AIF are*

shown in green, PDFs for parameters estimated using the uL-AIF are shown in red, and PDFs for parameters estimated using the cL-AIF are shown in blue. These PDFs are normalized so that the integrations of the PDF (area under the curve) are the same for each parameter.

Figure 3.3 compares the use of R-AIF vs. uL-AIF vs. cL-AIF in the modeling of a representative, single-voxel, cervical cancer DCE-MRI dataset. The use of the R-AIF does not model the DCE data well, especially for the initial rise of the CA concentration. The voxel-specific uL-AIF approach provides the smallest systematic deviations in the residuals. However, the *in silico* simulation study clearly identifies the so obtained CTUM parameter estimates as unreliable (*vide supra*). Use of the voxel-specific cL-AIF models the data well, with small residuals approaching those of the uL-AIF. Figure 3.3d - f show the posterior probability density functions (PDFs) for each of the three estimated CTUM parameters employing the three different AIFs. MCMC calculations employing both the R-AIF and the cL-AIF converged well (i.e., narrow PDFs, thus small uncertainties). Despite the smallest residuals, but entirely consistent with the *in silico* simulations, CTUM parameters were poorly determined (i.e., characterized by wide PDFs, thus large uncertainties) when the uL-AIF was employed.

Next, both the R-AIF and the cL-AIF were employed to analyze all the DCE-MRI data from sixteen patients with advanced stage cervical cancer, on a voxel-by-voxel basis. Figure 3.4 shows the pharmacokinetic parametric (F_p , PS , and v_p) maps and corresponding uncertainty maps estimated for a representative transverse tumor slice, employing either the R-AIF or the cL-AIF. The voxel-wise uncertainty for each parameter was computed using the standard deviation of the MCMC samples (i.e., the width of the PDF) divided by the mean parameter value. The F_p estimated using the cL-AIF is substantially larger than that estimated using the R-AIF.

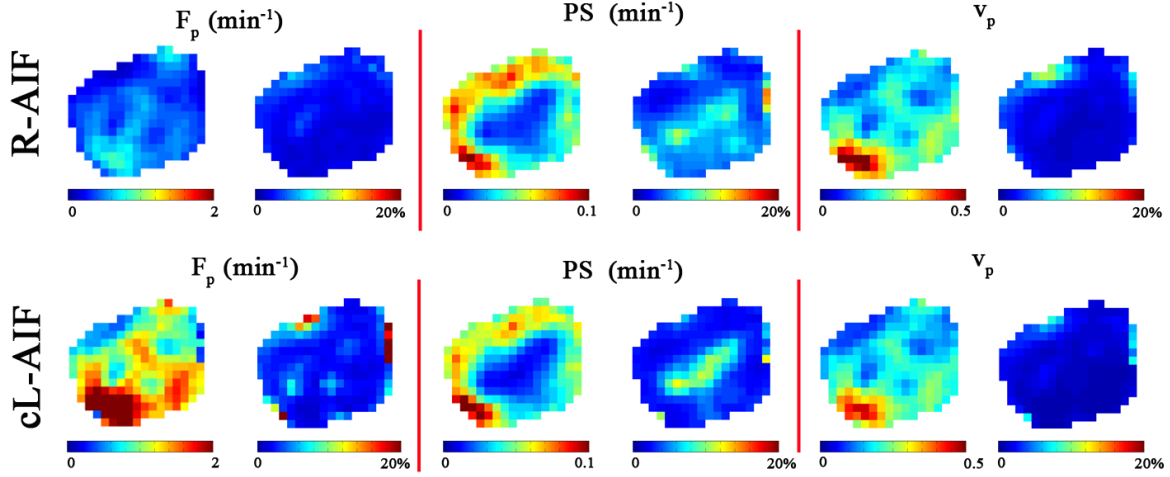


Figure 3.4: Parametric maps (left map of each pair) and corresponding uncertainty maps.

Regarding the delay and amplitude scaling parameters, Figure 4 shows maps of the delay time, Δt (Panel a), and scaling factor, s (Panel b), estimated for the same tumor slice shown in Figure 3. As expected for highly heterogeneous tumor tissues, the bolus amplitudes and arrival times vary from voxel-to-voxel. The median delay time and the median scaling factor across all tumor voxels for each of the sixteen subjects are shown in the boxplots (Panels d & e) of Figure 4. The scaling factors for 14 out of 16 patients are less than 1 (i.e., lower amplitude than the R-AIF), while the scaling factors for the other two patients are larger than 1 (i.e., higher amplitude than the R-AIF). This latter finding is likely due to partial volume effects in the direct measurement of the R-AIF, which can lead to underestimation of the true CA concentration. Voxel-wise, Bayesian model selection compared the R-AIF and cL-AIF in the modeling of the cervical cancer DCE-MRI data. Figure 4 shows the preferred-model map for the same tumor slice (Panel c), and the mean preferred-model percentage across the sixteen cervical cancers patients (Panel f). The cL-AIF approach is more probable than the R-AIF approach, with respective model voxel-count percentages of $78\% \pm 14\%$ vs. $22\% \pm 14\%$ (mean \pm SD, $n = 16$).

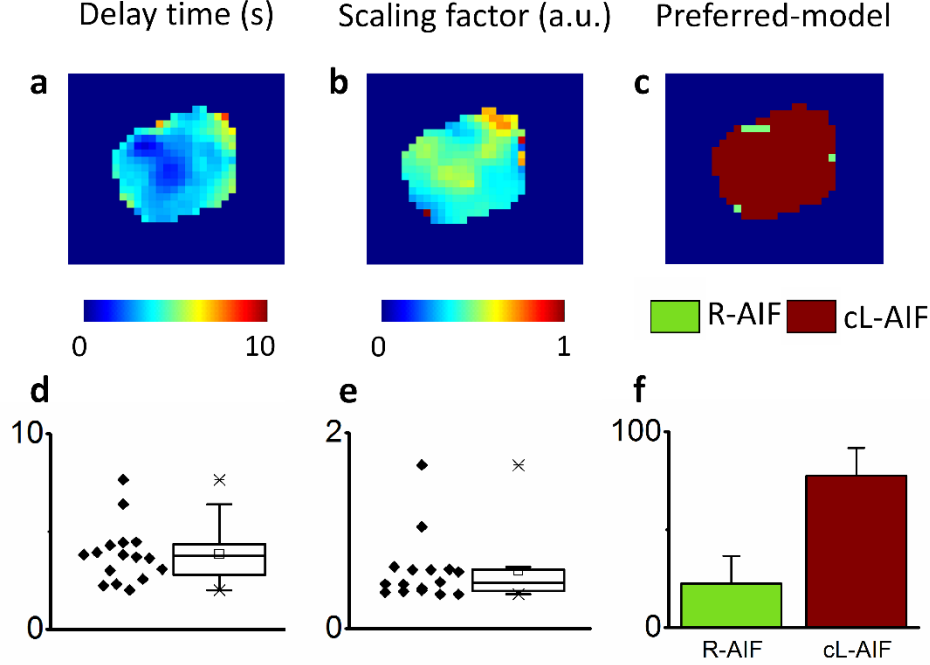


Figure 3.5: Estimations of the delay time and scaling factor, and model selection. **Panels a & b:** delay time (**Panel a**) and scaling factor (**Panel b**) maps estimated for an example tumor slice employing the cL-AIF. **Panel c:** model-selection (R-AIF vs. cL-AIF) preferred model map for the same tumor slice. **Panels d & e:** median delay time (**Panel d**) and scaling factor (**Panel e**) estimated using the cL-AIF for each of the sixteen patients. **Panel f:** mean preferred-model percentage across all DCE-MRI data for the sixteen patients. Error bars indicate the standard deviation of the preferred model percentages across the sixteen cervical tumors.

3.4 Discussion

Quantitative analysis of DCE-MRI is challenging because of difficulties in obtaining an accurate and appropriate AIF for tracer kinetic modeling. Furthermore, given CA bolus delay and dispersion, and the structurally and functionally abnormal vasculature characteristic of cancer, a single R-AIF is unlikely to approximate well the CA input for every voxel within the tumor ROI. In this study, we demonstrated the feasibility of using a voxel-specific, inferred cL-AIF, based on fixed parameterization of the R-AIF measured from a large, feeding (“remote”) artery with inclusion of two additional free parameters, bolus time-delay, Δt , and amplitude-scaling, s , to better model the DCE-MRI data in a voxel-by-voxel fashion.

In conventional DCE-MRI modeling, an offset time is often incorporated into the tissue response function to account for the delay in the arrival of the CA bolus at the tissue of interest. However, the inclusion of an offset time alone in the modeling may not be enough to fit the acquired DCE data (Figure 3.3a). To account for the CA dispersion, two approaches can be used. As pointed out by Calamante *et al.* [9], in principle, it should be possible to correct the R-AIF by employing a vascular transition function (VTF), in which the bolus transition process is described by modeling the vascular bed. Such a model, if it exists, would be quite complex, and it is unknown whether such a model would be well supported by the acquired DCE-MRI data. A simplified, mono-exponential, VTF model [24] only improves the fitting marginally compared to the direct use of the R-AIF, whereas the improvement is substantial when the cL-AIF is employed (see Figure 3.6).

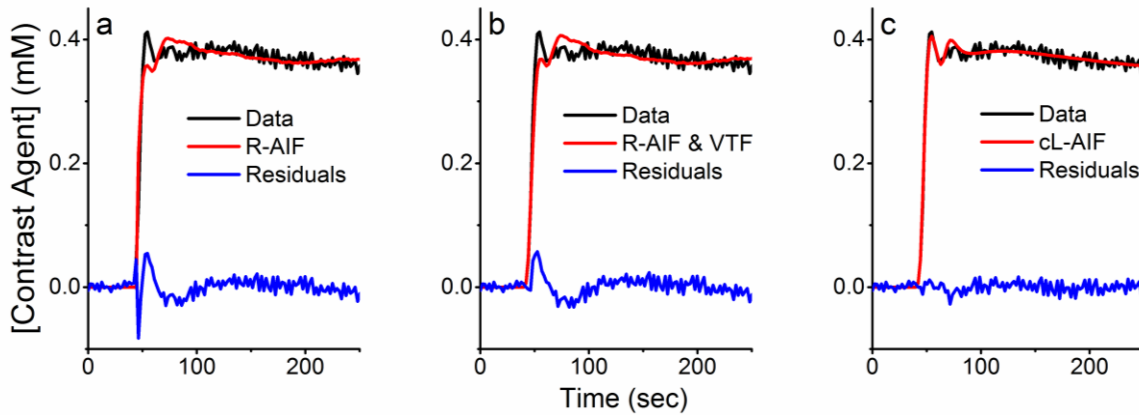


Figure 3.6: Modeling of a representative cervical cancer DCE-MRI dataset employing three AIFs. **Panel a**, the measured R-AIF; **Panel b**, the measured R-AIF as corrected by a single exponential VTF (i.e., $VTF(t) = \beta e^{-\beta t}$); **Panel c**, the cL-AIF. The squared residuals for the three methods are 0.0319, 0.0271, and 0.0086 mM^2 , respectively.

Estimating a local-AIF for the tissue of interest is an alternative approach to the use of a VTF. Blind deconvolution, which simultaneously estimates the local-AIF and the tracer kinetic parameters from the tissue CA concentration vs. time curves, has been proposed. Fluckiger *et al.* [17, 18] showed that constraining the input function to a particular functional form (i.e., a local-

AIF model) yields more accurate parameter estimation compared to deconvolution without a specific AIF model. In Fluckiger *et al.* [18], *k*-means clustering tissue curves were calculated and employed in a deconvolution to estimate a single, tumor-wide AIF or regional AIF (region size $< 10 \times 10 \times 10$ voxels). The estimated AIF was then used to estimate voxel-specific tracer kinetic parameters. However, such an estimated AIF is still not a voxel-specific local-DCE-AIF, especially in the presence of the structurally and functionally abnormal vasculature of tumor tissues.

In the first part of our study, an uL-AIF based on a gamma-variate model, Eq. [5], was employed to estimate voxel-specific local-AIFs and tracer kinetic CTUM parameters. Simulation studies show that the accuracy and precision of the estimated kinetic parameters were severely compromised using this uL-AIF. Even for the simulated, noiseless data, the unconstrained L-AIF approach still produces large relative errors (see Supplementary Figure S2). This is because: (i) even though no noise was added, the simulated data are inevitably truncated (i.e., only 120 abscissa values are sampled, up to 250 seconds); (ii) the simulated signal is sampled every 2.1 seconds, rather than as an ideal continuous curve. Given a total of twelve free parameters in the uL-AIF approach, it is not surprising that the tissue CA concentration *vs.* time curve is insufficiently informative to support the simultaneous estimation of all the parameters defining both the fully parameterized, voxel-specific uL-AIFs and the tracer kinetic model. This effect is visually demonstrated by the PDFs for the CTUM's three free parameters in Figures 2d - f (red). When the uL-AIF is employed, the PDFs for the CTUM's three free parameters are low and wide, indicating poor parameter estimation, despite the small systematic deviations in the residual, i.e., good modeling in terms of Chi-square (Figure 2b). Here, we highlight that the Bayesian-based data analysis approach described herein affords a posterior PDF, rather than a single parameter value,

for each of the estimated parameters and thus, importantly, provides uncertainties (i.e., the width and shape of the PDFs) for all results.

Upon constraining the voxel-specific local-DCE-AIF model with parameters extracted from the R-AIF, the accuracy and precision of PS , v_p , and F_p are all significantly improved compared to the use of the uL-AIF model (see Supplementary Figure S2). Applying this cL-AIF approach to the cervical cancer DCE-MRI data, Figures 2a - c show improved modeling (smaller residuals) compared to the direct use of the R-AIF. Also, the kinetic parameters (PS , v_p , and F_p) were all well resolved (Figures 2d - f). Consistent with previous DCE-MRI [10] and DSC-MRI [12, 13] reports, blood plasma flow was underestimated when the R-AIF was employed (see Supplementary Table S3). Note that the values of v_p estimated by both approaches are high, which is likely due to the physiological assumptions/constraints inherent in the CTUM (e.g., negligible CA backflux from the extravascular extracellular space to the vascular space, see Soubbron *et al.* [4] for details). Indeed, all of the commonly used DCE models, including the extended Tofts model, make different underlying assumptions/simplifications that allow, in principle, an exceedingly complex tissue response to be approximated by just a few summary parameters. Whenever a simplified model is employed for the purpose of stable parametric estimates, biases in the estimated parameter values will inevitably be generated by the simplifications/constraints. One key feature of essentially all modeling methods is that more complex models are almost always able to provide better representations of the data, as determined by Chi-square. However, the tradeoff is that more complex models require higher data quality to support stable parameter estimation. To further test whether the two added free parameters (Δt and s) in the cL-AIF model were well supported by the DCE-MRI data, Bayesian model selection, which takes into account both the goodness of fit and the complexity of the model, was applied to compare the cL-AIF and

R-AIF approaches. As noted earlier, the weight (or penalty) assigned to each parameter derives naturally from that parameter's contribution to the likelihood function of the modeled data (i.e., its posterior probability), which distinguishes the Bayesian approach from other constrained optimization methods. The cL-AIF approach was preferred relative to the R-AIF approach (bar graph in Figure 4) for the clinical cervical cancer DCE-MRI data reported herein.

From an experimental perspective, we note that the measured R-AIF may contain errors/artifacts that affect the amplitude, including inflow and partial volume. Further, limited water exchange may also affect the amplitude estimated by the cL-AIF method. Estimates of the amplitude scaling factor will be influenced by such model imperfections. Thus, care should be taken in interpretation (physiological meaning) of the amplitude of the scaling factor. Like other tracer kinetic model parameter estimation methods, the main limitation of our study is the validation of the derived physiological parameters in terms of their biophysical “trueness”. For this study, in which inferred cL-AIFs were employed, validation against non-MR and non-AIF based methods would be ideal. However, this validation is challenging, due to the lack of such gold-standard methods with human subjects. Evaluating the clinical utility of the estimated tracer kinetic parameters for diagnosis and monitoring/predicting therapeutic response, which are ongoing, may provide a reasonable alternative.

In conclusion, we have shown through *in silico* simulations that the cL-AIF method provides accurate and precise CTUM parameter estimates under contrast-to-noise conditions representative of clinical DCE-MRI. Further, when compared against a single, global R-AIF, Bayesian model selection chose the voxel-specific cL-AIF, in concert with the CTUM, as the preferred clinical cervical cancer DCE-MRI data model. Additionally, as expected with heterogeneous cervical

cancer tissue, the estimated, voxel-specific cL-AIFs show local variations in CA bolus amplitude and arrival time.

We note that the cL-AIF approach is not limited to cervical cancer data, nor to the CTUM. Indeed, the cL-AIF approach should be widely applicable to other R-AIFs and tracer kinetic models. We also highlight that Bayesian-based data analysis affords uncertainties for each estimated parameter, *via* PDFs, and voxel-wise comparison across methods/models, *via* model selection. (An enabling software suite is available at <http://bayesiananalysis.wustl.edu/index.html>.) Further work is required to validate the biophysical trueness of the tracer kinetic parameters estimated with the cL-AIF approach, likely through the use of preclinical rodent models, and to evaluate whether the parameters so obtained provide better diagnosis of pathology and treatment response.

3.5 Acknowledgements

This project was supported by funding from the Alvin J. Siteman Comprehensive Cancer Center (P30 CA091842).

3.6 References

1. Tofts PS, Brix G, Buckley DL, et al (1999) Estimating kinetic parameters from dynamic contrast-enhanced t1-weighted MRI of a diffusable tracer: Standardized quantities and symbols. *J Magn Reson Imaging* 10:223–232
2. Naish JH, Kershaw LE, Buckley DL, et al (2009) Modeling of contrast agent kinetics in the lung using T1-weighted dynamic contrast-enhanced MRI. *Magn Reson Med* 61:1507–1514
3. Leuthardt EC, Duan C, Kim MJ, et al (2016) Hyperthermic Laser Ablation of Recurrent Glioblastoma Leads to Temporary Disruption of the Peritumoral Blood Brain Barrier. *PLOS ONE* 11:e0148613. doi: 10.1371/journal.pone.0148613
4. Sourbron SP, Buckley DL (2013) Classic models for dynamic contrast-enhanced MRI. *NMR Biomed* 26:1004–1027

5. Yankeelov TE, Lepage M, Chakravarthy A, et al (2007) Integration of quantitative DCE-MRI and ADC mapping to monitor treatment response in human breast cancer: initial results. *Magn Reson Imaging* 25:1–13
6. Semple SIK, Harry VN, Parkin DE, Gilbert FJ (2009) A Combined Pharmacokinetic and Radiologic Assessment of Dynamic Contrast-Enhanced Magnetic Resonance Imaging Predicts Response to Chemoradiation in Locally Advanced Cervical Cancer. *Int J Radiat Oncol* 75:611–617
7. Parker GJM, Roberts C, Macdonald A, et al (2006) Experimentally-derived functional form for a population-averaged high-temporal-resolution arterial input function for dynamic contrast-enhanced MRI. *Magn Reson Med* 56:993–1000
8. Port RE, Knopp MV, Brix G (2001) Dynamic contrast-enhanced MRI using Gd-DTPA: Interindividual variability of the arterial input function and consequences for the assessment of kinetics in tumors. *Magn Reson Med* 45:1030–1038
9. Calamante F (2005) Bolus dispersion issues related to the quantification of perfusion MRI data. *J Magn Reson Imaging* 22:718–722
10. Schmitt M, Viallon M, Thelen M, Schreiber WG (2002) Quantification of myocardial blood flow and blood flow reserve in the presence of arterial dispersion: a simulation study. *Magn Reson Med* 47:787–793
11. Murase K, Yamazaki Y, Miyazaki S (2004) Deconvolution analysis of dynamic contrast-enhanced data based on singular value decomposition optimized by generalized cross validation. *Magn Reson Med Sci MRMS Off J Jpn Soc Magn Reson Med* 3:165–175
12. Wu O, Østergaard L, Koroshetz WJ, et al (2003) Effects of tracer arrival time on flow estimates in MR perfusion-weighted imaging. *Magn Reson Med* 50:856–864
13. Calamante F, Gadian DG, Connelly A (2000) Delay and dispersion effects in dynamic susceptibility contrast MRI: simulations using singular value decomposition. *Magn Reson Med Off J Soc Magn Reson Med Soc Magn Reson Med* 44:466–473
14. Rose SE, Janke AL, Griffin M, et al (2004) Improved Prediction of Final Infarct Volume Using Bolus Delay–Corrected Perfusion-Weighted MRI Implications for the Ischemic Penumbra. *Stroke* 35:2466–2471
15. Korporeal JG, van den Berg CA, Jeukens CR, et al (2010) Dynamic Contrast-enhanced CT for Prostate Cancer: Relationship between Image Noise, Voxel Size, and Repeatability 1. *Radiology* 256:976–984
16. van Osch MJP, van der Grond J, Bakker CJG (2005) Partial volume effects on arterial input functions: shape and amplitude distortions and their correction. *J Magn Reson Imaging JMRI* 22:704–709
17. Fluckiger JU, Schabel MC, DiBella EV (2009) Model-based blind estimation of kinetic parameters in dynamic contrast enhanced (DCE)-MRI. *Magn Reson Med* 62:1477–1486

18. Fluckiger JU, Schabel MC, DiBella EVR (2010) Toward local arterial input functions in dynamic contrast-enhanced MRI. *J Magn Reson Imaging* 32:924–934
19. Lee JJ, Bretthorst GL, Derdeyn CP, et al (2010) Dynamic susceptibility contrast MRI with localized arterial input functions. *Magn Reson Med* 63:1305–1314
20. Kallehauge JF, Tanderup K, Duan C, et al (2014) Tracer kinetic model selection for dynamic contrast-enhanced magnetic resonance imaging of locally advanced cervical cancer. *Acta Oncol Stockh Swed* 53:1064–1072
21. Sharma P, Socolow J, Patel S, et al (2006) Effect of Gd-DTPA-BMA on blood and myocardial T1 at 1.5T and 3T in humans. *J Magn Reson Imaging* 23:323–330
22. Duan C, Kallehauge JF, Bretthorst GL, et al (2016) Are complex DCE-MRI models supported by clinical data? *Magn Reson Med* n/a-n/a. doi: 10.1002/mrm.26189
23. Jaynes ET (2003) *Probability Theory: The Logic of Science*. Cambridge University Press
24. Calamante F, Yim PJ, Cebal JR (2003) Estimation of bolus dispersion effects in perfusion MRI using image-based computational fluid dynamics. *NeuroImage* 19:341–35

Chapter 4 Anti-VEGF Treatment of Frank Radiation-Induced Necrosis in Brain¹

4.1 Introduction

Radiation-induced necrosis (RN), with clinical symptoms mimicking those of tumor recurrence, is a late time-to-onset, devastating complication following radiotherapy to the central nervous system (1–3). Traditionally, RN has been treated with corticosteroid (4) to control edema and lessen inflammatory responses. However, the long-term use of corticosteroid is associated with chronic side effects, including hyperglycemia and immunosuppression. Anticoagulants agents (e.g., heparin and warfarin) (5) and hyperbaric oxygen therapy (6) have also been used in an attempt to heal microvasculature impairments and improve regional cerebral blood supply, but results have been inconsistent and disappointing (7). Recently, RN in the brain has been treated clinically using bevacizumab (Avastin®, Genentech, San Francisco, CA), an anti-vascular endothelial growth factor (VEGF) antibody hypothesized to restore blood brain barrier (BBB) function and, thereby, to repair vascular leakage (7–9).

While bevacizumab improves neurological symptoms and reduces the volume of RN-associated vascular leakage and resultant edema detected radiographically, the treatment brings with it potentially serious complications (10–12). For instance, bevacizumab treatment increases the risk of hemorrhage and retards wound healing by impairing neovascularization, which are critical concerns for neurosurgeons (12, 13). Also, Levin et al (14) reported clinically significant toxicity, including deep-vein thrombosis, and superior-sagittal-sinus thrombosis, in 6 of 11 bevacizumab-

¹ All contents in this chapter have been published in Duan, C., Perez-Torres, C.J., Yuan, L., Engelbach J.A., Beeman S.C., Tsien, C.I., Rich K.M., Schmidt R.E., Ackerman J.J.H., Garbow, J.R. et al. *J Neurooncol* (2017). doi: 10.1007/s11060-017-2410-3.

treated patients. Deterioration/rebound phenomena after an initial positive response with/without continued therapy have also been documented (15–17). A comprehensive study of the treatment effect, validated with gold-standard histology, is warranted. Preclinical models present a unique opportunity to study the effects of anti-VEGF antibody treatment on pure RN, independent of the potentially obfuscating complications of other pathologies, including recurrent tumors.

We have previously investigated the mitigative effect of anti-VEGF antibody on RN (18) and the specificity of this effect (19), in which the irradiated mice were treated starting from the *initial* appearance of RN on anatomic MR (approximately 4 weeks post irradiation). Motivated by ongoing clinical trials using bevacizumab to treat *frank* RN, in the present study we evaluate the anti-VEGF antibody treatment with a preclinical protocol mimicking the more clinically relevant situation. Specifically, anti-VEGF antibody treatment is not administered until a moderate-size region of focal RN developed at the irradiation site. Both anatomic and diffusion-weighted MRI were employed to monitor changes in the lesions as functions of both treatment and time post irradiation. We also evaluated the treatment responses using standard haematoxylin and eosin (H&E) and immunohistochemical (IHC) stains, an evaluation that is, generally, impractical in humans due to the lack of appropriate tissue samples.

4.2 Material and methods

4.2.1 Animal Model

All experiments were approved by the Washington University Animal Studies Committee and were performed on six-to-eight week old female BALB/c mice (Harlan/Envigo, Indianapolis, IN, USA). A single-fraction, 50-Gy dose of radiation (50% isodose) from the Leksell Gamma Knife[®] Perfexion[™] (Elekta, Stockholm, Sweden) was focused on the cortex of the left hemisphere (n =

24). Figure 4.1 illustrates the irradiation scheme. As has been shown previously (18–20), this large, single-fraction dose of radiation reproducibly and robustly generates, in all irradiated mice, radiation necrosis whose histology recapitulates all of the features of clinical RN. At this dose, moderate focal RN can be observed at approximately 8 weeks post irradiation (PIR) on both anatomic MRI and histology (20). B20-4.1.1, a murine antibody that recognizes VEGF, and GP120:9239, a murine antibody of the same isotype that targets the HIV capsid protein, were obtained from Genentech (South San Francisco, CA, USA). At week 8 PIR, mice were randomly divided into two groups: (i) an anti-VEGF group, treated with B20-4.1.1 and (ii) an isotype-control group, treated with GP120:9239. Each antibody was administered intraperitoneally at 10 mg/kg twice weekly until week 12 PIR. To minimize the acute effect of blocking VEGF activity on permeability and therefore contrast-agent extravasation, all MRI scans were performed two days following a treatment.

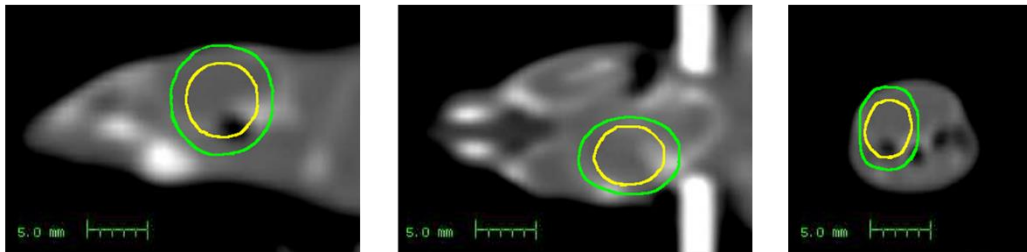


Figure 4.1: Illustration of the Gamma Knife irradiation scheme Yellow indicates isodose, while green indicates 25% isodose.

4.2.2 Magnetic Resonance Imaging

Images were acquired with a 4.7-T small-animal Agilent/Varian (Santa, Clara, CA) DirectDrive™ scanner using an actively decoupled transmit (volume, 9-cm inner diameter) and receive (surface, 1.5-cm outer diameter) coil pair. Mice were placed on a warm water pad and anesthetized with

isoflurane/O₂ (1% isoflurane) throughout the experiment. Before loading into the magnet, mice were given an intraperitoneal injection of 0.25 mL MultiHance (gadobenate dimeglumine; Bracco Diagnostics, Princeton, NJ) contrast agent, diluted 1:5 in sterile saline. Post-contrast T1-weighted (T1W, TR/TE = 650/16 ms) and T2-weighted (T2W, TR/TE = 1500/50 ms), spin-echo transaxial images were acquired every other week from week 4 PIR to week 12 PIR. A total of 21 contiguous slices with 0.5 mm thickness and $15 \times 15 \text{ mm}^2$ field of view (128×128 matrix) were collected. Diffusion-weighted images (DWI) were acquired at week 8 PIR (pre-treatment) and week 12 PIR (post-treatment) employing a diffusion weighted spin-echo sequence. Three separate diffusion datasets with the diffusion-encoding gradient applied along three orthogonal directions ($b = 1000 \text{ s/mm}^2$), and a reference dataset, without diffusion gradient ($b = 0$), were acquired for each animal with the same field of view as the post-contrast T1W and T2W images.

4.2.3 Data Analysis

RN volumes were derived from both post-contrast T1W and T2W images, as previously described (21), using custom-written Matlab software (The Mathworks, Natick, MA). Briefly, each mouse brain was divided along the midline into left (irradiated) and right (non-irradiated) hemispheres. The intensity of each pixel in the left hemisphere was normalized by the average intensity of 25 pixels (5×5 square) surrounding its mirror-image pixel in the right hemisphere. The lesion volumes were then determined *via* a threshold segmentation algorithm, in which areas of the left hemisphere brighter than the 95th percentile of the right hemisphere (i.e., an intensity threshold of roughly 1.4x that of the mean normalized pixel intensity) were defined as lesions. In addition, areas darker than the 95th percentile of the right hemisphere (i.e., a threshold of roughly 0.6) were also classified as lesions to account for hypo-intense regions caused by hemorrhage. For DWI experiments, apparent diffusion coefficient (ADC) maps were calculated as the average of the

diffusion coefficients calculated from the three separate diffusion datasets and the reference dataset. For both groups, RN lesion ROIs were defined on the post-contrast T1W images at week 8 PIR and overlaid onto the ADC maps. Each week-12 PIR image was co-registered (affine transformation to allow for possible scaling changes caused by brain swelling) to its corresponding week-8 PIR image. The same ROI drawn in week 8 was then overlaid onto the corresponding week-12 image. The median value for the ADC across the ROI was calculated for comparison between pre- and post-treatment datasets. Statistical analyses for both RN volumes and median ADCs were performed using a paired-sample, two-sided *t*-test.

4.2.4 Histology and IHC

All mice were sacrificed immediately after the last imaging time point (week 12 PIR) and intracardially perfused with 1% phosphate-buffered saline (PBS, PH = 7.4) and 10% formalin. Mice heads were dissected and immersed in formalin for 24 hours. Brains were removed from the skulls and a 3-mm thick transaxial block, centered at the irradiation site (~3 mm behind the bregma), was obtained for each brain. The blocks were then processed through graded alcohols and embedded in paraffin. All paraffin- fixed blocks were sectioned from their centers at a thickness of five microns. Tissue sections were stained with haematoxylin and eosin (H&E) according to standard protocols. Immunohistochemical staining (IHC) for both VEGF and HIF-1 α was performed following the manufacturers' protocols. Antigen retrieval was performed with citrate buffer (pH = 6.8) at 70°C overnight following one-hour non-specific blocking. Rabbit anti-VEGF (orb11553, Biorbyt, Cambridge, UK) at 1:500 and Rabbit anti-HIF-1 α (NB100-479, Novus Biotechnology, Littleton, CO, USA) at 1:300 were used as primary antibodies at 4°C overnight, and diaminobenzidine (DAB) staining was performed using the Histostain Plus Broad System kit (Invitrogen, Frederick, MD, USA). All sections were incubated with a broad-spectrum secondary

antibody for one hour and with horseradish peroxidase streptavidin (HRP-streptavidin) for 30 minutes. Staining was visualized with a DAB precipitation reaction. Histological slides were examined with the Hamamatsu NanoZoomer whole-slide imaging system (Hamamatsu, Hamamatsu City, Japan).

4.3 Results

RN volume is decreased after anti-VEGF antibody treatment

Both the anti-VEGF antibody-treated and isotype-control antibody-treated mice were imaged biweekly from weeks 4 to 12 PIR. Figure 4.2 shows representative post-contrast T1W and T2W images for both groups at week 8 (pre-treatment) and week 12 (post-treatment) PIR. RN lesions appear bright in these images. Note that anti-VEGF treatment reduced swelling (smaller brain sizes), while the brains continued to swell for the isotype-control group. Post-contrast, T1W-derived lesion volumes decreased after anti-VEGF treatment from 51.3 ± 19.0 to 24.6 ± 14.8 mm³ ($P < 0.001$), while the lesion volumes of the isotype-control antibody treated group increased from 55.4 ± 27.0 to 101.9 ± 42.9 mm³ ($P < 0.001$). Similarly, T2W-derived lesion volumes decreased after anti-VEGF treatment from 45.9 ± 15.5 to 21.7 ± 13.5 mm³ ($P < 0.001$), while the lesion volumes of the isotype-control group increased from 40.5 ± 15.8 to 84.9 ± 28.4 mm³ ($P < 0.001$). Note that T2W-derived lesion volumes are slightly smaller than post-contrast T1W-derived volumes, consistent with results reported previously (19).

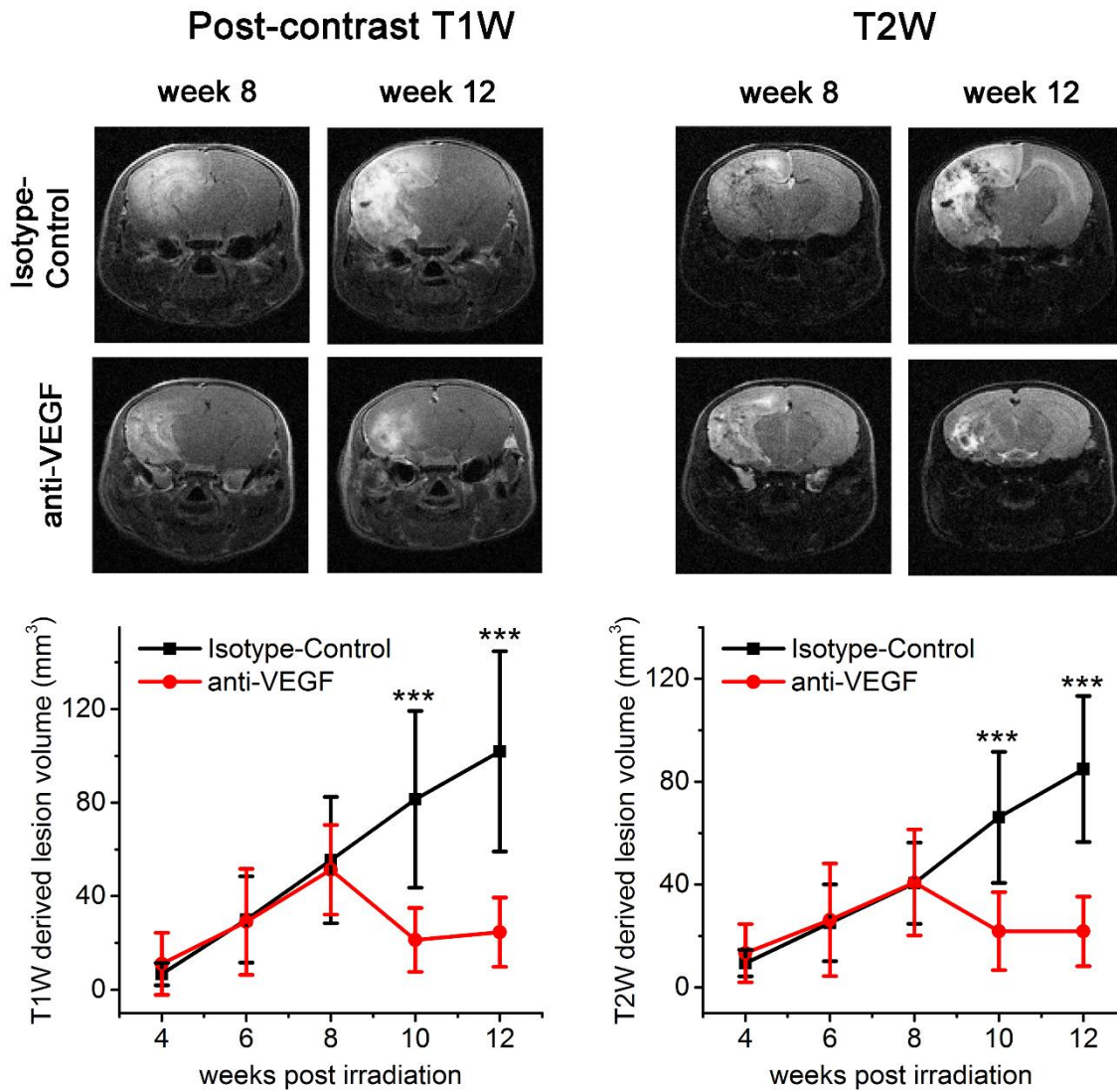
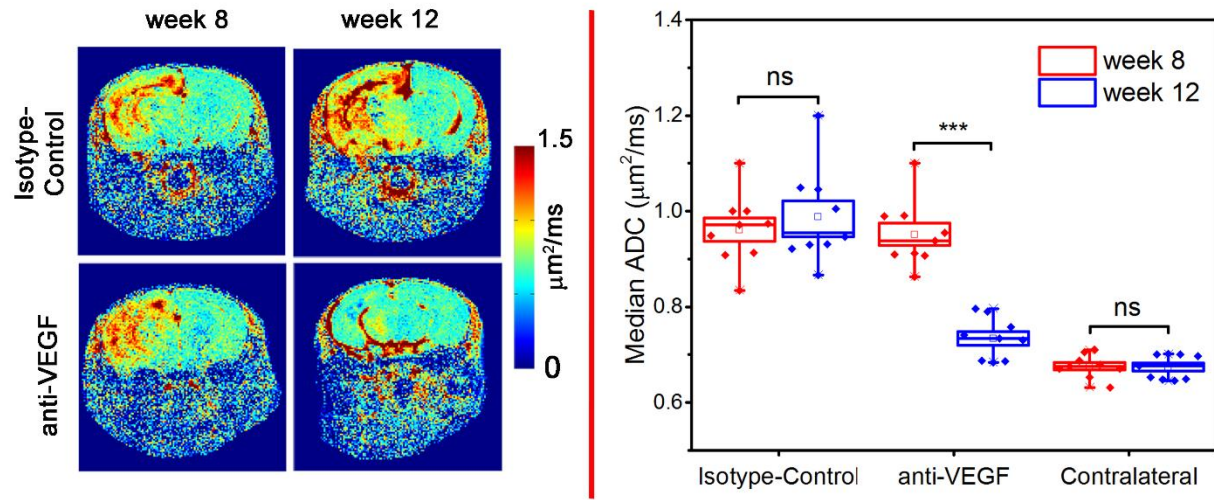


Figure 4.2: Anti-VEGF treatment response detected by anatomic MRI. The top panels show images at week 8 PIR (pre-treatment) and week 12 PIR (post-treatment) for one representative mouse in both isotype-control and anti-VEGF groups. The bottom panels are plots of MR-derived lesion volumes (mean \pm SD, $n = 12$) vs. time after irradiation for both groups (black, isotype-control group; gray, anti-VEGF group). “***” indicate $P < 0.001$ as calculated by a paired-sample t -test.

ADC is reversed after the treatment

Diffusion-weighted images were collected at weeks 8 and 12 PIR. Figure 4.3 (left) shows ADC maps for representative members of both groups. Compared to the contralateral side, the RN lesion demonstrates abnormally high ADC, as described previously (21). Boxplots in the right panel of

Figure 4.3 show that median ADCs across the lesion decreased from 0.95 ± 0.07 to 0.73 ± 0.04 $\mu\text{m}^2/\text{ms}$ ($P < 0.001$) for the anti-VEGF treated mice, while the median ADCs for the isotype-control group remain unchanged. For reference, the ADC for normal brain (0.68 ± 0.02 $\mu\text{m}^2/\text{ms}$) is computed from ROIs drawn in the contralateral hemisphere. For this healthy brain-tissue reference ADC measurement, only contralateral regions of anti-VEGF-treated animals are included, to avoid possible contamination from contralateral lesions observed previously in a small number of non-treated mice at late time points (22).



*Figure 4.3: Anti-VEGF treatment response detected by diffusion-weighted MRI. The left panels display representative ADC maps. Boxplots ($n = 9$), on the right, show median ADCs across the lesions. The contralateral group represents normal brain ADCs. “***” and “ns” indicate $P < 0.001$ and no significance, respectively.*

RN is not completely resolved histologically after treatment

To validate the treatment responses observed by MRI, standard H&E staining of brain tissue was performed for each mouse. Consistent with the clinical scenario, H&E staining of lesions in the isotype-control group display all of the classic RN-related pathologies, including telangiectasia, hyalinization, fibrinoid vascular necrosis, hemorrhage, and tissue loss (Figure 4.4, **left panel**).

These histologic features, though reduced in extent, are also observed in the brains of the anti-VEGF antibody treated mice (Figure 4.4, **middle panel**). In addition, large areas of focal mineralization (dystrophic calcification) were observed in roughly half of the anti-VEGF treated mice (Figure 4.4, **right panel**), while none of the isotype-control antibody treated brains showed any mineral deposits.

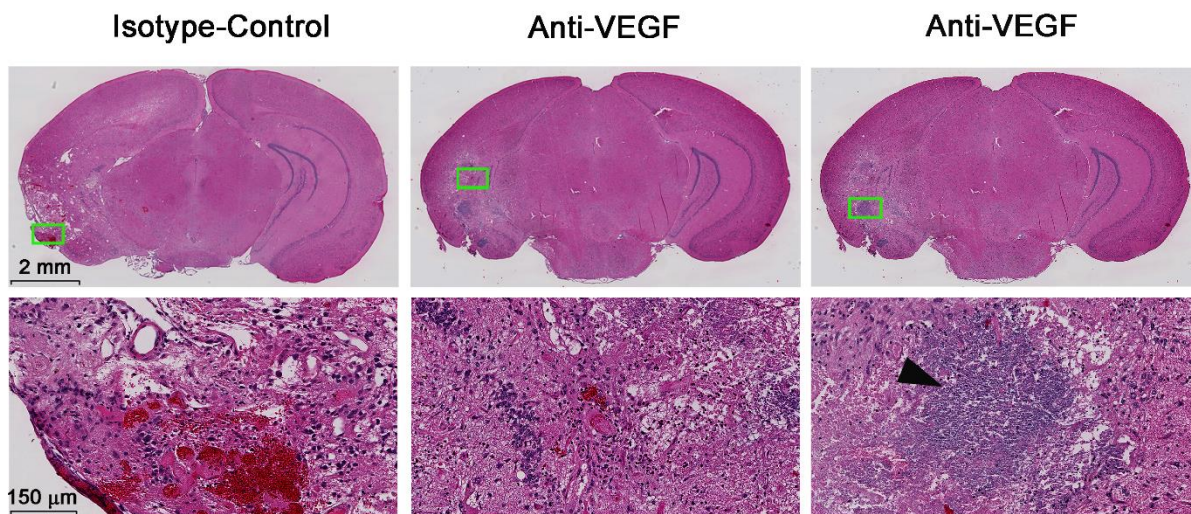


Figure 4.4: Anti-VEGF treatment as shown by H&E. Representative 2x (top) and 20x (bottom) H&E-stained slides for one isotype-control antibody treated mouse (left) and one anti-VEGF antibody treated mouse, with two different magnified areas (middle and right, respectively) at week 12 PIR. Both groups show histologic features that are characteristic of radiation necrosis, including hemorrhage, telangiectasia, loss of tissue, and neuronal necrosis. Note the large area of focal calcification (black arrowhead) in the bottom right panel.

VEGF and HIF-1 α remain upregulated after treatment

Immunohistochemistry was performed to evaluate the expression levels of VEGF and HIF-1 α , a well-known transactivator of VEGF, following anti-VEGF antibody treatment, for all mice in both groups. As a negative control, the same IHC staining protocols were also performed on non-irradiated, age-matched female mice (Figure 4.5, **left panel**). As expected, for the necrotic tissue, Figure 4.5(**middle panel**) shows that both VEGF and HIF-1 α were upregulated for the isotype-

control group, especially along the walls of the dilated blood vessels. However, despite the anti-VEGF antibody treatment and less RN-associated pathologies shown in Figure 4.4, both VEGF and HIF-1 α remained upregulated for the anti-VEGF group (Figure 4.5, **right panel**).

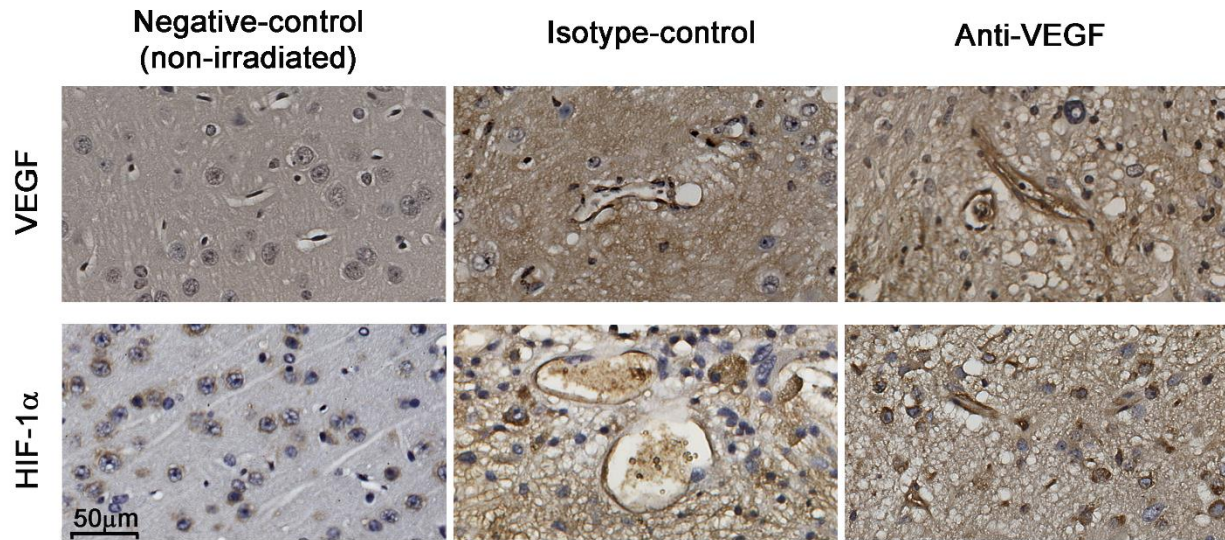


Figure 4.5: Anti-VEGF treatment response as shown by immunohistochemistry. Representative 60x VEGF (top) and HIF-1 α (bottom) staining for non-irradiated (left), isotype-control treated (middle) and anti-VEGF treated (right) mice. Brown indicates positive staining for both VEGF and HIF-1 α . Note, in particular, the dark brown staining along the dilated vessel walls.

4.4 Discussion

Cerebral radiation necrosis can be a serious consequence following radiotherapy. Traditional treatments of RN, including corticosteroids and hyperbaric oxygen, are associated with significant toxicity and limited efficacy (23). Recently, multiple groups have investigated the treatment effect of anti-VEGF antibody (i.e., bevacizumab), which blocks VEGF from reaching its capillary target and is, thus, hypothesized to reduce vascular leakage and associated brain edema, on radiographic volumes of RN clinically (7–10). The work presented herein is distinct from prior clinical studies in that the Gamma Knife mouse RN model is a single hemisphere radiation injury model, which

allows (i) direct comparisons with the non-irradiated hemisphere and (ii) histological validations that are impractical for clinical cases. The model is also independent of potential complications arising from other pathologies, including recurrent tumor.

Consistent with prior clinical investigations (7–10), anti-VEGF treated mice show remarkable decreases of RN lesion volume, detected radiographically on both post-contrast T1W and T2W images (**Fig. 1**). This finding is correlated with the smaller lesion volume, and less vasogenic edema, on H&E-stained brain tissue in treated group vs. untreated group. The swelling of the irradiated brains is also reduced by the treatment. In addition to anatomic images, diffusion MRI, whose metrics reflect the barriers and restrictions to the incoherent displacement of water molecules, was also investigated. We showed that the abnormally high ADC associated with RN was reduced to more normal levels (**Fig. 2**), an effect that is likely due to decreased vasogenic edema and brain swelling.

Building upon the results of our previous work, in which anti-VEGF treatment was initiated at the *initial* radiologic appearance of RN, the current study addresses the more clinically relevant problem in which treatment is not started until after the development of regions of *frank* RN. While in our earlier study the treated mice displayed almost no visible tissue damage by histology (H&E), typical RN histologic pathologies and large areas of focal mineral deposits are present after the anti-VEGF treatment in the current study. Jeyaretna et al (15) reported a worsening clinical scenario after bevacizumab treatment of histologic diagnosis-confirmed RN. In a follow-up, image-guided surgical biopsy, large areas of focal dystrophic calcification were observed in the lesion. It was hypothesized the prolonged anti-VEGF treatment resulted in overpruning of at-risk blood vessels, leading to vascular deficiency, which eventually exacerbated the lesion. The

connection between vascular deficiency and the observed dystrophic calcification is unclear and requires further study.

The pathophysiology of RN remains incompletely understood. The current consensus views RN as a continuous, complex process from endothelial-cell dysfunction to tissue hypoxia and necrosis, with concomitant upregulation of both HIF-1 α and VEGF (24, 25). As expected, we found that both VEGF and the HIF-1 α are upregulated for the isotype-control group, consistent with limited clinical biopsy results. Both VEGF and HIF-1 α remain upregulated in the treatment group, which may contribute to the risk of recurrence of RN lesions. This finding is consistent with the mechanism of action of the anti-VEGF antibody, which binds and, thus, blocks the function of VEGF and its bioactive fragments, but does not reduce/eliminate VEGF expression. In this regard, directly targeting of its upstream transactivator, HIF-1 α , may represent a feasible approach for reducing the expression of VEGF. On the other hand, VEGF is a homodimeric glycoprotein that acts *via* endothelial-specific receptor tyrosine kinases (e.g., VEGFR2). Thus, blocking these receptors may also help to reduce RN recurrence despite the continued upregulation of VEGF itself.

The observed reduction in radiographically detected lesion volume in mice is consistent with the improvement in clinical symptoms seen in RN patients following treatment with bevacizumab (14). However, neither post-contrast T1W nor T2W imaging contrasts provide direct readouts of RN pathologies. Post-contrast T1W is sensitive to vascular permeability, while T2W is sensitive to the brain edema resulted from the vascular leakage. It is not surprising that the anti-VEGF antibody, which mediates the BBB dysfunction, reduces the lesion volumes derived from these images. However, further tissue changes/damage within the necrotic area, including neuronal

necrosis and vascular necrosis, may be permanent and irreversible. Such pathology could be “invisible” on these images after anti-VEGF treatment.

One major limitation/side effect of anti-VEGF antibody treatment is that it impairs neovascularization and retards wound healing. Consequently, the timing of surgery in neurosurgical patients treated with anti-VEGF therapy must be carefully considered (12). Additionally, although this study demonstrated that anti-VEGF antibody treatment can reduce radiographically observed RN lesion volume, it did not address important questions about optimal dosing schemes and treatment periods. The use of a lower antibody dose and shorter treatment periods could potentially minimize side effects and improve patient care.

In summary, we found anti-VEGF antibody decreased RN lesion volumes on post-contrast T1W and T2W in a Gamma Knife mouse RN model. In addition, the abnormally high RN ADCs were reduced to values typical of normal brain. However, the lesions were not completely resolved histologically. The subsequent calcification and the continued upregulation of VEGF and HIF-1 α merit further clinical and pre-clinical investigation. More effective treatments, possibly aimed at targets either upstream (e.g., HIF-1 α) or downstream (e.g., VEGFR2) of VEGF, and monitoring of the neurological behavior of irradiated animals, pre- and post-treatment, will be the subject of future studies.

4.5 Acknowledgements

This project was supported by NIH grant R01 CA155365 (J.R.G), funding from the Alvin J. Siteman Cancer Center (P30 CA091842), the Barnes-Jewish Hospital Foundation Cancer Frontier Fund, and Elekta Instruments AB (Stockholm, Sweden). We acknowledge Genentech for donation

of the antibodies B20-4.1.1 and GP120:9239 and thank Mr. Jeremy Cates for his help with the irradiation of the mice.

4.6 References

1. Giglio P, Gilbert MR (2003) Cerebral radiation necrosis. *The neurologist* 9:180–188.
2. Kumar AJ, Leeds NE, Fuller GN et al. (2000) Malignant Gliomas: MR Imaging Spectrum of Radiation Therapy- and Chemotherapy-induced Necrosis of the Brain after Treatment 1. *Radiology* 217:377–84.
3. Rahmathulla G, Marko NF, Weil RJ (2013) Cerebral radiation necrosis: a review of the pathobiology, diagnosis and management considerations. *J Clin Neurosci* 20:485–502.
4. Shaw PJ, Bates D (1984) Conservative treatment of delayed cerebral radiation necrosis. *J Neurol Neurosurg Psychiatry* 47:1338–1341.
5. Glantz MJ, Burger PC, Friedman AH, et al (1994) Treatment of radiation-induced nervous system injury with heparin and warfarin. *Neurology* 44:2020–2020.
6. Bui Q-C, Lieber M, Withers HR, et al (2004) The efficacy of hyperbaric oxygen therapy in the treatment of radiation-induced late side effects. *Int J Radiat Oncol* 60:871–878. doi: 10.1016/j.ijrobp.2004.04.019
7. Gonzalez J, Kumar AJ, Conrad CA, Levin VA (2007) Effect of bevacizumab on radiation necrosis of the brain. *Int J Radiat Oncol Biol Phys* 67:323–326. doi: 10.1016/j.ijrobp.2006.10.010
8. Torcuator R, Zuniga R, Mohan YS et al. (2009) Initial experience with bevacizumab treatment for biopsy confirmed cerebral radiation necrosis. *J Neurooncol* 94:63–8.
9. Bölke E, Nawatny J, Hoffmann TK et al. (2011) Bevacizumab as a treatment option for radiation-induced cerebral necrosis. *Strahlenther Onkol* 187:135–9.
10. Lubelski D, Abdullah KG, Weil RJ, Marko NF (2013) Bevacizumab for radiation necrosis following treatment of high grade glioma: a systematic review of the literature. *J Neurooncol* 115:317–322. doi: 10.1007/s11060-013-1233-0
11. Scappaticci FA, Fehrenbacher L, Cartwright T et al. (2005) Surgical wound healing complications in metastatic colorectal cancer patients treated with bevacizumab. *J Surg Oncol* 91:173–80. doi:10.1002/jso.20301.
12. Abrams DA, Hanson JA, Brown JM, et al (2015) Timing of surgery and bevacizumab therapy in neurosurgical patients with recurrent high grade glioma. *J Clin Neurosci* 22:35–39.

13. Clark AJ, Butowski NA, Chang SM et al. (2011) Impact of bevacizumab chemotherapy on craniotomy wound healing: Clinical article. *J Neurosurg* 114:1609–16.
14. Levin VA, Bidaut L, Hou P et al. (2011) Randomized Double-Blind Placebo-Controlled Trial of Bevacizumab Therapy for Radiation Necrosis of the Central Nervous System. *Int J Radiat Oncol* 79:1487–95. doi:10.1016/j.ijrobp.2009.12.061.
15. Jeyaretna DS, Curry WT, Batchelor TT, et al (2011) Exacerbation of Cerebral Radiation Necrosis by Bevacizumab. *J Clin Oncol* 29:e159–e162. doi: 10.1200/JCO.2010.31.4815
16. Furuse M, Kawabata S, Kuroiwa T, Miyatake S-I (2010) Repeated treatments with bevacizumab for recurrent radiation necrosis in patients with malignant brain tumors: a report of 2 cases. *J Neurooncol* 102:471–475. doi: 10.1007/s11060-010-0333-3
17. Wang Y, Pan L, Sheng X et al (2012) Reversal of cerebral radiation necrosis with bevacizumab treatment in 17 Chinese patients. *Eur J Med Res* 2012;17:25. doi:10.1186/2047-783X-17-25.
18. Jiang X, Engelbach JA, Yuan L, et al (2014) Anti-VEGF Antibodies Mitigate the Development of Radiation Necrosis in Mouse Brain. *Clin Cancer Res* 20:2695–2702. doi: 10.1158/1078-0432.CCR-13-1941
19. Perez-Torres CJ, Yuan L, Schmidt RE, et al (2015) Specificity of vascular endothelial growth factor treatment for radiation necrosis. *Radiother Oncol* 117:382–385. doi: 10.1016/j.radonc.2015.09.004
20. Jiang X, Yuan L, Engelbach JA, et al (2015) A Gamma-Knife-Enabled Mouse Model of Cerebral Single-Hemisphere Delayed Radiation Necrosis. *PLOS ONE* 10:e0139596. doi: 10.1371/journal.pone.0139596
21. Perez-Torres CJ, Engelbach JA, Cates J, et al (2014) Toward Distinguishing Recurrent Tumor From Radiation Necrosis: DWI and MTC in a Gamma Knife–Irradiated Mouse Glioma Model. *Int J Radiat Oncol* 90:446–453. doi: 10.1016/j.ijrobp.2014.06.015
22. Perez-Torres CJ, Yuan L, Schmidt RE, et al (2015) Perilesional edema in radiation necrosis reflects axonal degeneration. *Radiat Oncol Lond Engl* 10:33. doi: 10.1186/s13014-015-0335-6
23. Miyatake S-I, Nonoguchi N, Furuse M, et al (2014) Pathophysiology, Diagnosis, and Treatment of Radiation Necrosis in the Brain. *Neurol Med Chir (Tokyo)*. doi: 10.2176/nmc.ra.2014-0188
24. Wong CS, Van der Kogel AJ (2004) Mechanisms of radiation injury to the central nervous system: implications for neuroprotection. *Mol Interv* 4:273–284. doi: 10.1124/mi.4.5.7
25. Yoritsune E, Furuse M, Kuwabara H, et al (2014) Inflammation as well as angiogenesis may participate in the pathophysiology of brain radiation necrosis. *J Radiat Res (Tokyo)* 55:803–811. doi: 10.1093/jrr/rru017

.

Chapter 5 Irradiated Brain Parenchyma Promotes Enhanced Tumor Growth and Invasion in a Mouse Model of Recurrent Glioblastoma¹

5.1 Introduction

Glioblastoma (GBM) is a highly aggressive and incurable malignant neoplasm of the brain. Together with surgical resection and chemotherapy, radiation therapy (RT) is a central component of the standard treatment for patients with newly diagnosed GBM (1–3). Advances in RT over the past decade have allowed more accurate delivery of radiation, and, thus, improved patient outcomes (4–6). Nonetheless, GBM tumors invariably recur, the vast majority within the first year (7) and within two centimeters of the RT treatment field (8,9).

Much of the attention regarding GBM recurrence has focused on glioma stem cells (GSCs), which are resistant to radiation (10,11), have increased DNA damage checkpoint and repair capacity (10), and exhibit lower rates of apoptosis (12–14). Nevertheless, radiation affects not only tumor cells, but also the tumor microenvironment (TME), and especially tumor-associated microglia and macrophages (15) that may contribute significantly to the resistance and recurrence of gliomas (16). Indeed, emerging evidence indicates that radiotherapy effects extend beyond cancer cell death (17). Irradiation induces vascular, stromal, and immunological changes in the TME that may enhance the migration and invasiveness of irradiated tumor cells (18). In this regard, several factors have been identified that modulate interactions between tumor and TME following RT (19–22). These studies, involving irradiation of both tumor cells and the associated tumor

¹ This chapter represents a manuscript that's in preparation.

(Chong Duan, Ruimeng Yang, Liya Yuan, John A. Engelbach, Christina I. Tsien, Keith M. Rich, Sonika Dahiya, Joseph J.H. Ackerman, and Joel R. Garbow)

microenvironment, demonstrated that the radiation modified both the phenotype of the tumor cells and their microenvironment. The increased infiltration of F98 tumor cells implanted four hours following whole-brain irradiation in Fischer rats, with concomitant upregulation of inflammatory factors IL-1 β , IL-6, and TNF- α , has been recently described (23,24).

In the present study, we investigated the effects of delayed radiation-induced changes in healthy brain parenchyma on the growth of naïve (i.e., non-irradiated) tumor cells, cells having no radiation-induced genetic or molecular changes. Tumor growth was measured by magnetic resonance imaging (MRI) and animal survival assessed by monitoring weight loss, with findings supported by histology (H&E staining). In mice in which naïve tumor cells were implanted six weeks post irradiation, we observed a remarkable increase in lesion mass, with a corresponding decrease in survival. Tumors growing in previously irradiated brain parenchyma demonstrated large regions of hemorrhage and necrosis, consistent with histologic features observed in patients with recurrent high-grade tumor. This novel model of recurrent tumor can serve as a versatile platform for a variety of fundamental and translational studies to evaluate quantitatively the factors promoting tumor growth in previously irradiated tissue and to identify and test potential new therapeutics.

5.2 Methods and Materials

Animals

All experiments were performed in accordance with the guidelines of Washington University's Institutional Animal Care and Use Committee and were approved by that committee. 7- to 8-week-old female BALB/c mice (Harlan Laboratories, Indianapolis, IN), housed five per cage in a light-

and temperature-controlled facility, were used in this study. These mice were observed daily to ensure that interventions were well tolerated.

GammaKnife irradiation Procedure

Mice were anesthetized and restrained on a custom-built platform mounted to the stereotactic frame that attaches to the treatment couch of the Leksell GammaKnife® (GK) Perfexion™ (Elekta, Stockholm, Sweden), a device used for stereotactic radiosurgery of patients with malignant brain tumors. Mice were anesthetized with a mixture of ketamine (25 mg/kg), acepromazine (5 mg/kg), and xylazine (5 mg/kg), injected intraperitoneally five minutes before the start of irradiation. Single fractions of 30 Gy or 40 Gy of radiation (50% isodose), generated using the GK's four mm collimator, were focused on the left cortex at a site ~ 3 mm posterior to bregma.

Tumor implantation

Tumor cells were implanted in mice, as described previously (25). Briefly, mice were anesthetized with isoflurane and secured in a stereotactic head holder. Murine DBT glioblastoma cells (26) were implanted (~10,000 cells suspended in 10 µL per mouse) over three minutes at a site 2-mm posterior and 3-mm to the left of bregma, 2-mm below the cortical surface.

Experimental scheme

These experiments were designed to assess tumor growth and mice survival in the setting of previously irradiated brain tissue. Three cohorts of mice (n=5 each) received a single fraction dose of 0, 30, or 40 Gy (50% isodose), respectively, of GK irradiation. At these radiation doses, no frank radiation necrosis is observed, visualized by either anatomic MR imaging or standard H&E staining, up to 20 weeks post irradiation (27). DBT tumor cells were implanted into the ipsilateral hemisphere six weeks post-irradiation.

Magnetic resonance imaging

Images were collected with a 4.7-T small animal MR scanner (Agilent/Varian, Santa Clara, CA) equipped with a DirectDriveTM console. The scanner is built around a 33-cm, clear-bore magnet (Oxford Instruments, Oxford, UK), with 21-cm inner diameter, actively shielded Agilent/Magnex gradient coils (maximum gradient, 28 G/cm; rise time, approximately 200 ms), and model A-240 gradient amplifiers (300 V, 300 A; Oy International Electric Company, Helsinki, Finland).

MRI data were collected using an actively decoupled coil pair: a 9-cm inner diameter volume coil (transmit) and a 1.5-cm outer diameter surface coil (receive). Before all imaging experiments, mice were anesthetized with isoflurane [/O₂ (2% (vol/vol)) and maintained on isoflurane/O₂ (1% (vol/vol))] throughout the experiment. Mice were restrained in a laboratory-built, three-point, Teflon head holder and were placed on a water pad with circulating warm water to maintain body temperature at approximately $37 \pm 1^{\circ}\text{C}$. Before being placed into the magnet, each mouse was injected intraperitoneally with 0.25 mL of MultiHance (gadobenate dimeglumine; Bracco Diagnostics Inc, Princeton, NJ) contrast agent, diluted 2:10 in sterile saline.

Mice were imaged every three days, starting ten days post-implantation, until they were sacrificed, or died due to disease progression. Mice were sacrificed if they lost more than 20% body weight or suffered obvious behavioral deficits (e.g., ataxia). Post-contrast T₁-weighted images were acquired with the following parameters: time-to-repetition (TR) = 650 ms, time-to-echo (TE) = 20 ms, number of transient (NT) = 4, field of view = 15 x 15 mm², matrix size = 128 x 128, slice thickness = 0.5 mm, 21 slices to cover the whole brain.

Histology (H&E staining)

Immediately after the last MRI session, all the mice were sacrificed and intracardially perfused with 1% phosphate-buffered saline (PBS, pH = 7.4) and 10% formalin. Mice heads were dissected and immersed in formalin for 24 hours. Brains were removed from the skulls and a 2-mm thick transaxial block, centered at the irradiation site (~3 mm behind the bregma), was obtained for each brain. The blocks were then processed through graded alcohols and embedded in paraffin. All paraffin-fixed blocks were sectioned from the center, at a thickness of five microns. Tissue sections were stained with hematoxylin and eosin (H&E) according to standard protocols.

Data analysis and statistics

Tumor volumes were derived using MATLAB (The Mathworks, Natick MA), in which regions of interest (ROI) for the tumor lesion were drawn manually on the post-contrast T₁-weighted images by an experienced radiologist (R.Y.). In calculating volumes, hypointense regions within the tumor were also treated as tumor lesions. MR-derived lesion volumes were calculated as the sum of the lesion voxels multiplied by the voxel volume. A repeated measures One-Way ANOVA was used to compare tumor volumes across groups. Mortality was compared among 0-, 30-, and 40- Gy GK-irradiation dose groups using Kaplan-Meier analysis of survival followed by a two-tail log-rank (Mantel-Cox) test. Graphs and statistical analyses were performed in Prism (GraphPad Software, San Diego, CA) and MATLAB.

5.3 Results

Irradiated microenvironment leads to aggressive tumor growth patterns on anatomic MRI

DBT-cell tumors were implanted into the brains of irradiated mice (30 or 40 Gy) six weeks post-irradiation. Anatomic MRI and histology (H&E staining) showed no structural changes following irradiation. DBT tumors grew markedly more rapidly, with significant contrast enhancement and

necrosis, compared to the control group (i.e., DBT-cell tumors implanted into non-irradiated “normal” brains), Figure 5.1. Tumors implanted in radio-modulated brains showed markedly enhanced tumor growth patterns. Furthermore, tumor contrast enhancement patterns were far more necrotic and infiltrative in the irradiated tumor microenvironment, whereas the control group had a different, more homogenous pattern of enhancement, with well-circumscribed tumors. The hypointense regions in the tumor centers for the irradiated groups are likely due to tumor necrosis and hemorrhage (see the histological results below).

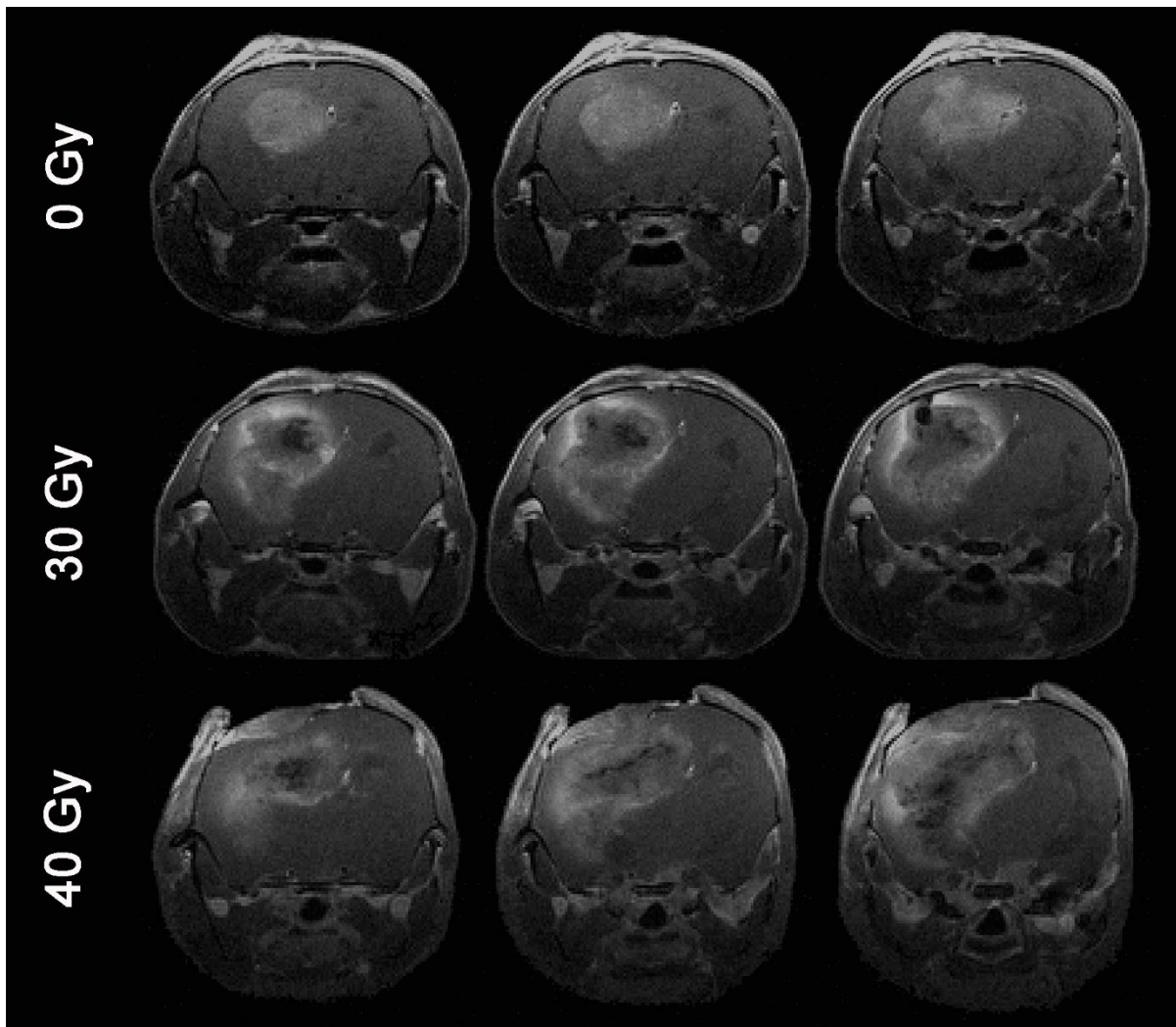


Figure 5.1: Representative, post-contrast, transaxial T1-weighted images of mice with DBT tumors post-implantation day 17. Six weeks prior to tumor-cell implantation, all mice in each

group received a single-fraction dose of 0 (no irradiation), 30 or 40 Gy of GK irradiation. Each row displays three contiguous image slices, chosen to display approximately the same anatomic region of the brain for each animal. Note the hypo-intense regions in the centers of the tumors for the irradiated groups (middle and bottom rows).

Irradiated microenvironment leads to aggressive tumor growth patterns with shortened overall survival

Figure 5.2A shows anatomic MRI tumor/lesion volumes, derived from post-contrast T₁-weighted images, post-implantation D17, for mice receiving 0-, 30-, or 40-Gy GK irradiation six weeks prior to tumor-cell implantation. Both 30- and 40-Gy irradiated groups demonstrated much larger tumor volumes compared to the Non-IR group ($P < 0.05$ for 0-Gy vs. both 30- and 40-Gy groups).

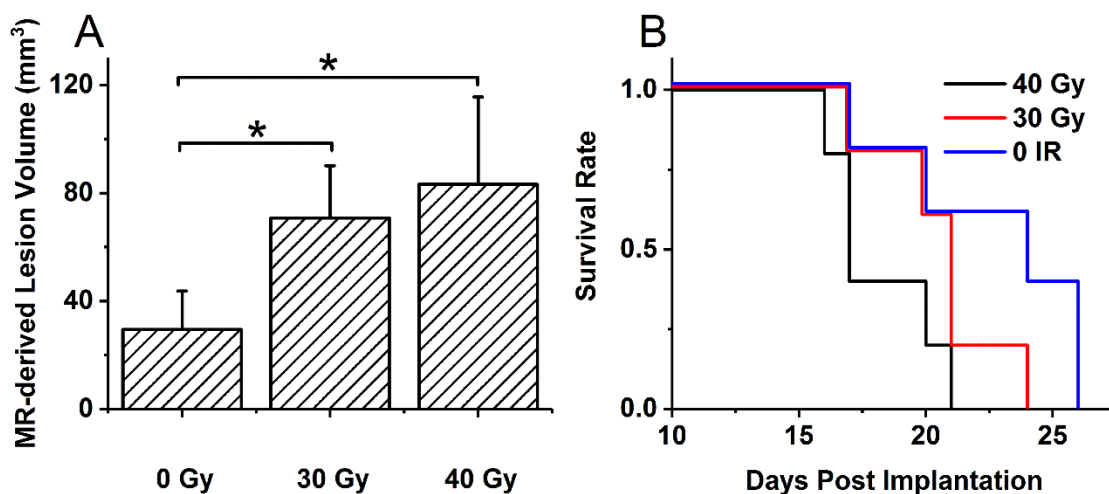


Figure 5.2: Prior Radiation Impacts Tumor Growth and Mouse Survival. **Panel A** shows lesion volumes, derived from post-contrast, T₁-weighted MR images, at post-implantation day 17, for mice irradiated with 0 (no irradiation), 30, or 40 Gy (50% isodose) six weeks prior to tumor implantation ($n = 5$ for each group). Tumor growth is significantly enhanced in previously irradiated brains, compared with non-irradiated controls. Data are shown as mean \pm standard deviation. **Panel B** shows the Kaplan-Meier survival curves for the same three groups of mice. Survival in mice irradiated with 40-Gy irradiation prior to tumor implantation is significantly shorter than that of the Non-IR group ($P < 0.05$). There is no statistically significant difference between the Non-IR and the 30-Gy groups ($P = 0.10$).

Mice with glioblastomas implanted in non-irradiated *vs.* radio-modulated brains were compared for survival. Survival data are shown in Figure 5.2B for these same three cohorts of mice. Our previous results showed that no frank RN is observed by either anatomic MR or standard H&E staining following either 30- and 40-Gy GK irradiation (27). However, DBT-cell tumor growth in the 40-Gy irradiated group was associated with a significant decrease in median survival compared with the Non-IR controls (17 *vs.* 24 days, $P<0.05$). There was no statistically significant difference observed between the 30-Gy compared to the Non-IR or 40-Gy tumor groups ($P=0.10$), likely due to the modest number of animals, $n = 5$, in each cohort. Together, these observations suggest that irradiation of the microenvironment may facilitate aggressive tumor growth with associated decreased survival in mice.

Irradiated microenvironment leads to aggressive tumor growth as noted on standard H&E staining

Mice with glioblastomas implanted in non-irradiated or radio-modulated brains were compared for changes in histology. Figure 5.3 shows standard H&E staining for three representative mice, which received 0- (Non-IR, left), 30- (middle) or 40-Gy (right) GK irradiation six weeks prior to tumor cell implantation, respectively. The Non-IR group was a control group, while the 30- and 40-Gy irradiated groups had tumors implanted in previously irradiated brain tissue absent the appearance of frank radiation necrosis. Employing low optical resolving power (2x, top row), tumors implanted in previously irradiated brain tissue demonstrated an aggressive tumor growth pattern, with large, mixed areas of hemorrhage and tumor necrosis. Under higher optical resolving power (40x, bottom row), tumors growing in a previously irradiated tumor microenvironment showed prominent histologic changes, including tumor-cell loss, tumor-cell necrosis, and hemorrhage, that were not seen in the control group.

5.4 Discussion

Despite significant treatment advances in the past decade, the overall cure rate for GBM remains extremely poor (2). While adjuvant radiotherapy significantly improves local tumor control, recurrences within a previously irradiated treatment field are highly resistant to retreatment therapies and are associated with higher risk of local invasion and poor prognosis (28). The majority of relapses following irradiation occur within 2-3 cm of the enhancing tumor volume (i.e., the target volume of RT and radio-modulated brain parenchyma) (29,30).

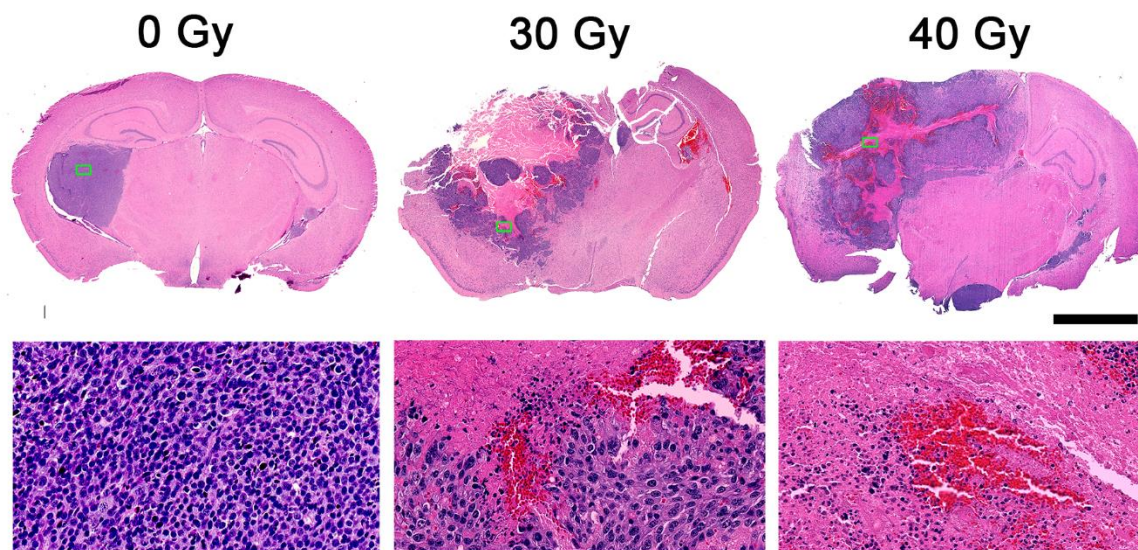


Figure 5.3: Prior irradiation of the brain with 30 Gy (middle column) or 40 Gy (right column) of GK radiation has a substantial effect on tumor growth patterns and progression histologically, compared to the control, non-irradiated brain (left column). Lesions arising tumors implanted into previously irradiated brain (middle, right columns) are significantly more vascular and necrotic than those in non-irradiated brain (right column). Scale bar: 2.3 mm (top row) and 100 μ m (bottom row).

Numerous studies focused on the response of tumor to radiation have identified radiation-induced tumoral changes as a possible driving force for the enhanced invasiveness and proliferation of recurrent tumor, contributing to resistance and, ultimately, death. It has been generally assumed

that tumor repopulation and progression after radiotherapy are due to the presence/selection of radiation-resistant tumor cells. Wide-Bode, et al. (20), demonstrated that partial brain radiotherapy may promote migration of large numbers of tumor satellites in the brain and increased invasiveness of glioma cells *via* enhanced $\alpha_v\beta_3$ integrin expression, and an altered profile of matrix metalloproteinase-2 and -9 expression. Wang, et al. (21), investigated the invading tumor front following radiotherapy, and concluded that tumor-secreted stromal cell-derived factor-1, which regulates macrophage recruitment and vessel vascularization, is a potential key factor responsible for increased tumor invasiveness and proliferation, leading to treatment resistance. Brown, et al. (31), used a partial RT field to simulate residual tumor at the edge of the treatment field, but limited animal survival rates precluded characterization of the delayed, late radiation effects to the microenvironment.

In contrast to these previous preclinical animal models, which involved delivery of radiation to established tumors, our model simulates the delayed effects of radiation therapy on the microenvironment that lead to aggressive, infiltrative tumor growth patterns and likely contribute to treatment resistance in patients. The development and characterization of a novel, animal model that simulates recurrent glioma tumor growth patterns in radiation-modulated brain will allow us to evaluate the potential cellular and molecular basis for glioma tumor resistance.

In the present study, we demonstrated that irradiation to the microenvironment leads to a remarkable pattern of aggressive, infiltrative tumor regrowth. Our data showed that DBT-cell tumors grew much more rapidly in the irradiated tissue, resulting in increased lesion mass associated with significantly decreased survival (**Figures 1 & 2**). Anatomic MRI and histologic studies confirmed aggressive growth patterns for tumor cells implanted into previously irradiated

brain parenchyma. These tumors developed large areas of hemorrhagic necrosis and leaky vasculature, with substantial contrast enhancement, consistent with the features of recurrent high-grade tumor in patients. In contrast to the well-circumscribed tumor edges observed in the non-irradiated, control group, tumors in the irradiated microenvironment also developed increased tumor satellites (**Figure 3**), an indicator of increased invasiveness. Collectively, these data suggest that we have developed a model of recurrent GBM that simulates delayed, radiation-modulated alterations in the tumor microenvironment following brain radiotherapy, leading to aggressive, invasive tumor regrowth and treatment resistance.

To date, therapeutic regimens have largely targeted initial (primary) tumor phenotypes, not those recurrent phenotypes induced by radiation modulation of the TME. This may explain the failure of many potential therapeutic agents to translate successfully from *in vitro* studies to the clinic. Adopting multi-faceted approaches that not only target initial disease, but also anticipate subsequent changes in recurrent-tumor phenotype, driven by radiation modulation of the TME, may lead to improved patient outcomes.

In conclusion, our innovative preclinical model simulates the delayed effects of radiation upon the microenvironment, leading to aggressive, infiltrative tumor growth and invasiveness, and providing new insights into recurrent gliomas. This model can, therefore, serve as a novel platform for (i) improving our understanding of the mechanisms of tumor resistance and regrowth in the irradiated brain, (ii) developing novel, imaging biomarkers for distinguishing recurrent tumor from post-IR treatment effects, and (iii) improving the therapeutic ratio, by developing therapeutic strategies in a clinically relevant model that are directly translatable to the clinic.

5.5 Acknowledgments

This project was supported by NIH grant R01 CA155365 (JRG), funding from the Alvin J. Siteman Cancer Center (P30 CA091842), the Barnes-Jewish Hospital Foundation Cancer Frontier Fund, and Elekta Instruments AB (Stockholm, Sweden). We thank Dr. Robert Drzymala and Mr. Jeremy Cates (Radiation Oncology, Washington University) for their assistance in irradiating mice and Dr. Dinesh Thotala (Radiation Oncology, Washington University) for providing the DBT tumor cells.

5.6 References

1. Walker MD, Green SB, Byar DP, Alexander Jr E, Batzdorf U, Brooks WH, et al. Randomized comparisons of radiotherapy and nitrosoureas for the treatment of malignant glioma after surgery. *N Engl J Med*. 1980;303:1323–1329.
2. Stupp R, Mason WP, Van Den Bent MJ, Weller M, Fisher B, Taphoorn MJ, et al. Radiotherapy plus concomitant and adjuvant temozolomide for glioblastoma. *N Engl J Med*. 2005;352:987–996.
3. Becker KP, Yu J. Status quo—standard-of-care medical and radiation therapy for glioblastoma. *Cancer J*. 2012;18:12–19.
4. Bhide S, Nutting C. Recent advances in radiotherapy. *BMC Med*. 2010;8:25.
5. Morris DE, Bourland JD, Rosenman JG, Shaw EG. Three-dimensional conformal radiation treatment planning and delivery for low- and intermediate-grade gliomas. *Semin Radiat Oncol*. 2001;11:124–37.
6. Hermanto U, Frija EK, Lii MJ, Chang EL, Mahajan A, Woo SY. Intensity-modulated radiotherapy (IMRT) and conventional three-dimensional conformal radiotherapy for high-grade gliomas: Does IMRT increase the integral dose to normal brain? *Int J Radiat Oncol*. 2007;67:1135–44.
7. Sneed PK, Gutin PH, Larson DA, Malec MK, Phillips TL, Prados MD, et al. Patterns of recurrence of glioblastoma multiforme after external irradiation followed by implant boost. *Int J Radiat Oncol*. 1994;29:719–27.
8. Liang BC, Thornton AF, Sandler HM, Greenberg HS. Malignant astrocytomas: focal tumor recurrence after focal external beam radiation therapy. *J Neurosurg*. 1991;75:559–63.
9. Oppitz U, Maessen D, Zunterer H, Richter S, Flentje M. 3D-recurrence-patterns of glioblastomas after CT-planned postoperative irradiation. *Radiother Oncol J Eur Soc Ther Radiol Oncol*. 1999;53:53–7.

10. Bao S, Wu Q, McLendon RE, Hao Y, Shi Q, Hjelmeland AB, et al. Glioma stem cells promote radioresistance by preferential activation of the DNA damage response. *Nature*. 2006;444:756–60.
11. Hambardzumyan D, Squartro M, Holland EC. Radiation resistance and stem-like cells in brain tumors. *Cancer Cell*. 2006;10:454–6.
12. Jordan CT, Guzman ML, Noble M. Cancer Stem Cells. *N Engl J Med*. 2006;355:1253–61.
13. Wicha MS, Liu S, Dontu G. Cancer stem cells: an old idea--a paradigm shift. *Cancer Res*. 2006;66:1883-1890; discussion 1895-1896.
14. Tamura K, Aoyagi M, Ando N, Ogishima T, Wakimoto H, Yamamoto M, et al. Expansion of CD133-positive glioma cells in recurrent de novo glioblastomas after radiotherapy and chemotherapy. *J Neurosurg*. 2013;119:1145–55.
15. Hambardzumyan D, Gutmann DH, Kettenmann H. The role of microglia and macrophages in glioma maintenance and progression. *Nat Neurosci*. 2016;19:20–7.
16. Barker HE, Paget JTE, Khan AA, Harrington KJ. The tumour microenvironment after radiotherapy: mechanisms of resistance and recurrence. *Nat Rev Cancer*. 2015;15:409–25.
17. Feys L, Descamps B, Vanhove C, Vral A, Veldeman L, Vermeulen S, et al. Radiation-induced lung damage promotes breast cancer lung-metastasis through CXCR4 signaling. *Oncotarget*. 2015;6:26615–32.
18. Ohuchida K, Mizumoto K, Murakami M, Qian L-W, Sato N, Nagai E, et al. Radiation to Stromal Fibroblasts Increases Invasiveness of Pancreatic Cancer Cells through Tumor-Stromal Interactions. *Cancer Res*. 2004;64:3215–22.
19. Ahn G-O, Tseng D, Liao C-H, Dorie MJ, Czechowicz A, Brown JM. Inhibition of Mac-1 (CD11b/CD18) enhances tumor response to radiation by reducing myeloid cell recruitment. *Proc Natl Acad Sci*. 2010;107:8363–8.
20. Wild-Bode C, Weller M, Rimner A, Dichgans J, Wick W. Sublethal irradiation promotes migration and invasiveness of glioma cells Implications for radiotherapy of human glioblastoma. *Cancer Res*. 2001;61:2744–2750.
21. Wang S-C, Yu C-F, Hong J-H, Tsai C-S, Chiang C-S. Radiation Therapy-Induced Tumor Invasiveness Is Associated with SDF-1-Regulated Macrophage Mobilization and Vasculogenesis. *PLOS ONE*. 2013;8:e69182.
22. Badiga AV, Chetty C, Kesanakurti D, Are D, Gujrati M, Klopfenstein JD, et al. MMP-2 siRNA Inhibits Radiation-Enhanced Invasiveness in Glioma Cells. *PLoS ONE* [Internet]. 2011 [cited 2016 Oct 10];6. Available from: <http://www.ncbi.nlm.nih.gov/pmc/articles/PMC3116828/>
23. Desmarais G, Charest G, Fortin D, Bujold R, Mathieu D, Paquette B. Cyclooxygenase-2 inhibitor prevents radiation-enhanced infiltration of F98 glioma cells in brain of Fischer rat. *Int J Radiat Biol*. 2015;91:624–33.

24. Desmarais G, Charest G, Therriault H, Shi M, Fortin D, Bujold R, et al. Infiltration of F98 glioma cells in Fischer rat brain is temporary stimulated by radiation. *Int J Radiat Biol.* 2016;92:444–50.
25. Jost SC, Wanebo JE, Song S-K, Chicoine MR, Rich KM, Woolsey TA, et al. In vivo imaging in a murine model of glioblastoma. *Neurosurgery.* 2007;60:360–371.
26. Kumanishi T, Ikuta F, Yamamoto T. Brain Tumors Induced by Rous Sarcoma Virus, Schmidt-Ruppin Strain. III. Morphology of Brain Tumors Induced in Adult Mice. *J Natl Cancer Inst.* 1973;50:95–109.
27. Jiang X, Yuan L, Engelbach JA, Cates J, Perez-Torres CJ, Gao F, et al. A Gamma-Knife-Enabled Mouse Model of Cerebral Single-Hemisphere Delayed Radiation Necrosis. *PloS One.* 2015;10:e0139596.
28. Suit HD. Local control and patient survival. *Int J Radiat Oncol Biol Phys.* 1992;23:653–660.
29. Massey V, Wallner KE. Patterns of second recurrence of malignant astrocytomas. *Int J Radiat Oncol Biol Phys.* 1990;18:395–398.
30. Garden AS, Maor MH, Yung WA, Bruner JM, Woo SY, Moser RP, et al. Outcome and patterns of failure following limited-volume irradiation for malignant astrocytomas. *Radiother Oncol.* 1991;20:99–110.
31. Kumar S, Arbab AS, Jain R, Kim J, deCarvalho AC, Shankar A, et al. Development of a novel animal model to differentiate radiation necrosis from tumor recurrence. *J Neurooncol.* 2012;108:411–20. his project was supported by NIH grant R01 CA155365 (JRG), funding from the Alvin J. Siteman Cancer Center (P30 CA091842), the Barnes-Jewish Hospital Foundation Cancer Frontier Fund, and Elekta Instruments

Chapter 6 Summary and Future Research

6.1 Summary

The vasculature of tumors is fundamentally different from that of normal tissues. Thus, the temporal and spatial variation in the structure of vasculature offers valuable information on assessing tumor characteristics and potential treatment responses. In this dissertation, we have investigated the use of dynamic contrast-enhanced MRI in measuring vascular perfusion and permeability for cancers. In Chapter 2, a Bayesian-probability theory based, data-driven, model selection approach was developed for the determination of an optimal model for the pharmacokinetic modeling of any given dynamic contrast-enhanced MRI data. It was found that highly parameterized, complex models require higher data quality for accurate and stable model parameter estimation. In the absence of performing a model-selection calculation, these complex models should be employed cautiously. In Chapter 3, a constrained, local arterial input function (cL-AIF) model was developed to improve the pharmacokinetic modeling of dynamic contrast-enhanced MRI data, by accounting the voxel-specific contrast agent bolus arrival-time delay and amplitude errors. The cL-AIF method provides accurate and precise vascular parameter estimates under signal-to-noise conditions representative of clinical DCE-MRI. Further, as expected with heterogeneous cancer tissue, the estimated, voxel-specific cL-AIF show local variations in contrast agent bolus amplitude and arrival time.

In this dissertation, we have also investigated the radiation treatment effects in brain. Radiotherapy is a central component of the standard treatment for patients with cancer. While radiation exerts its therapeutic effect by killing tumor cells, increasing evidences demonstrate that radiation induces vascular, stromal and immune changes in normal tissue. In Chapter 4, we studied the late

time-to-onset radiation-induced necrosis employing a Gamma Knife-enabled animal model. The efficacy of anti-vascular endothelial growth factor treatment of frank, developed radiation necrosis was evaluated using both MRI and gold standard histology. It was shown that anti-VEGF antibody treatment decreased RN lesion volumes on post-contrast T1W and T2W images. In addition, the abnormally high RN ADCs were reduced to values typical of normal brain. However, large amount of focal calcification were presented in the treated brains, and the expression of VEGF and HIF-1 α were continually upregulated, which merit further clinical and pre-clinical investigation. In Chapter 5, we investigated the effects of radiation-modulated brain parenchyma on the growth of naïve, non-irradiated tumor cells, in an innovative preclinical model simulating the delayed effects of radiation upon the microenvironment. We demonstrated that irradiation to the microenvironment leads to a remarkable pattern of aggressive, infiltrative tumor regrowth. This model can serve as a novel platform for improving our understanding of the mechanisms of tumor resistance and regrowth in the irradiated brain.

6.2 Future Research

DCE-MRI with Golden-Angle Radial Sampling

Dynamic contrast-enhanced MRI continuously acquires T_1 -weighted images to monitor the passage of an intravenously injected, Gd-based, contrast agent bolus. It normally requires the determination of an appropriate temporal resolution before the experiments. Recently, Feng Li et al. (1) introduced a radial golden-angle k-space data acquisition scheme, together with iterative reconstruction procedure on the undersampled time series, for rapid dynamic volumetric MRI. The continuous sampling of radial data, with a 111.25° increment, provides relatively uniform coverage of k-space with high temporal incoherence. Further, the radial trajectories in k-space is less sensitive to periodic (e.g., respirational and cardiac motion) and non-periodic (e.g., patient

movement) motion. Most importantly, this approach enables retrospective reconstruction of image time series by re-grouping the radial trajectories with arbitrary temporal resolution. Glioblastoma DCE-MRI studies employing this sampling technique are currently ongoing in our lab. Besides increased motion robustness, this approach also potentially allows to analyze the effects of temporal resolution and SNR on the pharmacokinetic parameter estimation in DCE-MRI data analysis.

Characterizing Vascular Properties of Radiation Treatment Effects with DCE-MRI

In this dissertation, Chapters 2-3 focused on the measurement of vascular properties using DCE-MRI, while Chapters 4-5 focused on the radiation treatment effects in brain. It seems natural to apply DCE-MRI on the current mouse model of radiation treatment effects, as those effects are always associated with vascular pathologies. Nevertheless, the application of quantitative DCE-MRI on preclinical model, especially mouse, is largely hampered by the difficulties in obtaining an arterial input function due to the lack of appropriate, well-resolved, arteries within the imaging field of view. Future effects will be focused on AIF-free modeling approaches for quantitative DCE-MRI, such as the reference region methods introduced by Yankeelov TE, et al.(2).

Irradiation Dose, Fractionation and Tumor-Cell Implantation Time Point

In Chapter 4, a single-fraction 50 Gy dose Gamma Knife irradiation was employed to generate the late time-to-onset radiation necrosis on a mouse model. In Chapter 5, to investigate the effects of radiation-modulated microenvironment, in the absence of radiation necrosis, on the growth of naïve glioblastoma cells, a single-fraction 30 or 40 Gy GK irradiation were used. Outstanding questions remain regarding whether (and how) the Gamma Knife irradiation dose and fractionation scheme affect the radiation treatment effects, including the development of radiation necrosis. Specifically, many studies have demonstrated that irradiation of the vasculature leads to dose-

dependent structural destruction of blood vessels (3,4). For our preclinical investigation, a high-end dosing scheme (i.e., single-fraction of high dose) was chosen because rodents are widely known to be more radioresistant than humans. Thus, it will be an interesting follow-up to study the radiation treatment effects under different irradiation scheme (total dose and fractionation). Further, in Chapter 5, non-irradiated glioma cells were implanted into the irradiated brain at six weeks post-irradiation. The radiation-modulated brain parenchyma dramatically enhanced the development of naïve glioma cells. Critical question also remain regarding the tumor-cell implantation time point (e.g., when the tumor-growth promoting effect of irradiated brain arises and how long it lasts post-irradiation).

Therapeutic Agents Targeting Specifically at Tumors Developed in Irradiated Brain

In Chapter 5, we introduced a novel animal model simulating tumors developed in radiation-modulated tumor microenvironment. To date, therapeutic regimens have largely targeted initial (primary) tumor phenotypes, not those recurrent phenotypes induced by radiation modulation of the tumor microenvironment. This may explain the failure of many potential therapeutic agents to translate successfully from *in vitro* studies to the clinic. Adopting multi-faceted approaches that not only target initial disease, but also anticipate subsequent changes in recurrent-tumor phenotype, driven by radiation modulation of the TME, may lead to improved patient outcomes. The innovative preclinical model, developed in Chapter 5, simulates the delayed effects of radiation upon the microenvironment. This model can, therefore, serve as a novel platform for developing and evaluating therapeutic strategies in a clinically relevant model for recurrent tumors developed in irradiated tumor microenvironment.

6.3 References

1. Feng L, Grimm R, Block KT, Chandarana H, Kim S, Xu J, Axel L, Sodickson DK, Otazo R. Golden-angle radial sparse parallel MRI: Combination of compressed sensing, parallel imaging, and golden-angle radial sampling for fast and flexible dynamic volumetric MRI. *Magn. Reson. Med.* 2014;72:707–717. doi: 10.1002/mrm.24980.
2. Yankeelov TE, Luci JJ, Lepage M, Li R, Debusk L, Lin PC, Price RR, Gore JC. Quantitative pharmacokinetic analysis of DCE-MRI data without an arterial input function: a reference region model. *Magn. Reson. Imaging* 2005;23:519–529.
3. Baker DG, Krochak RJ. The Response of the Microvascular System to Radiation: A Review. *Cancer Invest.* 1989;7:287–294. doi: 10.3109/07357908909039849.
4. Lerman OZ, Greives MR, Singh SP, et al. Low-dose radiation augments vasculogenesis signaling through HIF-1–dependent and –independent SDF-1 induction. *Blood* 2010;116:3669–3676. doi: 10.1182/blood-2009-03-213629.

Appendix A: Hyperthermic Laser Ablation of Recurrent Glioblastoma Leads to Temporary Disruption of the Peritumoral Blood Brain Barrier¹

A.1 Introduction

Glioblastoma (GBM) is the most common and lethal malignant brain tumor in adults (1). Despite advanced treatment, median survival is less than 15 months, and fewer than 5% of patients survive past 5 years (2-3). Effective treatment options for recurrent GBM remain very limited and much of research and development efforts in recent years have focused on this area of greatly unmet needs. Most recurrent tumors develop within the 2-3 cm margin of the primary site and are thought to arise from microscopic tumor cells that infiltrate the peritumoral region prior to resection of the primary tumor (4). Therefore elimination of micrometastatic GBM cells in this region likely will improve long-term disease control.

Inadequate CNS delivery of therapeutic drugs due to the blood brain barrier (BBB) has been a major limiting factor in the treatment of brain tumors. The presence of contrast enhancement on standard brain MRI qualitatively reflects a disrupted state of the BBB. For this reason, drug access to the viable contrast enhanced tumor rim is likely significantly higher than to the peritumoral region, which usually does not have contrast enhancement (5-6). Evidence supporting this hypothesis came from studies in which drug levels of cytotoxic agents were sampled in tumors

¹ All contents in this chapter have been published in Leuthardt EC*, Duan C*, Kim MJ, Campian JL, Kim AH, Miller-Thomas MM, Shimony JS, and Tran DD (2016) Hyperthermic Laser Ablation of Recurrent Glioblastoma Leads to Temporary Disruption of the Peritumoral Blood Brain Barrier. *PLoS ONE* 11(2):e0148613. doi:10.1371/journal.pone.0148613. (*These authors contributed equally to this work)

and the surrounding brain tissue at the time of surgery or autopsy. Drug concentrations were at the highest in the enhancing portion of tumors, and then rapidly decreased up to 40 fold lower by 2-3 cm distance from the viable tumor edge (7-9). Overall, these observations suggest that the BBB and its integrity negatively correlate with delivery and potentially therapeutic effects of BBB impermeant drugs.

To circumvent the BBB problem in local drug delivery, recent approaches have focused on bypassing it. A previously described method is the use of Gliadel, a polymer wafer impregnated with the chemotherapeutic agent carmustine (BCNU) and placed intra-operatively in the resection cavity to bypass the BBB. This approach resulted in a statistically significant but modest survival advantage in both newly diagnosed and recurrent GBM (10-12). The modest benefit of Gliadel could be due to the short duration of drug delivery as nearly 80% of BCNU is released from the wafer over a period of only 5 days (13). This observation further supports the notion that the BBB is critical to chemotherapy effect. However, Gliadel is not widely utilized as it requires an open craniotomy and can impair wound healing. Another approach of bypassing the BBB is the convection-enhanced delivery system in which a catheter is surgically inserted into the tumor to deliver chemotherapy (14). This procedure requires prolonged hospitalization to maintain the external catheter to prevent serious complications and as a result has not been used extensively.

The role of hyperthermia in inducing BBB disruption has been previously described in animal models of CNS hyperthermia. In a rodent model of glioma, the global heating of the mouse's head to 42°C for 30 minutes in a warm water bath significantly increased the brain concentration of a thermosensitive liposome encapsulated with Adriamycin chemotherapy (15). To effect more locoregional hyperthermia, retrograde infusion of a saline solution at 43°C into the left external carotid artery in the Wistar rat reversibly increased BBB permeability to Evans-blue albumin in

the left cerebral hemisphere (16). In another approach, neodymium-doped yttrium aluminium garnet (Nd:YAG) laser-induced thermotherapy to the left forebrain of Fischer rats resulted in locoregional BBB disruption as evidenced by passage of Evans blue dye, serum proteins (e.g. fibrinogen & IgM), and the chemotherapeutic drug paclitaxel for up to several days after thermotherapy (17). The effect of hyperthermia on the BBB of human brain has not been examined.

Here we describe an approach to induce sustained, local disruption of the peritumoral BBB using MRI-guided laser interstitial thermal therapy, or LITT. The biologic effects and correlation with MRI findings of LITT have been studied in both animal and human models since the development of LITT over twenty years ago. A well-described zonal distribution of histopathological changes with corresponding characteristic MR imaging findings centered on the light-guide track replace the lesion targeted for thermal therapy. The central treatment zone shows development of coagulative necrosis with complete loss of normal neurons or supporting structures immediately following therapy, corresponding to hyperintense T1-weighted signal intensity relative to normal brain (18-21). The peripheral zone of the post-treatment lesion is characterized by avid enhancement with intravenous gadolinium contrast agents, which peaks several days following thermal therapy and persists for many weeks after the procedure. Gadolinium contrast enhancement in the brain following LITT is due to leakage of gadolinium contrast into the extravascular space across a disrupted BBB (19-22). The perilesional zone of hyperintense signal intensity of FLAIR-weighted images develops within 1-3 days of thermal treatment and persists for 15- 45 days (21).

We demonstrate that in addition to cytoreductive ablation of the main recurrent tumor, hyperthermic exposure of the peritumoral region resulted in localized, lasting disruption of the

BBB as quantified by dynamic contrast-enhanced MRI (DCE-MRI) and serum levels of brain-specific enolase (BSE), thus providing a therapeutic window of opportunity for enhanced delivery of therapeutic agents.

A.2 Material and methods

Patient Selection

Adult patients (age ≥ 18 years) with unequivocal evidence of recurrent bevacizumab-naïve, histologically confirmed GBM were screened for eligibility to participate in an IRB approved protocol. Patients with prior diagnosis of a WHO grade II or III gliomas were eligible if the recurrent tumor had radiographic characteristics of a GBM, WHO grade IV. For these subjects to be included a biopsy was obtained immediately prior to LITT and subsequent pathologic analysis must have confirmed secondary GBM, WHO grade IV. General characteristics that make the lesion(s) favorable to treatment include the following: (a) the lesion(s) is (are) supratentorial and accessible from a cephalad approach (i.e., top one third of the head), (b) the lesion(s) is (are) unilateral, (c) the lesion(s) is (are) relatively well circumscribed, (d) the volume of lesion(s) can be encompassed by two 3-cm cylinders (i.e., 2 treatment trajectories), (e) a safe trajectory can be established relative to functional structures (i.e., eloquent cortex and corticospinal tract), and (f) the patient's body habitus can fit into the bore of the MRI. The primary objectives of the protocol are to determine MR imaging correlates and serum biomarkers of peritumoral BBB disruption after LITT.

Study design

The pilot study has 2 main objectives: 1) To determine the safety of LITT in patients with recurrent GBM and spatiotemporal MR imaging correlates and serum biomarkers of peritumoral BBB

disruption after LITT; and 2) To determine whether treatment with the BBB impermeant chemotherapy agent doxorubicin dosed at 20mg/m² IV weekly for 6 doses during the window of post-LITT BBB disruption is safe and will improve local disease control compared to when the same agent given during the window of intact BBB. The first 10 patients were assigned to the late (starting 6 weeks after LITT) doxorubicin treatment arm so that MRI and serum biomarker measurements can be performed without potential confounding effects of chemotherapy. The next 30 patients are randomized at the ratio of 2 to 1 to either early (starting within 1 week after LITT) or late doxorubicin treatment to achieve the final distribution of 20 patients in each arm. Non-evaluable patients due to any reason will be replaced. Data collected in the first 10 weeks after LITT from the first 20 enrolled patients were focused on the biophysical parameters of measurements of BBB disruption, which is independent from the second objective and provides the foundation for this report (Figure A.1). Patients underwent a pre-LITT baseline DCE-MRI and biomarker measurement within 48 hours prior to LITT. Patients underwent post-LITT baseline DCE-MRI and biomarker measurement within 48 hours after LITT. Subsequent DCE-MRIs were performed at weeks 2, 4, 6, and 10 after LITT. Biomarker measurements were performed weekly for 6 weeks and at week 10 after LITT patients underwent a pre-LITT baseline DCE-MRI and biomarker measurement within 48 hours prior to LITT. Patients underwent post-LITT baseline DCE-MRI and biomarker measurement within 48 hours after LITT. Subsequent DCE-MRIs were performed at weeks 2, 4, 6, and 10 after LITT. Subsequent biomarker measurements were performed weekly for 6 weeks and at week 10 after LITT.

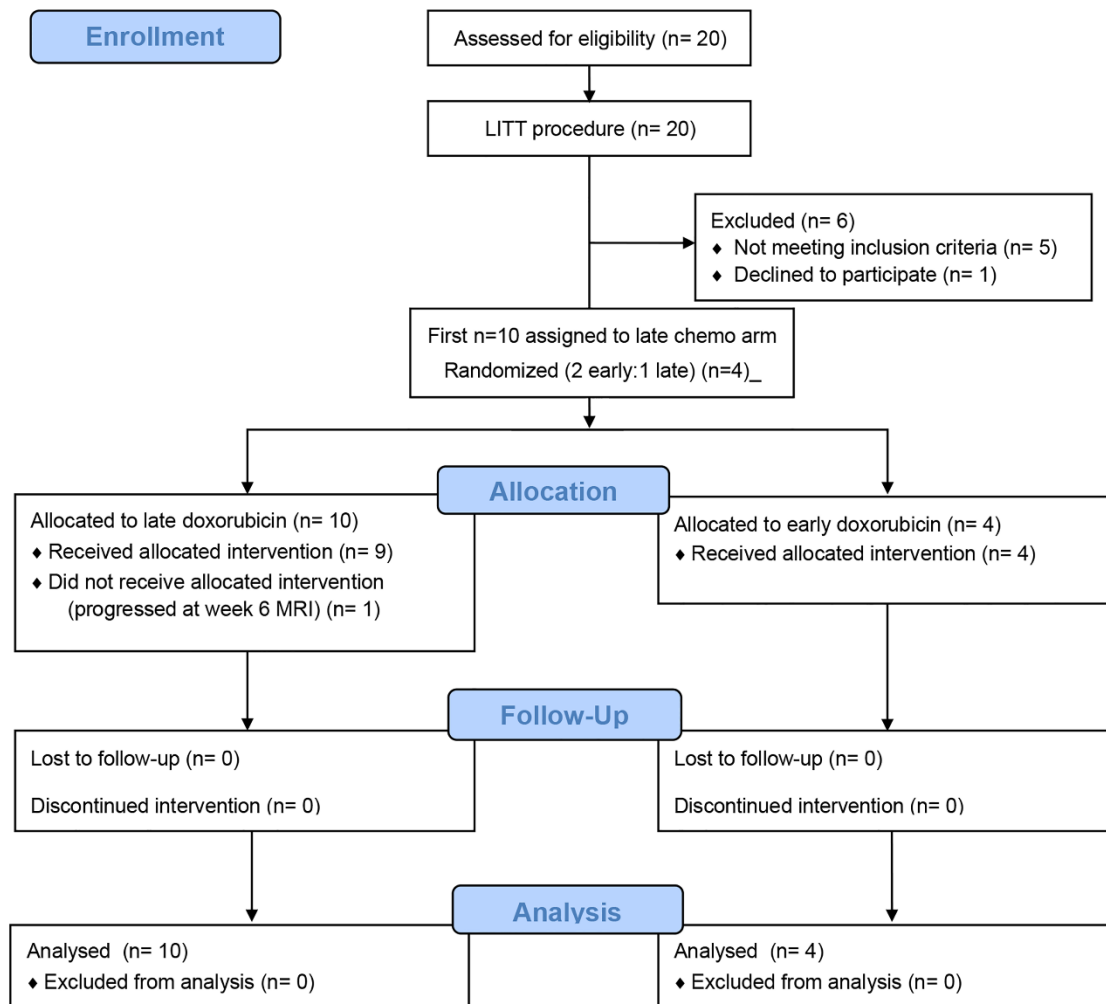


Figure A.1: Consort flow diagram of the BBB disruption measurement portion of the pilot phase 2 study involving the first 20 enrolled patients. Early or Early doxorubicin: Treatment started within 1 week after LITT. Late or Late doxorubicin: Treatment started at 6 weeks after LITT

MRI-guided Laser Thermal Ablation Therapy (LITT)

The Neuroblate system, Monteris, Inc, was used to deliver LITT of GBM. LITT is a minimally invasive laser surgery currently cleared by the FDA for interstitial thermal treatment of brain lesions with 1064 nm lasers (23-26). LITT employs a small incision in the scalp and skull, through which a thin laser probe is inserted and guided by MR imaging to the core of a tumor mass where it delivers hyperthermic ablation with the maximal temperature in tumor core reaching 60-70°C resulting in coagulative necrosis, while the temperature decreases to 40-45°C in the peritumoral

region (26). Trajectories are chosen to maximize lesion ablation and minimize the number of passes. Live intra-procedural repetitive measurements of a T1-weighted 2-dimensional-FLASH sequence provide temporally sensitive thermometry measurements necessary to create controlled and conformal lesions.

DCE-MRI

Dynamic contrast-enhancement (DCE) is a method that relies on dynamically measuring the changes in T1-weighted images following the administration of contrast agent (27). Using pharmacokinetic modeling this method can estimate the vascular transfer constant (K^{trans}) (28). K^{trans} describes the ability of contrast to move from the intravascular compartment to the extracellular extravascular compartment and thus provide a quantitative measure of the degree of BBB leakage (28).

MRI Protocol

Standard of care imaging with added DCE-MRI was obtained within 48 hours prior to, within 48 hours after and then at weeks 2, 4, 6, and 10 after LITT. All patients were scanned on the same Siemen's Avanto 1.5T MRI (Erlanger, Germany) identically using a tumor follow up standard of care imaging protocol that including anatomical imaging sequences (T1-weighted pre and post-contrast, T2-weighted images, FLAIR images) augmented with rapid T1-weighted DCE protocol (3D gradient echo, TR/TE = 4.8/2.4ms, matrix 256x256x44, voxel size 1.5x1.5x4mm, temporal resolution 10s, for a total of 6min after the administration of Multihance (Gadobenate Dimeglumine, Bracco) 0.1 mmol/kg injected at a rate of 5 mL/s.

Data analysis

Regions of interest (ROIs) were defined on the enhancing ring surrounding the ablated tumor on the DCE-MRI images using post-contrast T1-weighted image and FLAIR images for guidance. The ROI was selected on the portion of the ring that demonstrated maximal contrast enhancement and were within 1cm of the margin of ablation. The outlined ROIs were transferred to all the other DCE time point measurements within each dataset. Signal intensity vs. time curves was generated as the average within the ROIs. To avoid partial volume effect, an arterial input function (AIF) was obtained from one voxel in the center of the middle cerebral artery (MCA) for each dataset. The MR signal intensities were then converted to contrast agent concentrations as described in Kallehauge et al. (29), using reported pre-contrast T_1 and contrast agent relaxivity.

Quantitative pharmacokinetic parameters (K^{trans} and v_e) were estimated for each dataset by applying a standard Tofts Model (27):

$$C_t(t) = K^{trans} \times \int_0^t C_a(\tau) \times e^{-\frac{K^{trans}}{v_e} \times (t-\tau)} d\tau \quad (1)$$

where $C_t(t)$ is the tissue contrast agent concentration vs. time curve obtained at the enhanced region following the administration of contrast agent bolus, $C_a(t)$ is the concentration of the contrast agent in the plasma of the capillary inlet of the tissue and is approximated by the measured upstream AIF following the standard DCE-MRI analysis approach (30), K^{trans} is the forward volume transfer constant (from vascular space to extravascular extracellular space), which is a direct reflection of capillary permeability, and v_e is the extravascular extracellular volume fraction.

All pharmacokinetic modeling was performed using a custom written Bayes Data-Analysis Toolkit (<http://bayesiananalysis.wustl.edu>). The posterior probabilities for all the model parameters were

computed by an application of Bayes' Theorem with Markov-chain Monte Carlo simulation. Initial values for all the parameters were sampled from the prior probability for each parameter. Uniformly distributed prior probabilities bounded by appropriate physiological ranges were assigned to all of the parameters. The prior ranges selected are $0-6.0\text{min}^{-1}$ for K^{trans} , and 0-1 for v_e . In the current study we focused on the values of the K^{trans} . Computations were carried out on Dell PowerEdge R900 servers (Dell, Inc., Round Rock, TX), vintage 2008. All MCMC calculations were performed with 48 simulations and 50 repetitions. Further details about Bayesian parameter estimation are given in Lee et al. (31).

Data analysis

Serum levels of BSE were measured using an ELISA kit (Alpco) per the manufacturer's instructions.

Statistical analysis

For serum BSE optimization analysis, 2-sided Student T test was used. Pearson correlation coefficients were calculated between the time courses of K^{trans} , serum BSE levels, and the area of FLAIR abnormality for each of the subjects. Since the MRI measurements were only performed at a few time points the curves were interpolated into a smooth curve using piecewise cubic Hermite interpolation.

A.3 Results

A.3.1 Patient characteristics and treatment course

Twenty bevacizumab-naïve patients with suspected recurrent GBM were enrolled in the study. Fifteen patients (1, 4, 5, 7, 9, 10, 12-20) were diagnosed histologically with primary GBM, WHO grade IV. All received standard concurrent radiation and temozolomide chemotherapy per the Stupp protocol (2-3), except for Patient 9, who received radiation alone without concurrent

temozolomide, followed by standard adjuvant temozolomide. Patient 4 withdrew consent. Patients 2, 6, and 11 and Patients 3 and 8 were initially diagnosed with a WHO grade III and grade II glioma, respectively, and subsequently developed recurrent tumor with radiographic appearances of probable transformed or secondary GBM. However needle biopsy immediately prior to LITT failed to demonstrate secondary GBM, which rendered these patient non-eligible. Several patients had participated in prior clinical trials for newly diagnosed GBM. All recurrent tumors were approximately 3 cm or less at the longest dimension (Table A.1).

Table A.1: Patient Baseline Demographics and Characteristics. TMZ/RT: Stupp protocol of 60 Gy radiotherapy plus concurrent 75mg/m² daily temozolomide. Doxorubicin treatment: Timing of 20mg/m² IV weekly doxorubicin treatment after LITT. Early = Starting within 1 week after LITT; Late = Starting at 6 weeks after LITT.

PtN ^o	Age Range	Initial Diagnosis	Molecular Biomarkers	Tumor Location	TMZ/RT	Eligible?	Doxorubicin Treatment
1	50-60	GBM	Unmethylated MGMT	Left temporal	Yes	Yes	Late
2	40-50	Astrocytoma WHO grade III	1p, 19q intact; IDH1 wild-type	Left parietal	Yes	No (GBM unconfirmed)	N/A
3	60-70	Astrocytoma WHO grade II	1p, 19q intact; IDH1 wild-type	Left parietal	Yes	No (GBM unconfirmed)	N/A
4	50-60	GBM	Methylated MGMT	Right parietal	Yes	No	N/A
5	60-70	GBM	Unmethylated MGMT; EGFRvIII	Left temporal	Yes	Yes	Late
6	40-50	Astrocytoma WHO grade III	1p, 19q intact; IDH1 wild-type	Left temporal	Yes	No (GBM unconfirmed)	N/A
7	40-50	GBM	Methylated MGMT; EGFRvIII	Right frontal	Yes	Yes	Late
8	30-40	Oligoastrocytoma WHO grade II	1p, 19q intact; IDH1 R132H	Left insular	Yes	No (GBM unconfirmed)	N/A
9	50-60	GBM	Methylated MGMT; EGFRvIII	Left thalamic	No (RT only)	Yes	Late
10	60-70	GBM	Unmethylated MGMT	Left parietal	Yes	Yes	Late
11	40-50	Astrocytoma WHO grade III	1p, 19q intact; IDH1 R132H	Right frontal	Yes	No (biopsy, LITT not	N/A

						performed)	
12	60-70	GBM	Unmethylated MGMT	Left frontal	Yes	Yes	Late
13	60-70	GBM	MGMT methylation unknown	Right frontal	Yes	Yes	Late
14	60-70	GBM	Methylated MGMT; EGFRvIII	Right temporal	Yes	Yes	Late
15	60-70	GBM	Unmethylated MGMT	Right frontal	Yes	Yes	N/A
16	50-60	GBM	Unmethylated MGMT; EGFRvIII	Left frontal	Yes	Yes	Early
17	50-60	GBM	Unmethylated MGMT	Right parietooccipital	Yes	Yes	Early
18	50-60	GBM	Unmethylated MGMT; EGFRvIII	Left parietal	Yes	Yes	Late
19	70-80	GBM	Methylated MGMT; EGFRvIII	Left frontal	Yes	Yes	Early
20	60-70	GBM	Methylated MGMT; EGFRvIII	Right parietal	Yes	Yes	Early

A.3.2 Quantitative measurement of LITT-induced peritumoral BBB disruption by DCE-MRI

Brain MRI obtained within 48 hours following LITT showed the targeted tumor replaced by a post-treatment lesion corresponding to the volume of treated tissue on intraoperative thermometry maps. The post-treatment lesion lost the original rim of tumor-associated contrast enhancement and instead demonstrated central hyperintense T1-weighted signal compared to the pre-treated tumor and normal brain and a faint, newly developed discontinuous rim of peripheral contrast enhancement extending beyond the original tumor-associated enhancing rim (Figure 2.1A). These findings are consistent with a loss of viable tumor tissue caused by LITT, thus achieving an effective cytoreduction similar to open surgical resection. Of note, the rim of new peripheral contrast enhancement persisted for at least the next 28 days (Figure A.2B–Figure A.2E).

Perilesional edema qualitatively evaluated on FLAIR-weighted images increased from pretreatment MRI obtained within 48 hours following LITT showed the targeted tumor replaced by a post-treatment lesion corresponding to the volume of treated tissue on intraoperative thermometry maps. The post-treatment lesion demonstrated central hyperintense T1-weighted signal compared to normal brain and a faint discontinuous rim of peripheral contrast LITT. This rim of peripheral contrast enhancement persisted for at least the next 28 days. Perilesional edema qualitatively evaluated on FLAIR-weighted images increased from pretreatment imaging at week 2 and persisted at week 4 following LITT. Perilesional edema decreased on subsequent MRI examinations. These findings qualitatively indicate that peritumoral BBB is disrupted by LITT and that the disruption peaks within approximately 2 weeks after the procedure.

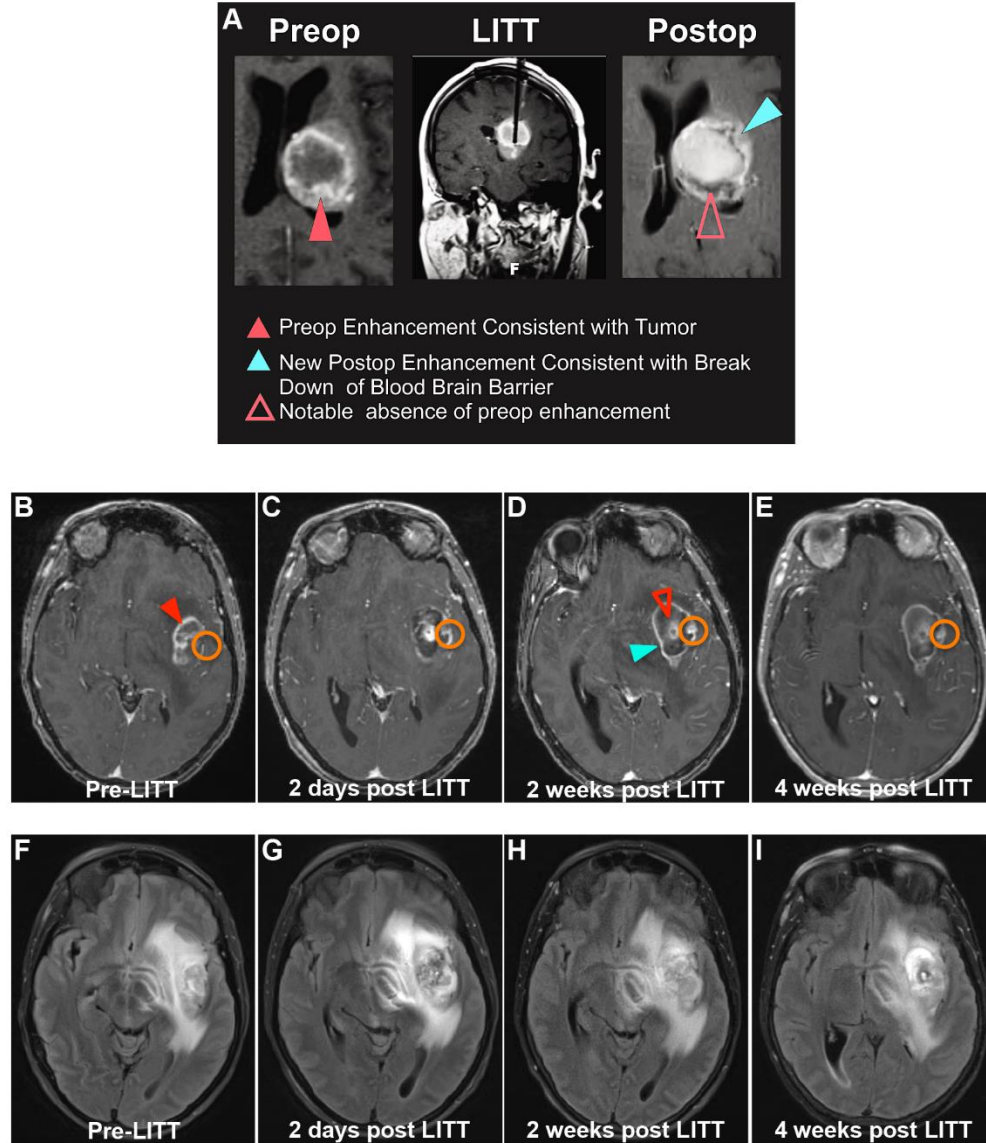


Figure A.2: Radiographic appearances of post-LITT changes. (A) A woman with a left thalamic GBM treated with LITT underwent axial and coronal T1-weighted post-contrast enhanced MR images of the brain pre- LITT, during LITT and 48 hours post LITT. (B-I) A woman with a left insula GBM underwent axial T1-weighted post-contrast enhanced (B-E) and axial FLAIR-weighted (F-I) MR images of the brain pre-LITT and within 48 hours post LITT, 2 weeks post LITT, and 4 weeks post LITT. In both cases, the enhancing tumor (solid red arrowheads in A and B) is replaced by a central zone of T1-weighted signal hyperintensity (open red arrowheads in A and D) and a faint, new discontinuous rim of enhancement extending beyond the original tumor associated enhancing rim (solid blue arrowheads in A and D). The rim of contrast enhancement intensifies at 2 weeks post LITT (D) and remains stable at 4 weeks post LITT (E). Perilesional edema evaluated on FLAIR-weighted images is slightly increased between the pre-treatment (F) and immediate post-treatment (G) images, increases to a maximum point on the 2-week post-

treatment images (H) and improves slightly by the 4-week images (I). The orange circles denote a representative ROI used to calculate temporal progression of K^{trans} after LITT.

Figure A.3 demonstrates the K^{trans} time curves for our cohort of patients. In all subjects the K^{trans} is highly elevated in the first few days after the procedure and then progressively decreases at approximately the 4-week time point. The bottom right subplot in Figure A.3 is an average of the K^{trans} time courses from all the subjects. This figure demonstrates the peak K^{trans} value immediately after the LITT procedure with persistent elevation out to about 4 weeks. Radiographically, persistent contrast enhancement and FLAIR hyperintensity were observed well past 6 weeks and in many cases more than 10 weeks later. Several patients had recurrent tumor by radiographic criteria (increasing size of the edema and enhancing area around the tumor site) and these patients also demonstrated a corresponding increase in the K^{trans} value. These recurrences occurred after the 10 week mark and thus were not included in Figure A.3. In summary, these results indicate that the peritumoral BBB disruption as measured by K^{trans} peaked immediately after LITT and persisted above baseline for an additional 4 weeks.

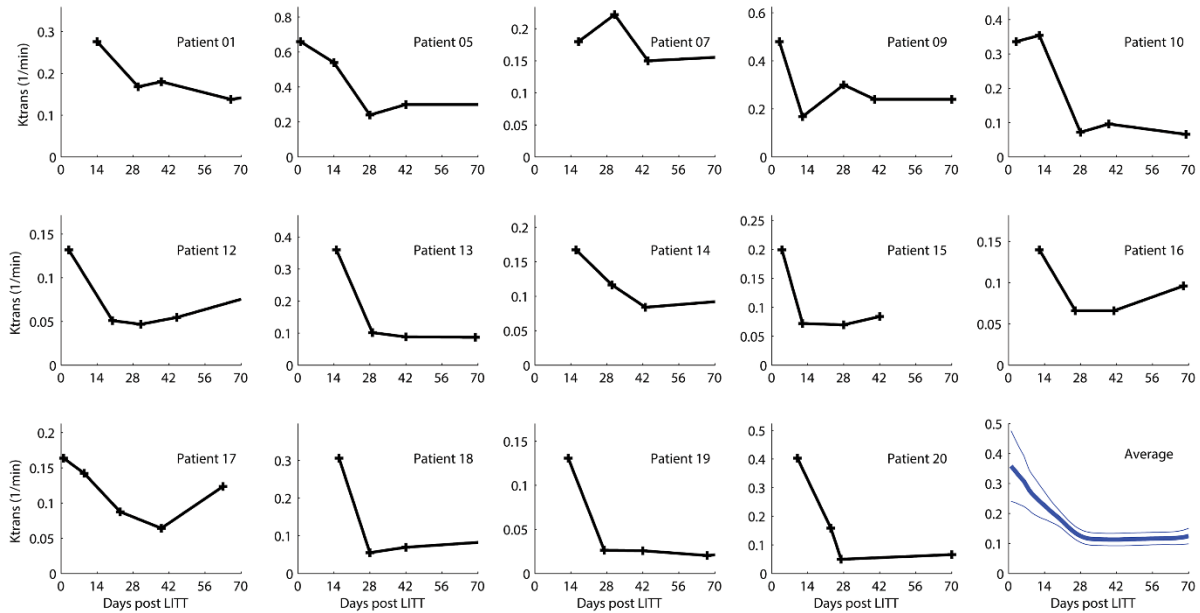
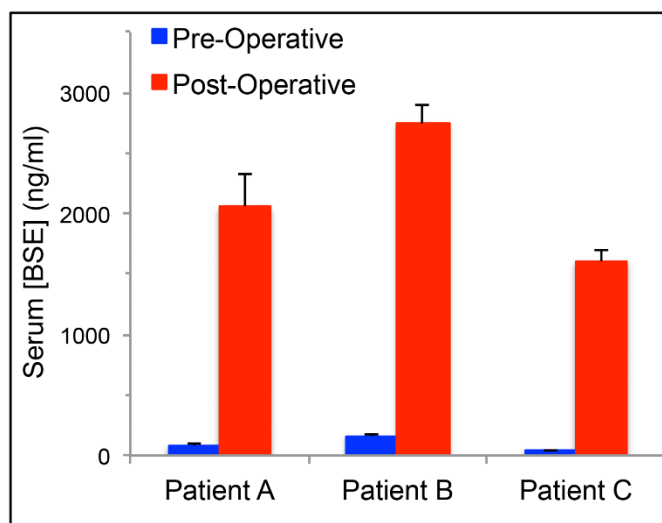


Figure A.3: K^{trans} for each of the 14 included subjects in the study as a function of time in days from the LITT procedure. In all subjects the K^{trans} is highly elevated in the first few days after the procedure and then progressively decreases out to approximately the 4-week time point. This is best illustrated in the bottom right which is an average of the 14 subject curves.

A.3.3 Quantitative measurement of LITT-induced peritumoral BBB disruption by serum BSE biomarker

We next sought another, independent method to quantify the degree of BBB disruption by measuring serum levels of the brain specific factor BSE that might be released into the circulation due to the increased BBB permeability using highly sensitive assays such as ELISA. This method has been validated for quantitative measurement of BBB disruption induced by several forms of brain injuries including surgery, traumatic brain injury, cerebrovascular accident and multiple sclerosis (32-34). To optimize the ELISA assay for BSE, we collected sera from 3 patients with a newly diagnosed low-grade (WHO grade 2) glioma before and after their planned craniotomy and surgical resection, and determined serum concentrations of BSE. WHO grade 2 gliomas were chosen for the optimization because as they are generally non-contrast enhanced tumors on brain MRI, tumor-associated BBB is relatively intact and consequently, serum concentrations of brain-

specific factors are predicted to be low pre-operatively and to then rise post-operatively due to the BBB compromise from the surgery. Serum BSE concentrations were low prior to surgery and then, as predicted, consistently increased after open craniotomy and tumor resection, thus indicating that this method had adequate sensitivity in detecting changes in serum levels of BSE due to disruption of the BBB (Figure A.4).



*Figure A.4: Optimization of the BSE ELISA assay for measuring BBB disruption. Serum concentrations of BSE before and after open craniotomy for surgical debulking in 3 subjects (A, B, and C) with a low-grade glioma, WHO grade II. * $p < 0.05$.*

We next determined concentrations of BSE in sera obtained from the 14 evaluable LITT patients within 48 hours prior to LITT, within 48 hours after LITT and weekly thereafter for 6 weeks, and then at week 10 after LITT, and compared them to K^{trans} values in the same patient. Serum BSE concentrations demonstrated a steady rise shortly after LITT, peaking by 2-3 weeks in most patients then gradually declining over the subsequent 2-3 weeks (Figure A.5). Compared to K^{trans} , peak concentrations of BSE were delayed by up to 1-2 weeks. Serum sample for Patient 1 was not obtained at week 10 since an amendment to the protocol to allow serum collection at this time point was not yet approved by the local IRB. Similar to the K^{trans} results, the serum BSE

concentration in Patient 12 rose rapidly after week 6, which coincided with the emergence of contrast-enhanced recurrent disease demonstrated on the brain MRI at week 10. Patient 15 had an early rise in serum BSE concentrations and a small increase in K^{trans} at week 4 (Figure A.5), and was also found to have contrast-enhanced multifocal recurrences at week 6 and therefore serum sample was not obtained at week 10. When combined with the DCE-MRI measurements, these results provide further confirmation that besides allowing for effective tumor cytoreduction LITT induces disruption of the peritumoral BBB that persists up to 4-6 weeks after the procedure.

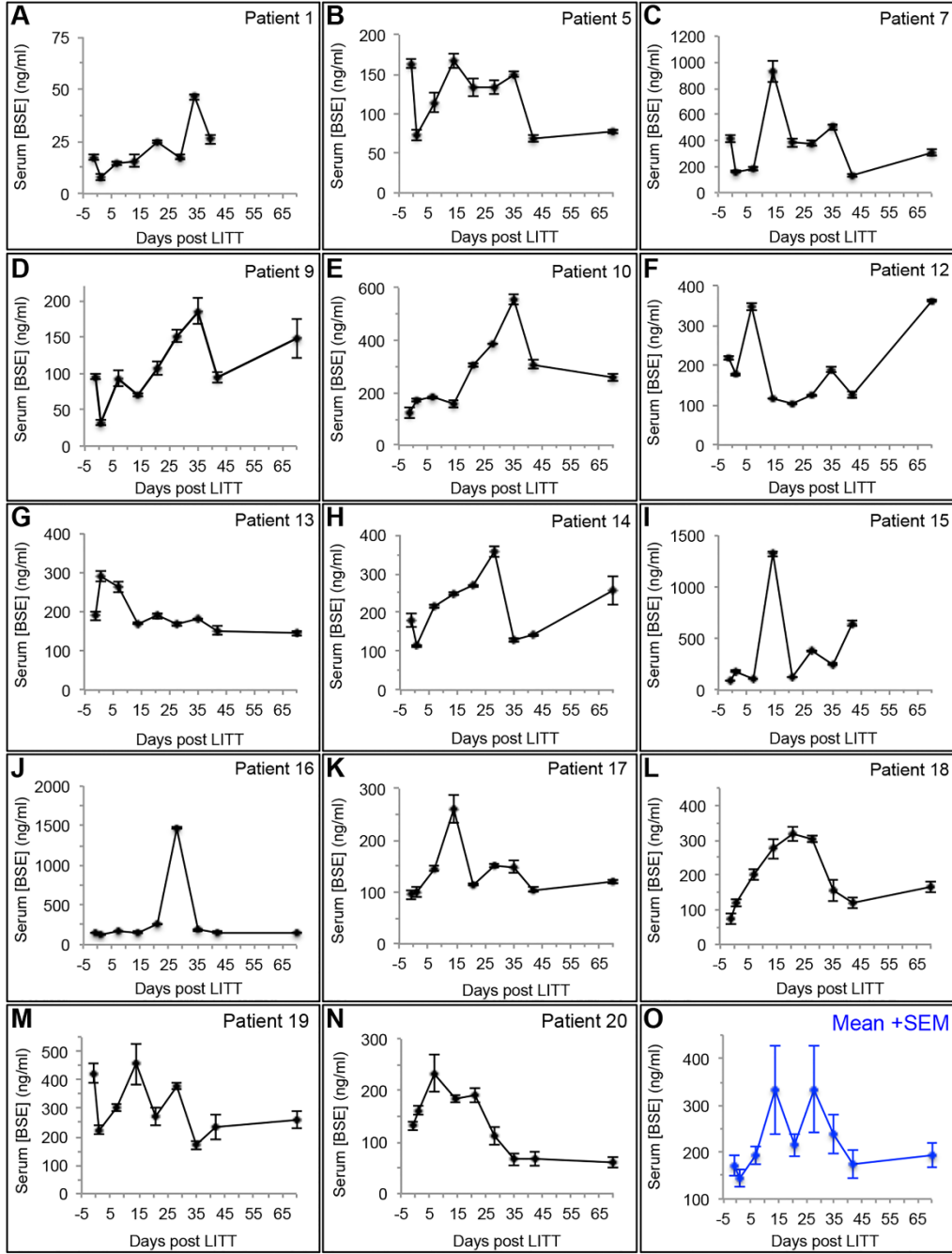


Figure A.5: BBB disruption induced by LITT as measured by serum biomarkers. Serum concentrations of BSE for each of the 14 evaluable subjects in the study (A-N) and as the mean + SEM (O) as a function of time in days from the LITT procedure. In 7/14 subjects, serum BSE levels slightly decreased immediately after LITT, then in 13/14 subjects, serum BSE levels rose shortly after LITT, peaked between 1–3 weeks after LITT, and then decreased by the 6-week time point. In Patient #12, serum BSE concentration increased at week 10 coincident with an increased K^{trans} at the same time point, consistent with a recurrent tumor as demonstrated on diagnostic MR imaging. Patient #15's serum BSE concentration began to rise by week 4, consistent with early multifocal recurrent disease as demonstrated on diagnostic MR imaging.

A.4 Discussion

LITT is a minimally invasive neurosurgical technique that achieves effective tumor cytorreduction of brain tumors using a laser to deliver hyperthermic ablation. Here we have demonstrated that an unexpected, potentially useful effect of LITT is its ability to also disrupt the BBB in the peritumoral region that extends outwards 1-2 cm from the viable tumor rim. Importantly, the disruption persists in all 14 evaluable, treated patients for up to 4 weeks after LITT as measured quantitatively by DCE-MRI and up to 6 weeks as measured by serum levels of the brain-specific factor BSE. These observations indicate that after LITT there is a window during which enhanced local delivery of therapeutic agents into the desired location (i.e. peritumoral region) can potentially be achieved.

In all of the patients in this series, the peaks of serum concentrations of BSE were delayed from several days to 1-2 weeks following the peak of BBB disruption as measured by K^{trans} . This delay could be explained by: 1) the higher data point resolution for the serum values versus DCE-MRI values (weekly versus biweekly, respectively); and 2) interval physiologic breakdown of thermally ablated tissue coupled with subsequent diffusion and equilibration between the intracranial and peripheral compartments. More importantly, both methods showed that the peritumoral BBB disruption induced by LITT was temporary, decreasing soon after peaking and being resolved by 4-6 weeks in most patients. Our present data demonstrating a dual application of LITT to achieve cytorreduction and to induce reversible disruption of the peritumoral BBB should allow for the reexamination of drugs that have not demonstrated a survival advantage in prior studies or are predicted to be ineffective in primary or metastatic brain tumors because of their poor BBB penetration despite possessing considerable anti-cancer activity in vitro and/or in extracranial tumors.

Whether the 4-6 week duration of BBB disruption after LITT is long enough to be therapeutically meaningful will need to be determined prospectively in future studies. In the case of Gliadel, direct delivery of BCNU into the resection cavity over a short period of 5 days was sufficient to result in a modest survival benefit for both recurrent and newly diagnosed GBM (13) when compared to BCNU administered systemically. Therefore the significantly longer duration of BBB disruption induced by LITT would be predicted to be adequate for enhanced drug delivery and clinical benefits when the right therapeutic agents are utilized.

In addition to the role LITT could play for enhanced local delivery of therapeutic agents, there is also the possibility that this approach could have important immunological consequences. The persistent elevation of BSE after LITT in the peripheral circulation indicates that proteins are being continually released outside the immune-privileged compartment of the CNS. With the laser ablation of the tumor, it is reasonable to assume the tumor specific proteins are also being released into systemic circulation. Whether this enhanced presentation of tumor antigens and neoantigens to the immune system could facilitate the body's tumor-specific immune response remains to be determined, but is quite an intriguing line of inquiry for future investigation.

A.5 Acknowledgements

We would like to thank our colleagues in neurosurgery, neuro-radiology, neuropathology, and medical oncology for their collaboration and helpful discussion, the clinical trial core at the Siteman Cancer Center for their support, Laura Sullivan, Abigail Gwinn, Trisha Sturgill, Ann Woodside, Madelyn Kissel, and Andrew Wegrzyn for their help in coordinating the study and

processing blood samples. We also would like to thank the staff of the Center for Clinical Imaging and Research for their dedicated acquisition of the MRI data.

A.6 References

1. Parkin DM. Global cancer statistics in the year 2000. *The Lancet Oncology*. 2001;2(9):533-543.
2. Stupp R, WP Mason, MJ van den Bent, *et al*. Radiotherapy plus Concomitant and Adjuvant Temozolomide for Glioblastoma. *New England Journal of Medicine*. 2005;352(10):987-996.
3. Stupp R, ME Hegi, WP Mason, *et al*. Effects of radiotherapy with concomitant and adjuvant temozolomide versus radiotherapy alone on survival in glioblastoma in a randomised phase III study: 5-year analysis of the EORTC-NCIC trial. *The Lancet Oncology*. 2009;10(5):459-466.
4. Hochberg FH and A Pruitt. Assumptions in the radiotherapy of glioblastoma. *Neurology*. 1980;30(9):907-911.
5. Holodny AI, AO Nusbaum, S Festa, *et al*. Correlation between the degree of contrast enhancement and the volume of peritumoral edema in meningiomas and malignant gliomas. *Neuroradiology*. 1999;41(11):820-825.
6. Kassner A and R Thornhill. Measuring the integrity of the human blood-brain barrier using magnetic resonance imaging. *Methods Mol Biol*. 2011;686:229-245.
7. Deeken JF and W L Jätscher. The Blood-Brain Barrier and Cancer: Transporters, Treatment, and Trojan Horses. *Clinical Cancer Research*. 2007;13(6):1663-1674.
8. Stewart DJ, MT Richard, H Hugenholtz, *et al*. Penetration of VP-16 (etoposide) into human intracerebral and extracerebral tumors. *J Neurooncol*. 1984;2(2):133-139.
9. Stewart DJ, K Lu, RS Benjamin, *et al*. Concentration of vinblastine in human intracerebral tumor and other tissues. *J Neurooncol*. 1983;1(2):139-144.
10. Brem H, S Piantadosi, PC Burger, *et al*. Placebo-controlled trial of safety and efficacy of intraoperative controlled delivery by biodegradable polymers of chemotherapy for recurrent gliomas. The Polymer-brain Tumor Treatment Group. *Lancet*. 1995;345(8956):1008-1012.
11. Westphal M, Z Ram, V Riddle, *et al*. Gliadel wafer in initial surgery for malignant glioma: long-term follow-up of a multicenter controlled trial. *Acta Neurochir (Wien)*. 2006;148(3):269-275; discussion 275.
12. Westphal M, DC Hilt, E Bortey, *et al*. A phase 3 trial of local chemotherapy with biodegradable carmustine (BCNU) wafers (Gliadel wafers) in patients with primary malignant glioma. *Neuro-oncology*. 2003;5(2):79-88.

13. Fleming AB and WM Saltzman. Pharmacokinetics of the carmustine implant. *Clin Pharmacokinet.* 2002;41(6):403-419.
14. Bobo RH, DW Laske, A Akbasak, *et al.* Convection-enhanced delivery of macromolecules in the brain. *Proceedings of the National Academy of Sciences.* 1994;91(6):2076-2080.
15. Gong W, Z Wang, N Liu, *et al.* Improving efficiency of adriamycin crossing blood brain barrier by combination of thermosensitive liposomes and hyperthermia. *Biol Pharm Bull.* 2011;34(7):1058-1064.
16. Oztas B and M Kucuk. Reversible blood-brain barrier dysfunction after intracarotid hyperthermic saline infusion. *Int J Hyperthermia.* 1998;14(4):395-401.
17. Sabel M, F Rommel, M Kondakci, *et al.* Locoregional opening of the rodent blood-brain barrier for paclitaxel using Nd:YAG laser-induced thermo therapy: a new concept of adjuvant glioma therapy? *Lasers Surg Med.* 2003;33(2):75-80.
18. Kangasniemi M, RJ McNichols, JA Bankson, *et al.* Thermal therapy of canine cerebral tumors using a 980 nm diode laser with MR temperature-sensitive imaging feedback. *Lasers Surg Med.* 2004;35(1):41-50.
19. Reimer P, C Bremer, C Horch, *et al.* MR-monitored LITT as a palliative concept in patients with high grade gliomas: preliminary clinical experience. *J Magn Reson Imaging.* 1998;8(1):240-244.
20. Schulze PC, T Kahn, T Harth, *et al.* Correlation of neuropathologic findings and phase-based MRI temperature maps in experimental laser-induced interstitial thermotherapy. *J Magn Reson Imaging.* 1998;8(1):115-120.
21. Schwabe B, T Kahn, T Harth, *et al.* Laser-induced thermal lesions in the human brain: short- and long-term appearance on MRI. *J Comput Assist Tomogr.* 1997;21(5):818-825.
22. Kangasniemi M, RJ Stafford, RE Price, *et al.* Dynamic gadolinium uptake in thermally treated canine brain tissue and experimental cerebral tumors. *Invest Radiol.* 2003;38(2):102-107.
23. Hawasli AH, AH Kim, GP Dunn, *et al.* Stereotactic laser ablation of high-grade gliomas. *Neurosurg Focus.* 2014;37(6):E1.
24. Mohammadi AM, AH Hawasli, A Rodriguez, *et al.* The role of laser interstitial thermal therapy in enhancing progression-free survival of difficult-to-access high-grade gliomas: a multicenter study. *Cancer Med.* 2014;3(4):971-979.
25. Hawasli AH, S Bagade, JS Shimony, *et al.* Magnetic resonance imaging-guided focused laser interstitial thermal therapy for intracranial lesions: single-institution series. *Neurosurgery.* 2013;73(6):1007-1017.

26. Hawasli AH, WZ Ray, RK Murphy, *et al.* Magnetic resonance imaging-guided focused laser interstitial thermal therapy for subinsular metastatic adenocarcinoma: technical case report. *Neurosurgery*. 2012;70(2 Suppl Operative):332-337; discussion 338.
27. Tofts PS, G Brix, DL Buckley, *et al.* Estimating kinetic parameters from dynamic contrast-enhanced T(1)-weighted MRI of a diffusable tracer: standardized quantities and symbols. *J Magn Reson Imaging*. 1999;10(3):223-232.
28. Leach MO, B Morgan, PS Tofts, *et al.* Imaging vascular function for early stage clinical trials using dynamic contrast-enhanced magnetic resonance imaging. *Eur Radiol*. 2012;22(7):1451-1464.
29. Kallehauge J, T Nielsen, S Haack, *et al.* Voxelwise comparison of perfusion parameters estimated using dynamic contrast enhanced (DCE) computed tomography and DCE-magnetic resonance imaging in locally advanced cervical cancer. *Acta Oncol*. 2013;52(7):1360-1368.
30. Donaldson SB, CM West, SE Davidson, *et al.* A comparison of tracer kinetic models for T1-weighted dynamic contrast-enhanced MRI: application in carcinoma of the cervix. *Magn Reson Med*. 2010;63(3):691-700.
31. Lee JJ, G Xuemin and L Suyu. Bayesian adaptive randomization designs for targeted agent development. *Clin Trials*. 2010;7(5):584-596.
32. Correale J, AL Rabinowicz, CN Heck, *et al.* Status epilepticus increases CSF levels of neuron-specific enolase and alters the blood-brain barrier. *Neurology*. 1998;50(5):1388-1391.
33. Marchi N, P Rasmussen, M Kapural, *et al.* Peripheral markers of brain damage and blood-brain barrier dysfunction. *Restor Neurol Neurosci*. 2003;21(3-4):109-121.
34. Stalnacke BM, Y Tegner and P Sojka. Playing soccer increases serum concentrations of the biochemical markers of brain damage S-100B and neuron-specific enolase in elite players: a pilot study. *Brain Inj*. 2004;18(9):899-909

Appendix B: Effects of Off-Resonance on T_1 Saturation Recovery Measurement in inhomogeneous field¹

B.1 Introduction

Nuclear magnetic resonance (NMR) relaxometry is being increasingly applied for measurements in grossly inhomogeneous field. In these applications (1, 2), it is either impossible or undesirable to insert the samples into a highly homogeneous superconducting magnetic field. One such application is oil-well logging where the sample is the earth formation. Unlike other conventional NMR spectroscopy and imaging techniques, relaxometry requires minimal static and radio frequency (RF) field homogeneity, which enables its broad applications in single-sided or other "inside-out" NMR measurements where the static magnetic field is necessarily inhomogeneous.

Carr-Purcell-Meiboom-Gill (CPMG) sequences (3-4) have found broad applications in oil-well logging (5-7). In particular T_2 based distribution measurements are widely used for estimating the distribution of pore sizes in porous media (8). To resolve multiple components, it is useful to perform two-dimensional measurements to measure correlations between different NMR properties, including $T_1 - T_2$ (9) and $D - T_2$ (10) distribution functions. There has been recently much interest in detecting contrast between T_1 and T_2 relaxation that arises in shale samples with low frequency molecular motion (11-14).

¹ All contents in this chapter have been published in Duan C, Ryan C, Utsuzawa S, Song Y-Q, and Hurlimann MD. Effect of Off-Resonance on T_1 Saturation Recovery Measurement in inhomogeneous field. *J Magn Reson* (2017); 281: 31-43.

A common method to measure T_1 and T_1 - T_2 distribution functions in inhomogeneous fields is to employ a saturation - recovery pulse sequence based on CPMG sequences. A typical implementation consists of a series of CPMG sequences that are run consecutively with a variable wait time, T_w , as shown in Fig. 1. In this case, both saturation and detection is achieved with CPMG sequences. The longitudinal magnetization, M_z , is eliminated by the initial $\pi/2$ pulse of the first CPMG sequence, and the subsequent π pulses prevent any recovery until the end of this sequence. M_z then recovers from $M_z = 0$ towards the thermal equilibrium M_0 during the wait time with the time constant T_1 . The measured amplitude of the second (detecting) CPMG sequence after the wait time T_w is then proportional to $1 - e^{-T_w/T_1}$.

This approach implicitly assumes that the static magnetic field B_0 and the RF field B_1 are homogeneous across the sample, so that $M_z = 0$ at the end of the CPMG sequence. However, in single-sided NMR measurements, the static magnetic field B_0 is grossly inhomogeneous, and the assumption regarding full saturation by the initial nominal $\pi/2$ pulse and the subsequent refocusing pulses is not valid any more.

In the present study, we analyze the relevant spin dynamics in grossly in-homogeneous field and show that it is still possible to perform quantitative T_1 measurements. We derive a generalized T_1 kernel for saturation-recovery measurements with CPMG detection and saturation that is valid in homogeneous field and takes full account of the off-resonance effects. The analytical results are validated by numerical simulations and experiments. This analysis complements the previous analysis of T_1 inversion-recovery measurements in inhomogeneous fields (15).

B.2 Theory

B.2.1 Spin Dynamics in homogeneous field

For a collection of uncoupled spins 1/2, the dynamics for the magnetization in the rotating frame is governed by the Bloch Equations:

$$\frac{dM_x(\vec{r}, t)}{dt} = -\omega_0(\vec{r})M_y(\vec{r}, t) + \omega_1(\vec{r}, t) \sin \phi(\vec{r}, t)M_z(\vec{r}, t) - \frac{1}{T_2}M_x(\vec{r}, t) \quad [1]$$

$$\frac{dM_y(\vec{r}, t)}{dt} = +\omega_0(\vec{r})M_x(\vec{r}, t) - \omega_1(\vec{r}, t) \cos \phi(\vec{r}, t)M_z(\vec{r}, t) - \frac{1}{T_2}M_y(\vec{r}, t) \quad [2]$$

$$\begin{aligned} \frac{dM_z(\vec{r}, t)}{dt} = & -\omega_1(\vec{r}, t) \sin \phi(\vec{r}, t)M_x(\vec{r}, t) + \omega_1(\vec{r}, t) \cos \phi(\vec{r}, t)M_y(\vec{r}, t) \\ & - \frac{1}{T_1}(M_z(\vec{r}, t) - M_0) \end{aligned} \quad [3]$$

Here $\omega_0 \equiv \gamma|B_0| - \omega_{RF}$ is the offset between the local Larmor frequency and the RF frequency, $\omega_1 \equiv \frac{1}{2}\gamma|B_1|$ is the local nutation frequency, and ϕ is the phase of the RF pulses in the rotating frame, and M_0 is the thermal equilibrium magnetization.

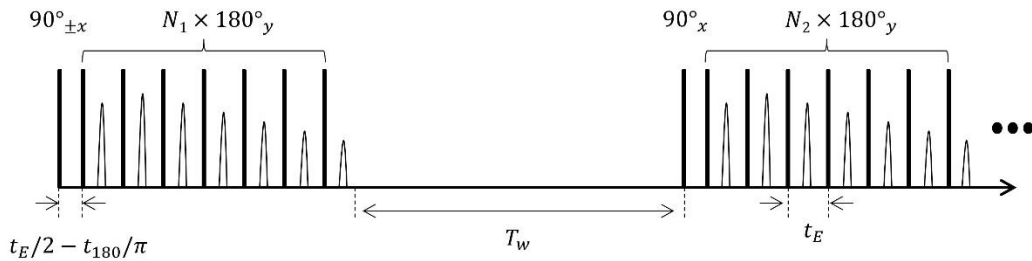


Figure B.1: Saturation – recovery pulse sequence considered in this study. CPMG sequences are employed for both saturation and detection. Here T_w is the saturation recovery wait time, t_E is echo spacing, t_{90} and t_{180} are the duration of nominal 90° and 180° pulses, respectively, and N_1 and N_2 are the number of refocusing pulses in the two CPMG sequences. The phase of all

refocusing pulses are set to +y and the phase of the excitation pulse of the second (detecting) CPMG sequence is set to +x. The phase of the excitation pulse of the first (saturating) CPMG sequence is set either to +x to -x. We assume that t_E is short enough to eliminate diffusion effects.

We are interested in the solution for the pulse sequence shown in *Figure B.1* for arbitrary values of ω_0 . The first CPMG sequence can be considered as the saturation sequence. For 90° and 180° CPMG pulses that are perfect and on-resonance, the evolution of the magnetization can be easily obtained. During the main CPMG sequence, the transverse magnetization decays according to $M_\perp(t) = M_0 \times e^{-t/T_2}$, and the longitudinal magnetization M_z oscillates between $\pm M_\perp(t) = M_0 \times \left(1 - e^{-\frac{t_E}{2T_1}}\right)$. At the nominal echo center at the end of the CPMG, $M_z = 0$. After the CPMG sequence and during the wait time, the M_z recovers towards the thermal magnetization M_0 with time constant T_1 :

$$M_z(T_w)/M_0 = 1 - e^{-T_w/T_1} \quad [4]$$

The initial amplitude of the second (detecting) CPMG sequence is then directly proportional to $M_z(T_w)$ and therefore Eq. 4 can be used as the kernel to extract T_1 from the NMR measurements.

To assure that this conventional T_1 kernel (Eq. 4) to be valid, the longitudinal magnetization at the beginning of the wait time has to be zero for all spin packets. This assumption is only valid for perfect pulses that are on resonance. In single-sided NMR, the fields are necessarily inhomogeneous and off-resonance effects become significant. This results in deviations from the standard kernel, Eq. 4, and will lead to faulty T_1 values. The pulse sequence under consideration is shown in *Figure B.1*. The first CPMG represents the saturation sequence.

B.2.2 Spin Dynamics in inhomogeneous field

Single CPMG sequence

In grossly inhomogeneous fields, all RF pulses are slice selective and the response is non-uniform across the sample. The resulting spin dynamics of multi-pulse sequences becomes complicated (6-7), but in the fast pulsing regime, i.e., $t_E \ll T_2$, analytical results are available that describe the response of a single CPMG sequence as a function of ω_0 and ω_1 (7). The key quantities controlling the spin dynamics are $\vec{m}_{exc}(\omega_0)$ and $\{\hat{n}(\omega_0), \theta(\omega_0)\}$ that characterize the initial 90° excitation pulse and the refocusing cycle, respectively. Here $\vec{m}_{exc}(\omega_0)$ is the magnetization resulting from the excitation pulse applied to an initial magnetization of unit amplitude along \hat{z} , while \hat{n} and θ are the axis and rotation angle of the effective rotation describing the repeated refocusing cycle.

Saturation – Recovery Sequence with CPMG saturation and CPMG detection

We next extend the results for a single CPMG sequence to that of the sequence shown in Figure B.1. The echoes generated by the second (detecting) CPMG in a gradient field have an asymptotic spectrum (7) that is proportional to the longitudinal magnetization $M_z(T_w; \omega_0)$ at the end of the wait time:

$$M_{asy}(T_w; \omega_0) = M_z(T_w; \omega_0) [\vec{m}_{exc,2}(\omega_0) \cdot \hat{n}(\omega_0)] \vec{n}_\perp(\omega_0) \quad [5]$$

Here the subscript 2 indicates that \vec{m}_{exc} refers to the excitation pulse of the second CPMG. We have made the implicit assumption that any transverse magnetization prior to the start of the second CPMG has completely dephased. Furthermore, we assumed that there is a uniform density of offset frequencies ω_0 across the sample, i.e. $f_{magnet}(\omega_0) = \text{constant}$. This is the case for an extended sample in a gradient B_0 field. When the magnetic field is not a simple gradient field and / or when

the sample does not extend across the entire field variation, Eq. 5 can be generalized by multiplying it by the actual density of offset frequency, $f_{magnet}(\omega_0)$.

As M_z recovers during T_w , its spectrum of $M_z(T_w, \omega_0)$ changes with time. At short values of T_w , the spectrum reflects the non-uniform M_z saturation generated by the first CPMG sequence, while at very long times, it becomes uniform and equal to M_0 . This implies that the echo shape of the detecting CPMG (i.e. Fourier transform of Eq. 5) varies with T_w . As a consequence, it is necessary to specify the windowing function or detection filter used to extract the echo amplitudes from the measured echoes. Common approaches include peak detection, integration of the echoes over a specified acquisition window, or matched filtering with the expected echo shape. In all cases, this procedure can be described by an effective acquisition filter $f_{acq}(\omega_0)$, such that the echo amplitude is given by:

$$A(T_w) = \int d\omega_0 M_{asy}(T_w; \omega_0) f_{acq}(\omega_0) \quad [6]$$

In the case of echo peak detection, $f_{acq}^{peak}(\omega_0) = \frac{\sin(\omega_0 T_{DW}/2)}{\omega_0 T_{DW}/2}$, where T_{DW} is the dwell time. In the case of matched filtering where the measured echoes are weighted by the expected asymptotic echo shape for a single CPMG on a sample at thermal equilibrium,

$$f_{acq}^{(match)}(\omega_0) = [\vec{m}_{exc,2}(\omega_0) \cdot \hat{n}(\omega_0)] \vec{n}_\perp(\omega_0) * \frac{\sin(\omega_0 T_{acq}/2)}{\omega_0 T_{acq}/2} \quad [7]$$

Here T_{acq} is the total acquisition time and $*$ denotes the convolution operation. Matched filtering optimizes the signal-to-noise-ratio of the extracted amplitudes in the presence of random white noise.

It is useful to introduce the effective weighting function $g(\omega_0)$ given by:

$$g(\omega_0) = [\vec{m}_{exc,2}(\omega_0) \cdot \hat{n}(\omega_0)] \vec{n}_\perp(\omega_0) f_{acq}(\omega_0) \quad [8]$$

With this notation, $A(T_w)$ can be written as the weighted integral of the longitudinal magnetization $M_z(T_w; \omega_0)$ and the effective weighting function $g(\omega_0)$:

$$A(T_w) = \int d\omega_0 M_z(T_w; \omega_0) g(\omega_0) \quad [9]$$

The weighting functions $g(\omega_0)$ can be evaluated with the equations given in Hurlimann et al. (7), and are shown for matched filtering and peak detection in Figure B.2. Unless otherwise noted, matched filtering is used in the rest of this paper.

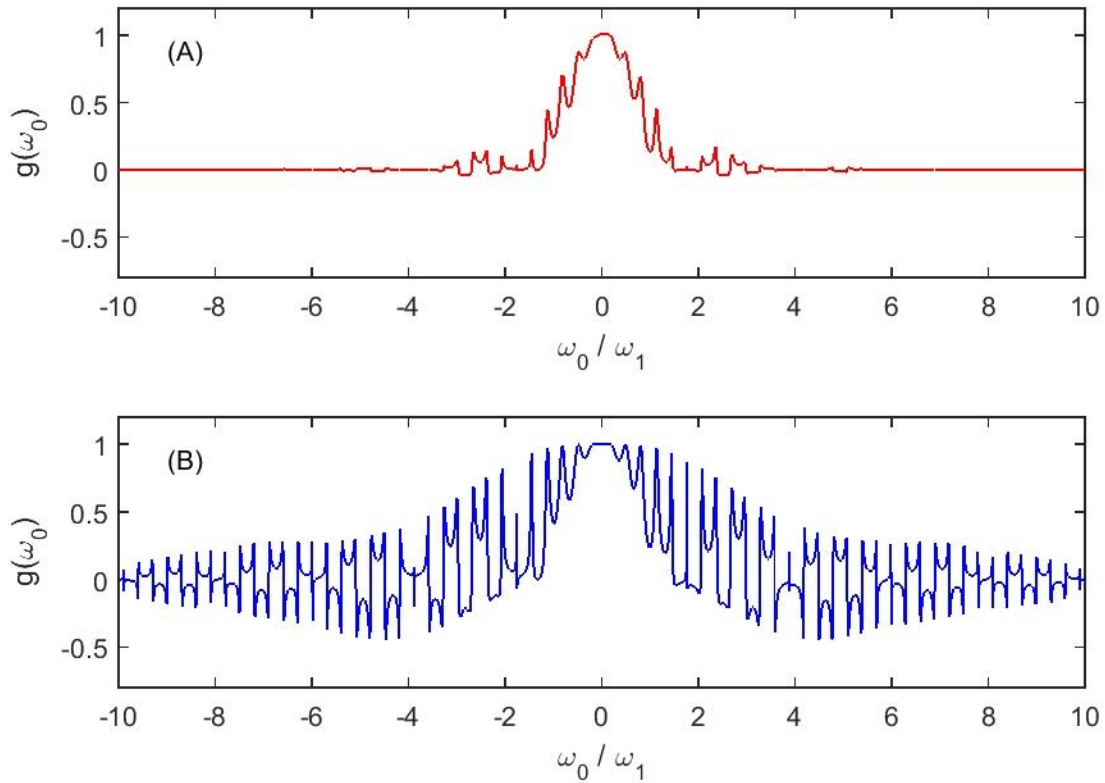


Figure B.2: Effective weighting function $g(\omega_0)$ given in Eq.[8] for two different choices of amplitude extraction: (A) matched filter and (B) peak detection. In the matched filter approach shown in (A), it was assumed that the total acquisition time $T_{acq} = 4t_{180}$, while for the peak detection, it was assumed that the dwell time $T_{DW} = t_{180}/20$.

General T_1 Kernel

In order to derive a generalized T_1 kernel, we relate the longitudinal magnetization at the end of T_w , $M_z(T_w; \omega_0)$ (or equivalently at the beginning of the second CPMG sequence) to the longitudinal magnetization at the beginning of T_w , $M_z(T_w = 0; \omega_0)$ (or equivalently at the end of the first CPMG sequence). According to Bloch's Equation, they are related by:

$$\frac{M_z(T_w; \omega_0)}{M_0} = \left(1 - e^{-\frac{T_w}{T_1}}\right) + \frac{M_z(T_w = 0; \omega_0)}{M_0} e^{-\frac{T_w}{T_1}} \quad [10]$$

Combining Eqs. [9] and [10] results in the modified form of the generalized T_1 kernel in inhomogeneous fields:

$$\frac{A(T_w)}{A_0} = 1 - (1 - \epsilon) e^{-\frac{T_w}{T_1}} \quad [11]$$

Where the offset parameter ϵ is given by:

$$\epsilon \equiv \int d\omega_0 \frac{M_z(T_w = 0; \omega_0)}{M_0} g(\omega_0) \quad [12]$$

The generalized T_1 kernel differs from the standard T_1 kernel by the offset term ϵ . This dimensionless parameter is the weighted integral of $M_z(T_w = 0; \omega_0)$, the longitudinal magnetization at the end of the initial CPMG sequence, with the weighting function $g(\omega_0)$. It is not a fixed constant, but depends on the experimental parameters and relaxation properties, in

particular on the normalized length of the first CPMG sequence, $N_I t_E = T_2$, and on the T_1/T_2 ratio. Here N_I is the number of echoes during the first CPMG sequence and t_E is the echo spacing.

Offset parameter ε for $T_1 = T_2$

The dependence of ε on the normalized duration of the CPMG sequence and the T_1/T_2 ratio can be inferred from the analysis of $M_z(T_w = 0; \omega_0)$, the longitudinal magnetization at the end of the first CPMG sequence. For $T_1 = T_2$, we obtain:

$$\varepsilon = \alpha_1 e^{-\frac{N_I t_E}{T_2}} + \alpha_2 (1 - e^{-\frac{N_I t_E}{T_2}}) \quad [13]$$

Where

$$\alpha_1 = \int d\omega_0 [\vec{m}_{exc,1}(\omega_0) \cdot \hat{n}(\omega_0)] n_z(\omega_0) g(\omega_0) \quad [14]$$

$$\alpha_2 = \int d\omega_0 n_z^2 g(\omega_0) \quad [15]$$

The dimensionless parameters α_1 and α_2 are constants for a given experimental configuration and do not depend on the relaxation properties of the sample. The term α_1 originates from the CPMG coherence pathway, whereas α_2 is due to the dynamic equilibrium term that builds up as the CPMG term decays. In principle, there is also a term due to the CP contribution. However, this term can be ignored. The longitudinal magnetization from this term fluctuates rapidly on a frequency scale much faster than the typical variations of $g(\omega_0)$ so that it does not contribute to the integral in Eq. 12 and averages out to zero.

Offset parameter ε for General T_1 / T_2 ratio

For $T_1 \neq T_2$, the expression for ε has a similar form as Eq. 13, but the coefficient α_2 has to be replaced by:

$$\int d\omega_0 \frac{n_z^2}{n_z^2 + (1 - n_z^2) \frac{T_1}{T_2}} g(\omega_0) \approx \frac{\alpha_2}{\eta + (1 - \eta) \frac{T_1}{T_2}} \quad [16]$$

This expression can be viewed as the definition of the dimensionless parameter η . In addition, for $T_1 \neq T_2$ the relaxation time T_2 in Eq. 13 should be replaced by T_{eff} , as given in Hurlimann et al. (7). Since this generalization typically results only in a small correction, we will ignore this effect in the rest of the paper. With these approximations, the general expression for the T_1 kernel has the form of Eq. 11, where ε is given by:

$$\epsilon = \alpha_1 e^{-\frac{N_1 t_E}{T_2}} + \frac{\alpha_2}{\eta + (1 - \eta) \frac{T_1}{T_2}} (1 - e^{-\frac{N_1 t_E}{T_2}}) \quad [16]$$

The three parameters α_1, α_2 , and η are given by Eqs. (14), (15), and (16), respectively and are independent of the relaxation properties of the sample. They depend on the characteristics of the experimental set-up, including the field configuration, data filtering, and choice of pulse phases. At the outset of the measurements, they have to be determined for the specific experimental setup used. It is desirable to make these parameters as small as possible. Possible strategies are discussed below.

B.3 Numerical Procedures

To check the theoretical analysis, we also performed a direct numerical simulation of the spin dynamics. We developed a scalable fast C++ code based on the integration of the Bloch Equations [1-3] for \vec{B}_0, \vec{B}_1 fields that are inhomogeneous and possibly time-dependent. Here we simulate the

Bloch vector dynamics over an array of voxels with a static \vec{B}_0 field and a pulsed \vec{B}_1 field. The calculations account for the effects of the RF pulses, precession in the inhomogeneous fields, T1 and T2 relaxation during the delay periods and optionally during pulses. The basic simulation steps are for each voxel:

1. Define a tilted and rotating frame, where the z-axis is pointing along the local direction of \vec{B}_0 , and the x-axis along $\vec{B}_{1,\perp}$ (where $\vec{B}_{1,\perp}$ is the component of \vec{B}_1 perpendicular to \vec{B}_0).
2. Determine the local values of the offset frequency $\omega_0 \equiv \gamma|B_0| - \omega_{RF}$ and $\omega_1 \equiv \frac{1}{2}\gamma|B_{1,\perp}|$.
3. Project the initial state into the tilted and rotating frame defined by \vec{B}_0 and $\vec{B}_{1,\perp}$.
4. For each time-step, propagate the Bloch vector within the tilted and rotating frame as either a delay (\hat{z} rotation followed by T_1 and T_2 relaxation) or a pulse (rotation about an axis determined by ω_0 , ω_1 and the pulse phase).

The detected magnetization M_z corresponds to the sum of the transverse components $M_x + iM_y$ over all voxels. To calculate the echo shapes, we also store the array of ω_0 values and perform a Fourier transformation.

Simulations were performed on a Dell Precision T7600 workstation equipped with two Intel Xeon E5-2667 processors (6 cores each, 2.9GHz), 256 GB physical memory (RAM), and running Microsoft Windows 8 Enterprise edition. In the presented results, we assumed a sample in a constant gradient \vec{B}_0 field extending over $\Delta\vec{B}_0 = \pm 10\vec{B}_{1,\perp}$, corresponding to $\omega_0 \in [-5\omega_1, +5\omega_1]$ and a uniform RF field \vec{B}_1 . Relaxation during the RF pulses was neglected. The asymptotic echo amplitudes were generally calculated assuming detection using the optimal matched filter defined by the asymptotic echo shape, unless otherwise noted. No additional receiver filter was applied to

the simulated echoes (i.e., the signal bandwidth is only limited by excitation). All calculated echo amplitudes are normalized with respect to the asymptotic echo signal amplitude of the initial CPMG signal when the wait time is long (i.e., fully recovered). The initial echo amplitude for a CPMG detection was calculated by extrapolating the echo train amplitudes (ignoring the first few echoes due to the transient effect (9)), and was then treated as the signal for the T_1 saturation

Experimental Procedures

B.4 Experimental procedure

To verify the theoretical and numerical analyses for saturation recovery in grossly inhomogeneous field, we performed saturation - recovery T_1 measurements with the sequence of Figure B.1 on ^1H with three samples: Deionized (DI) H_2O , NiCl_2 -doped H_2O , and skim milk. The cylindrical samples of 1-cm diameter and 24-cm length were placed in the center of a superconducting 1T horizontal-bore magnet. The T_1 and T_2 for all of three samples were measured first employing standard inversion recovery and CPMG pulse sequences. To generate the off-resonant effect, a static gradient of 8.6 kHz/cm was applied along the B_0 direction (i.e., horizontally). Effects of RF inhomogeneities were minimized by using a comparatively large RF solenoid coil ($Q \approx 104$) of 4-cm diameter and 8-cm length. For this setup, similar to the simulation, the signal bandwidth is limited by the excitation.

In our experimental setup, the variation in the off-resonance frequencies $\omega_0/2\pi$ across the sample span ± 34.4 kHz, which is significantly larger than the RF field strength $\omega_1/2\pi = 2.5$ kHz. Therefore, the echoes are well separated in time and have a width of the order of $2 \times t_{180}$. Following Hurlimann (16), the pulse spacing between the 90° pulse and the first 180° refocusing pulse was reduced from half the echo spacing by t_{180} / π to maximize the signal. Durations of the 90° and

180° pulses were typically 100 and 200 μs , respectively, and the echo spacing was $t_E = 1.2$ ms. Similar to the numerical analysis, we used a matched filter defined by the asymptotic echo shape to extract echo amplitudes from the measured NMR signals.

B.5 Results

B.5.1 Numerical and Analytical Results

M_z at the end of first CPMG

We first present results for the case when $T_1 = T_2$. Figure B.3 shows the simulated longitudinal magnetization spectra, $M_z(T_w = 0; \omega_0)$, at the end of the first CPMG sequence for different values of $N_{1t_E} = T_2$. It is clear that saturation is incomplete across the sample. The standard assumption $M_z(T_w = 0) = 0$ at the end of the first CPMG sequence (and the beginning of the wait time) is only valid near $\omega_0 = 0$ (i.e. on resonance). Away from resonance, M_z shows a complicated dependence on ω_0 and the CPMG duration. The spectra exhibit structure in frequency with characteristic scales of ω_1 and $2\pi / t_E$ ($= \omega_1/3$ in the current simulations). For short CPMG durations $N_{1t_E} / T_2 < 1$, the spectra show in addition fine oscillations. They are caused by the contributions of the CP term that exhibits structure at $2\pi = N_{1t_E}$. As the length of the CPMG sequence increases and the dynamic equilibrium regime is approached, the negative components and the fast oscillations of M_z vanish and the spectrum becomes symmetric with respect to ω_0 . This is confirmed by the results shown in *Figure B.4* that displays the individual contributions from the three terms given by the analytical solutions. The bottom row of *Figure B.4* shows the sum of the three contributions, which is in excellent agreement with the results shown in *Figure B.3* obtained by the numerical simulation. This agreement strongly supports the validity of the numerical procedure and the analytical solution.

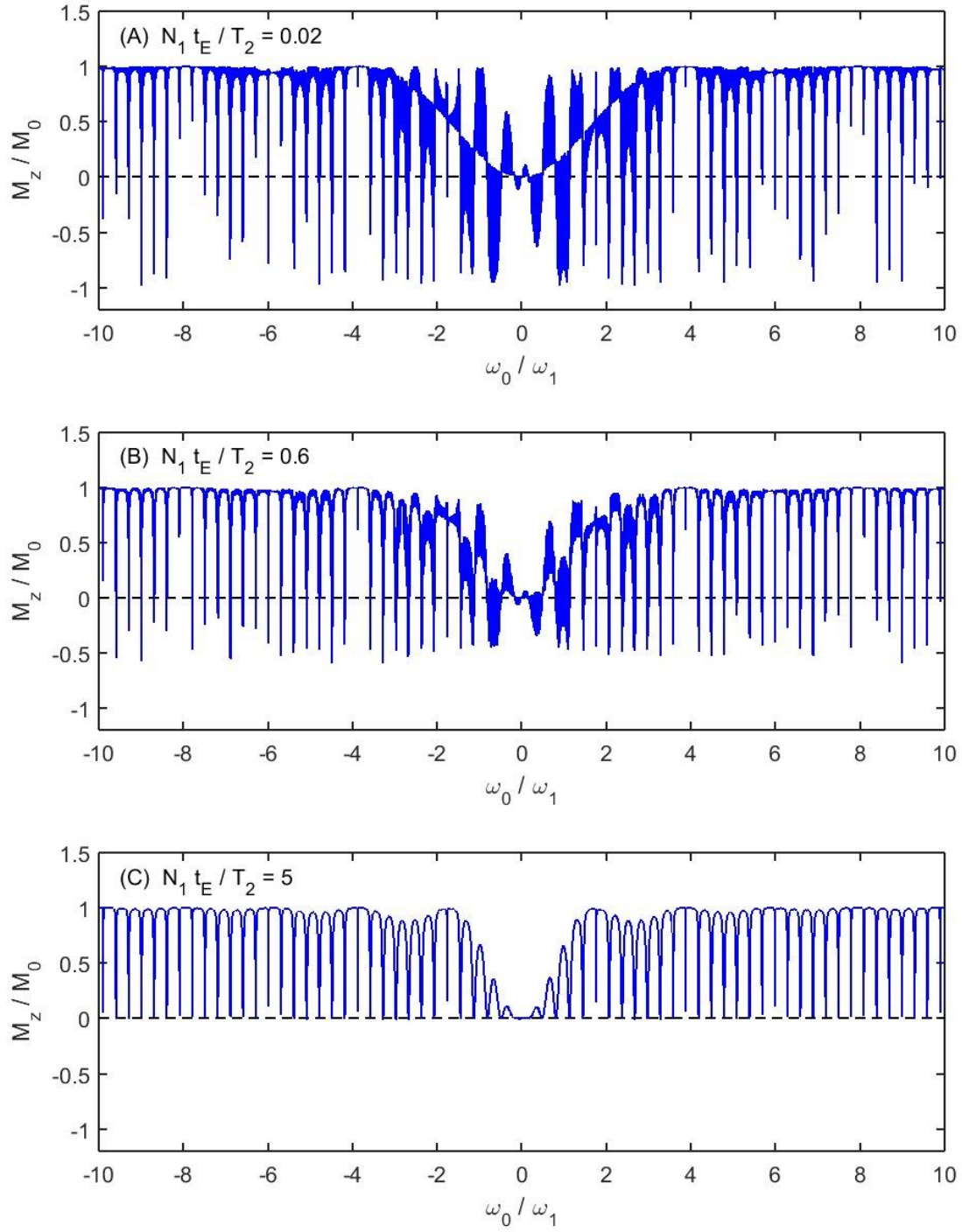


Figure B.3: Simulated spectra of longitudinal magnetization, M_z , at the end of the first CPMG sequence, normalized by the thermal magnetization M_0 for different normalized durations of the first CPMG sequence, $N_1 t_E / T_2$ as indicated. In all cases, $T_1 = T_2$. The x-axis is ω_0 / ω_1 , where ω_0 is the difference between the local Larmor frequency B_0 and the operating frequency ω_{RF} , and ω_1 is the nominal nutation frequency B_1 that is proportional to the RF amplitude. For the case of a gradient B_0 field, we can interpret the spectra as the z-magnetization across the sample.

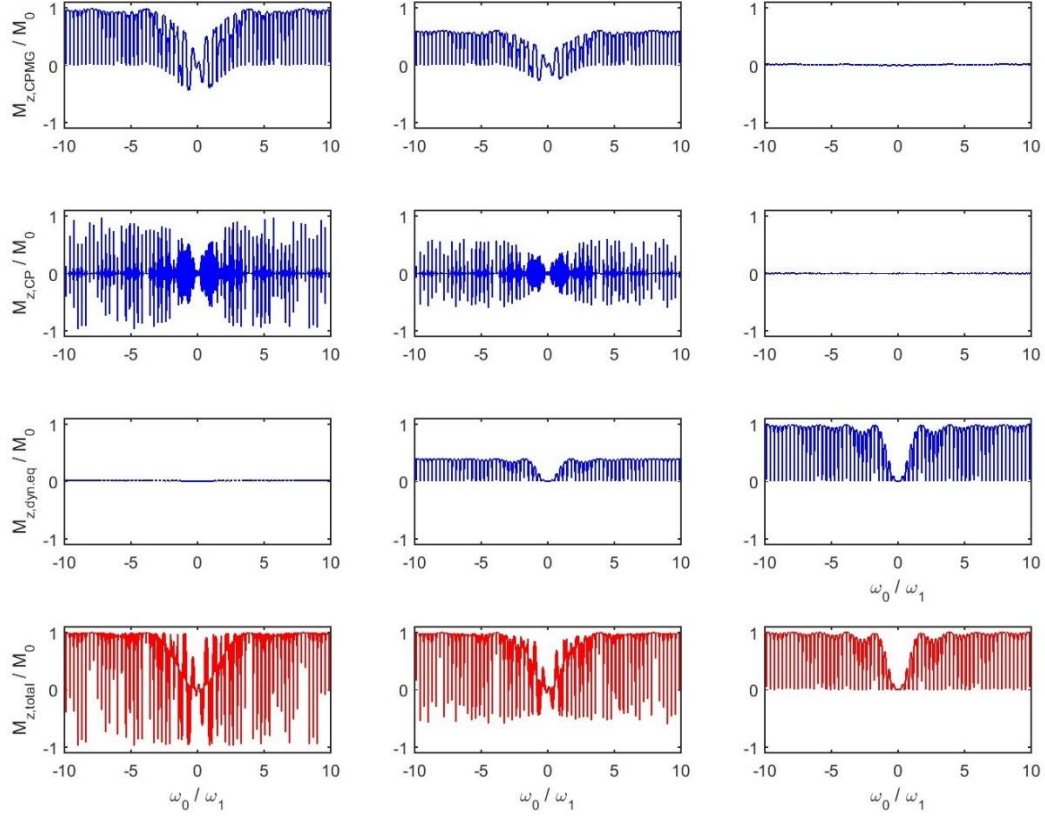


Figure B.4: Spectra of longitudinal magnetization, M_z , at the end of the first CPMG sequence, calculated from the analytical expression. From top to bottom, the different rows shows the contributions from the CPMG term, CP term, and dynamic equilibrium term, followed by the sum of all three terms. The different columns correspond to normalized durations of the first CPMG sequence, $N_{1T_E} = T_2$ of 0.02, 0.6, and 5, respectively. In all cases, $T_1 = T_2$.

Asymptotic echoes of the second CPMG

Given the M_z spectra at the end of the first CPMG sequence, the longitudinal magnetization then relaxes toward the thermal equilibrium M_0 during the subsequent wait time of duration T_w . This is followed by the second (detecting) CPMG that generates transverse magnetization and corresponding echoes. The simulated results of the asymptotic echoes are shown in the left column of Figure B.5. As T_w is varied, the overall height and also the shape of the echoes change. As expected, the results also depend on the normalized length of the saturating CPMG sequence, N_{1T_E}

$= T_2$. In the right column, the extracted amplitudes are plotted versus $1 - e^{-\frac{T_w}{T_1}}$, the nominal kernel for on-resonance behavior. We compare results for amplitudes extracted by two different methods: by matched filtering and by peak detection.

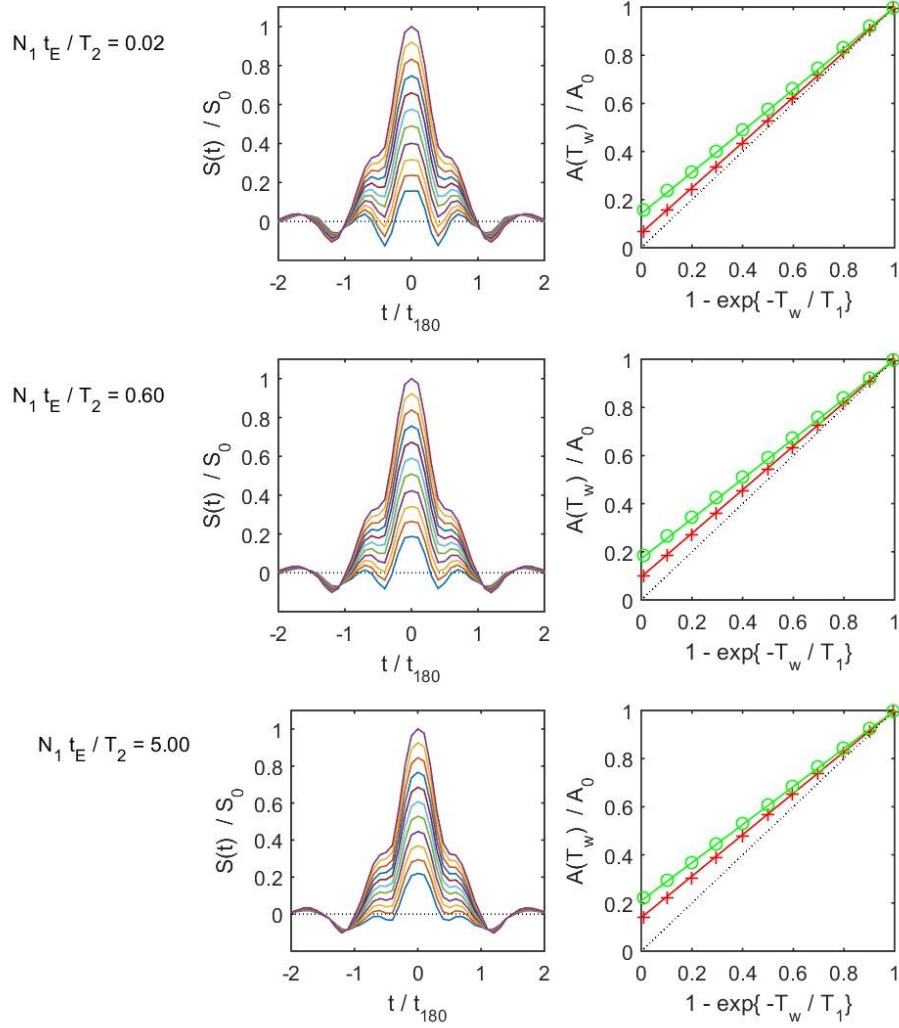


Figure B.5: Echo shapes and amplitudes as a function of $T_w = T_1$, $N_1 t_E = T_2$, and method of amplitude extraction. Left column: Simulated asymptotic echo shapes in the time domain of the second CPMG sequence for different values of the $T_w = T_1$ ratio between 0.01 to 5.00. The different rows correspond to different durations of the first CPMG sequence, $N_1 t_E = T_2$, as listed on the left. Right column: the symbols show the amplitudes extracted from the echoes displayed on the left, using two different methods of amplitude extraction. Green circles: peak detection; red cross: matched filtering using the echo shape for initial thermal equilibrium (corresponding to $T_w/T_1 \gg 1$). The solid lines show the predictions of Eq. 11 with values of ε determined by Eq. 13 with the

values of α_1 and α_2 listed in Table B.1. The green line corresponds to peak detection, while the red line corresponds to matched filtering.

Table B.1: Calculated values of α_1 and α_2 based on Eqs.14 and 15 for two methods of amplitude extraction

Method of Amplitude Extraction	α_1	α_2
Matched Filter	0.06	0.14
Peak Detection	0.14	0.21

In all cases, the results show noticeable deviations from the standard T_I kernel, $1 - e^{-\frac{T_w}{T_1}}$. Taking the case where $T_w = T_I = 0.01$ as an example, the simulated echoes are clearly much larger than 1% of the largest echo, which is the expected on-resonance behavior. Instead, the results follow the general form of Eq. 11 with offset terms ε that are in good quantitative agreement with the analytical results derived in section 2.1. Table A.1 lists the calculated values for α_1 and α_2 based on Eqs. 14 and 15 using the appropriate weighting functions $g(\omega_0)$ for the two types of methods used for amplitude extraction (see Figure B.2). The corresponding predictions for the T1 kernel from Eq. 11 and Eq. 13 are shown as solid lines on the right hand column of Fig. 5. As expected, the deviations between the general and standard T1 kernels are significantly larger for echo peak detection compared to matched filtering. This is caused by the increased off-resonance contributions in $g(\omega_0)$ for peak detection, as is clearly evident in Figure B.2. For the rest of the paper, we will limit ourselves to amplitudes extracted by matched filtering.

Phase Alternation of Excitation Pulse and Impact on $\square\square$

It is desirable to minimize the offset parameter ε . This can be partially accomplished by alternating the relative phase difference between the excitation and refocusing pulses of the first and second

CPMG sequence from $+90^\circ$ to -90° (see Figure B.1). This is demonstrated by the results of the numerical simulations shown in *Figure B.6*. When phase alternation (PA) is enabled (middle column of Figure B.6), the echo amplitudes at short wait time are greatly reduced for short durations of the first CPMG sequence. However, this PA effect vanishes as $N_1 t_E = T_2$ increases.

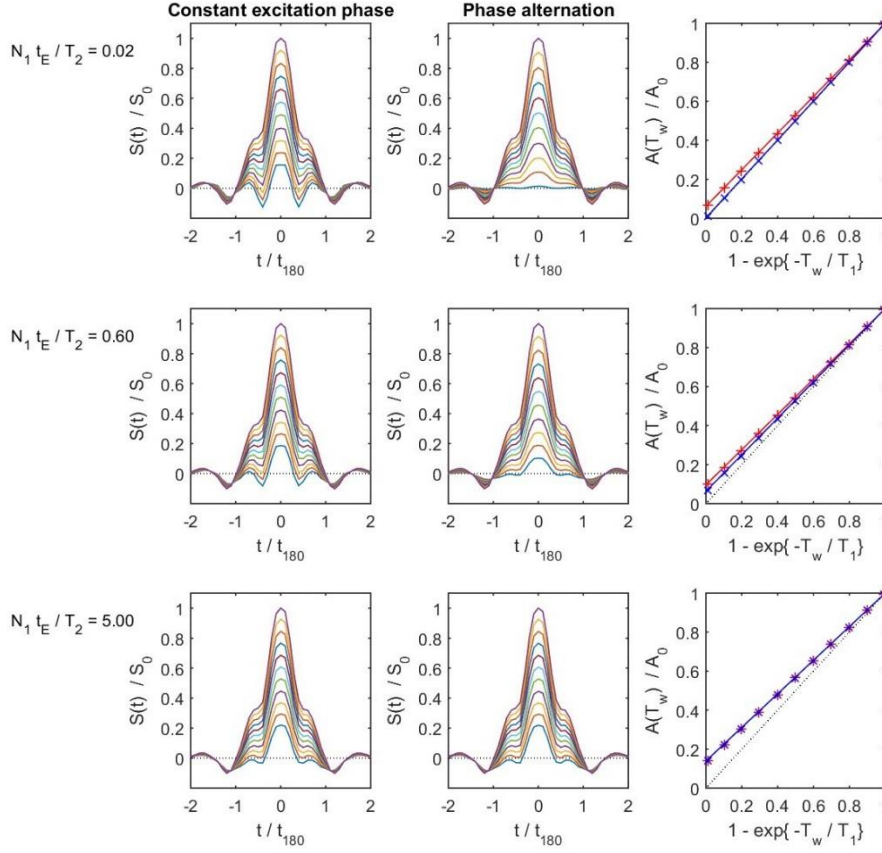


Figure B.6: Effect of phase alternation (PA) on echo shapes and amplitudes. The two left columns show simulated echo shapes without PA (left) and with PA (middle) for a range of $T_w = T_1$ ratio between 0.01 to 5.00. The rows correspond to different durations of the first CPMG sequence, $N_1 t_E = T_2$, as listed on the left. The right column compares the extracted amplitudes with PA (black) and without PA (red). Matched filtering was assumed. The symbols show the results of the numerical simulations, while the solid lines show Eq. 11 with values of ε determined by Eq. 13 with the values of α_1 and α_2 listed in Table A.2.

In terms of the theoretical description of section 2.1, PA reduces the value of α_1 , but leaves α_2 unaffected. This can be understood as follows: The profile of M_z for small values of N_{1TE}/T_2 (Figure B.3) and the profile of $g(\omega_0)$ (Figure B.2) are not fully symmetric with respect to ω_0 . The M_z profile is inverted with respect to ω_0 when the phase of the excitation pulse of the first CPMG sequence is inverted, while the profile of $g(\omega_0)$ is inverted when the phase in the second CPMG sequence is inverted. If the phases in both sequences are identical, the resulting offset parameters are given in Table A.1. If instead the phases are alternated, the evaluation of Eq. 14 with an inverted profile of M_z results in a greatly reduced value of α_1 , as shown in Table A.2. In the dynamic equilibrium regime, M_z is symmetric with respect to ω_0 and is not affected by the initial excitation pulse of the CPMG. Therefore, PA does not have any effect on α_2 . This observed near-cancellation of α_1 with PA occurs in gradient B_0 fields, but it is not guaranteed to be as effective with other field profiles when the different offset frequencies are not equally weighted.

Table B.2: Effect of phase alternation of excitation pulse on the calculated values of α_1 and α_2 . In both cases, amplitude extraction based on matched filtering is assumed.

Phases of Excitation Pulses	α_1	α_2
Identical Phase	0.06	0.14
Phase Alternation	< 0.01	0.14

Dependence of ε on the ratio T_1/T_2

The longitudinal magnetization at the end of the CPMG sequence is also affected by the ratio T_1/T_2 , especially when the initial CPMG sequence is long. This is illustrated in Figure B.7 that displays the spectrum of the longitudinal magnetization for different values of T_1 / T_2 . In this case, the longitudinal magnetization is saturated over a larger range of offset frequencies for large T_1 / T_2

ratios compared to $T_1 / T_2 = 1$. This is most pronounced when $N_{1TE} / T_2 > 1$ and the magnetization is controlled by the dynamic equilibrium regime. For shorter initial CPMG sequences when the CPMG and CP terms dominate, the dependence on T_1/T_2 disappears.

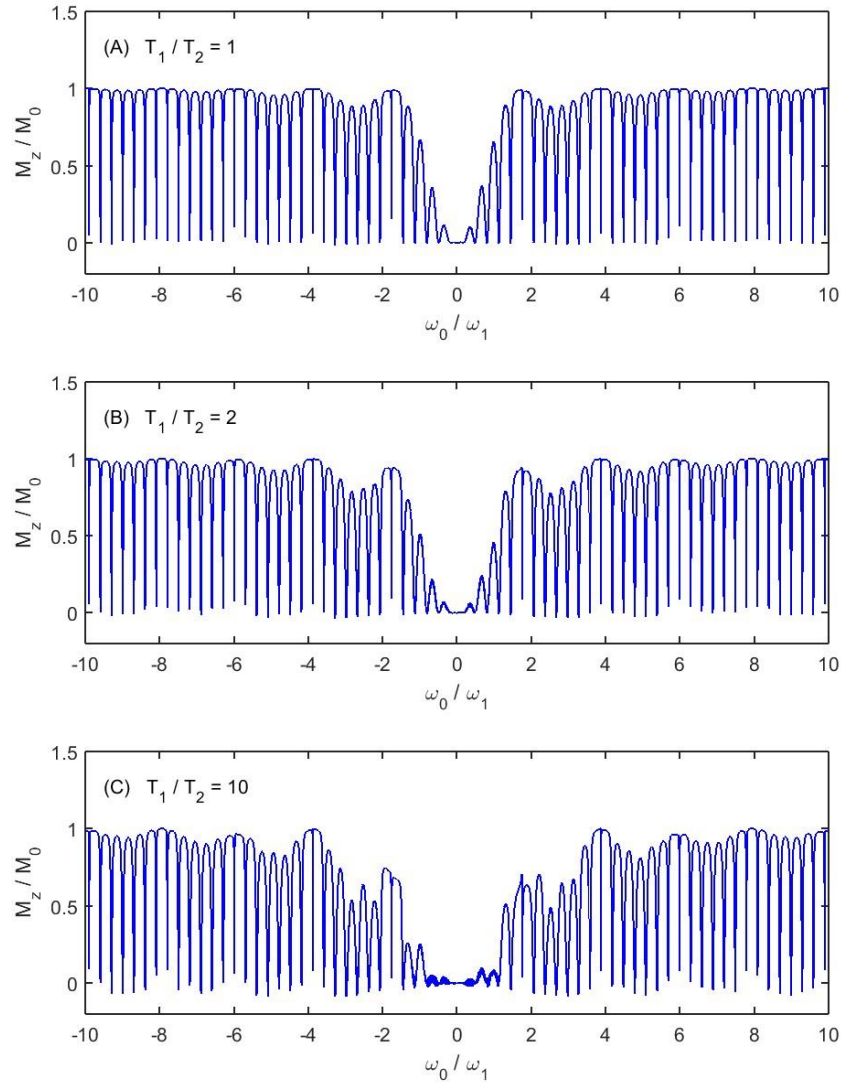


Figure B.7: Spectra of normalized longitudinal magnetization at the end of first CPMG sequence for different T_1/T_2 ratio as indicated. For all cases, $N_{1TE}/T_2 = 5$ (i.e., long initial CPMG sequence) was employed.

Given that for large T_1/T_2 ratios there is a wider range of frequencies ω_0 with significantly suppressed M_z , we expect ϵ to decrease with increasing values of T_1/T_2 . This is confirmed by the

results in Figure B.8 showing the dependence of the signal offset ϵ on $T_1 = T_2$ for the case of a long first CPMG sequence, $N_{1TE} / T_2 = 5$.

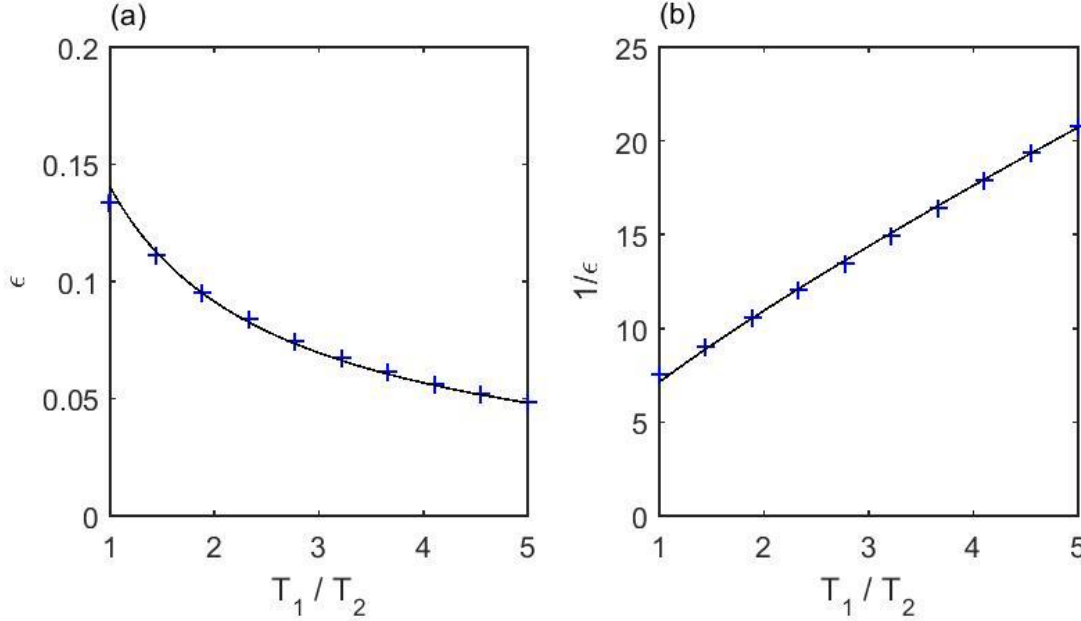


Figure B.8: Dependence of ϵ and $1/\epsilon$ on T_1/T_2 . Panel a: Dependence of signal offset ϵ on the ratio of T_1/T_2 for the ratio of $N_{1TE}/T_2=5$ and assuming matched filtering. The symbols show the results of the numerical simulations, while the line shows the evaluation of Eq. 12. Panel b: Dependence of $1/\epsilon$ versus T_1/T_2 . This panel displays the same data as shown in panel a. The near linear dependence of $1/\epsilon$ on T_1/T_2 confirms the general form of Eq. 17 and allows the extraction of $\eta = 0.56$.

The expression Eq. 17 of ϵ for a long initial CPMG sequence (i.e. $N_{1TE}/T_2 \gg 1$) reduces to " $\epsilon =$

$\frac{a_2}{\eta + (1-\eta)T_1/T_2}$. This predicts a linear dependence of $1/\epsilon$ on T_1/T_2 . This is tested in *Figure B.8b*. By

fitting the results to a straight line, the parameter $\eta = 0.56$ can be extracted. As for the previous parameters a_1 and a_2 listed in Table B.2, this parameter was obtained using the method of matched filtering for amplitude extraction.

Figure B.9 compares the analytical results with simulations for a range of different conditions. The simulations assume a B_0 field with a constant gradient, phase alternation in the phase of the

excitation pulses, and amplitude extraction by matched filtering. The analytical results follow Eq.

11 with $\epsilon \approx \frac{0.14}{0.56+0.44\frac{T_1}{T_2}} (1 - e^{-N_1 t_E/T_2})$. There is excellent agreement between simulation and

analytical results without any adjustable parameters. This demonstrates that in inhomogeneous field, the conventional T_1 kernel only approximates the response for short CPMG durations (assuming PA is used) or in systems with large T_1/T_2 ratios.

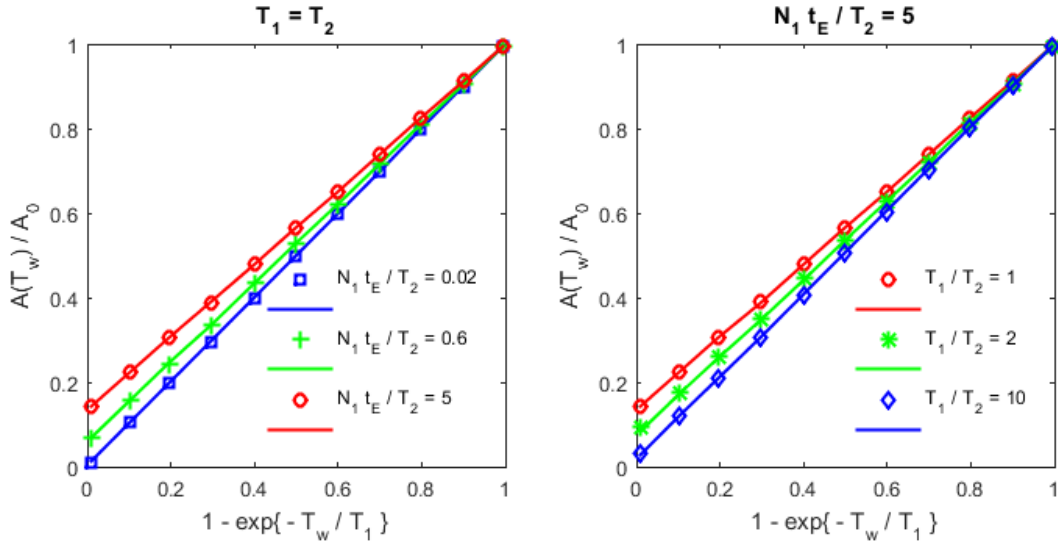


Figure B.9: Evaluation of the proposed new T_1 kernel (Equations 11 and 17) for various values of N_{1tE}/T_2 (Panel a) and T_1/T_2 (Panel b) in the presence of significant off-resonant effect. The markers show the results of the numerical simulation. The solid lines show the analytical results of the modified kernel with $\alpha_1 = 0$, $\alpha_2 = 0.14$, and $\eta = 0.56$.

B.5.2 Experimental Results

To validate the proposed T_1 saturation recovery kernel in the presence of off- resonance effect, we also performed a series of experiments for three samples with contrasting relaxation properties: deionized (DI) water, NiCl_2 -doped water, and skim milk. The measured relaxation times as measured by standard inversion recovery and CPMG sequences in uniform field are given in Table A.3. For fully relaxed samples ($T_w \gg T_1$), the measured asymptotic echo shapes for all samples

were identical, as expected. Taking the doped water as an example, Figure B.10 compares the echo shapes between simulation and experiments. Despite the unavoidable imperfections in the experiments (e.g. B_1 inhomogeneity and diffusion) excellent agreements were found between simulation and experiment.

Table B.3: Experimentally determined relaxation times for the three samples

Sample	DI water	Doped eater	Skim milk
T_1 [s]	2.44	0.30	1.56
T_2 [2]	2.18	0.28	0.17

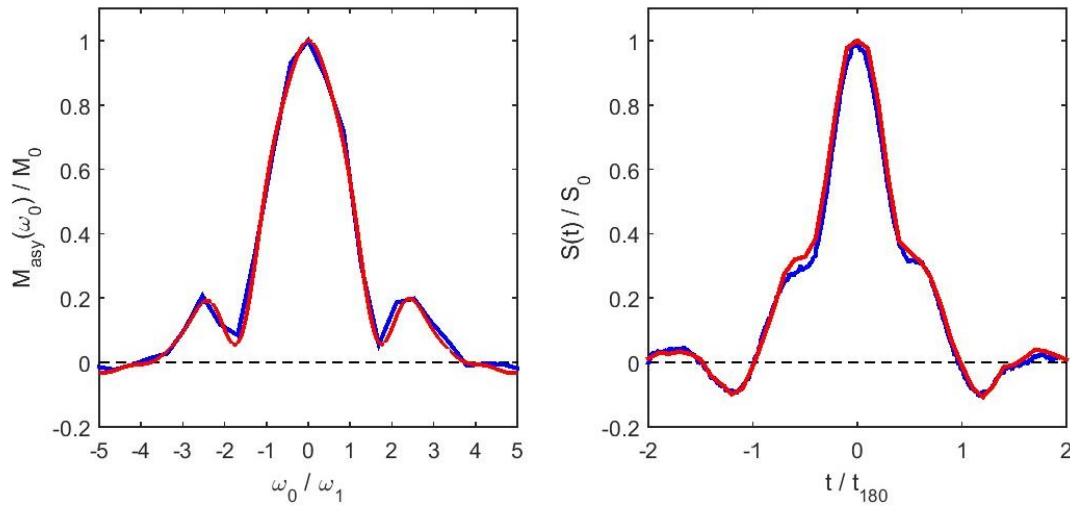


Figure B.10: Comparison between experimentally measured and numerically simulated echoes for both frequency domain (left panel) and time domain (right panel). The frequency is normalized with respect to ω_1 , and the time is normalized with respect to t_{180} . For both panels, the measured echoes are shown in blue, and the simulated echoes are shown in red. The agreement between experiment and simulation is excellent.

Figure B.11 shows both the measured echo shapes and the extracted echo amplitudes (using matched filtering) for doped water as a function of wait time. In these measurements, the first CPMG was long, consisting of 104 echoes that corresponds to $N_1 t_E / T_2 = 5:5$. Even though the echoes of the first CPMG have fully decayed, the application of a second CPMG almost immediately after the first CPMG generates sizeable echoes with a peak that is around 20% of the echo peak for the fully recovered case. As the wait time T_w increases, the amplitude of the echoes also increases until they saturate when the wait time is long compared with T_1 . The amplitudes show a linear dependence on $1 - e^{-T_w/T_1}$ with an offset ϵ that is in quantitative agreement with the theoretical expectations.

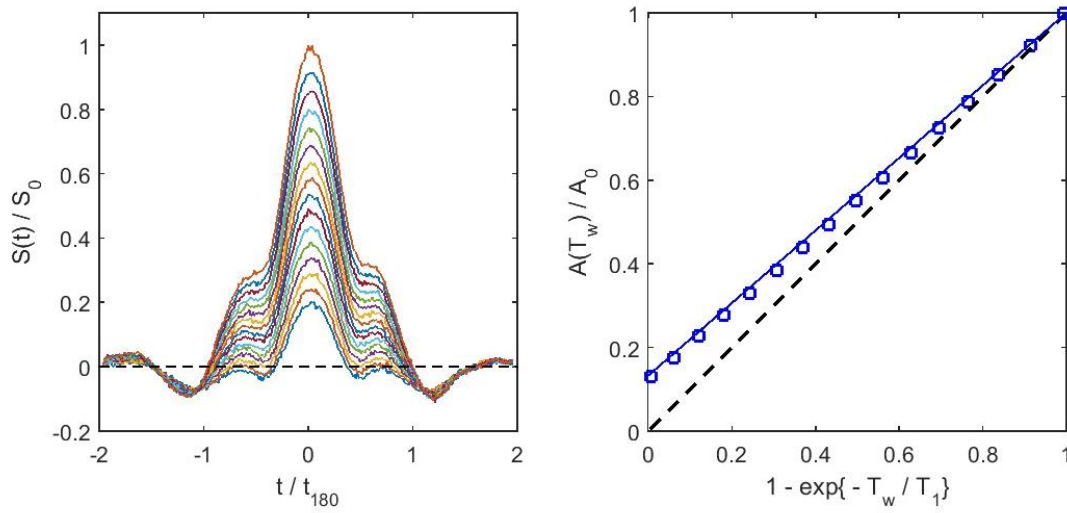


Figure B.11: Experimental results for standard saturation-recovery measurement for doped water: measured in-phase components of echoes (left) and extracted echo amplitude using matched filtering (right) for different recovery wait time T_w (T_w/T_1 in the range of 0.01 to 5). The blue line shows the expected behavior based on Eq. 11, whereas the dashed line shows the standard T_1 kernel (i.e. $\epsilon = 0$).

The measured effect of phase alternation is shown in Figure B.12. Phase alternation does not change the overall amplitude of the remaining M_z at the end of the first CPMG sequence, but rather it changes the impact on the echoes generated by the second CPMG sequence. When the saturating CPMG sequence is short ($N_1 t_E / T_2 < 1$), the resulting remnant M_z at the end of this sequence has both positive and negative amplitudes. With PA the second CPMG sequence effectively averages out the contributions from the remnant M_z magnetization, leading to vanishingly small amplitudes, whereas without PA, the contributions add more coherently. For long initial CPMG sequences, the remnant M_z magnetization is all positive and symmetric with respect to offset frequency. In this case, the measured response for PA and without PA are identical. The experimental results shown in Figure B.12 confirm not only this overall behavior, but the echo shapes show good quantitative agreement with the theoretical expectations.

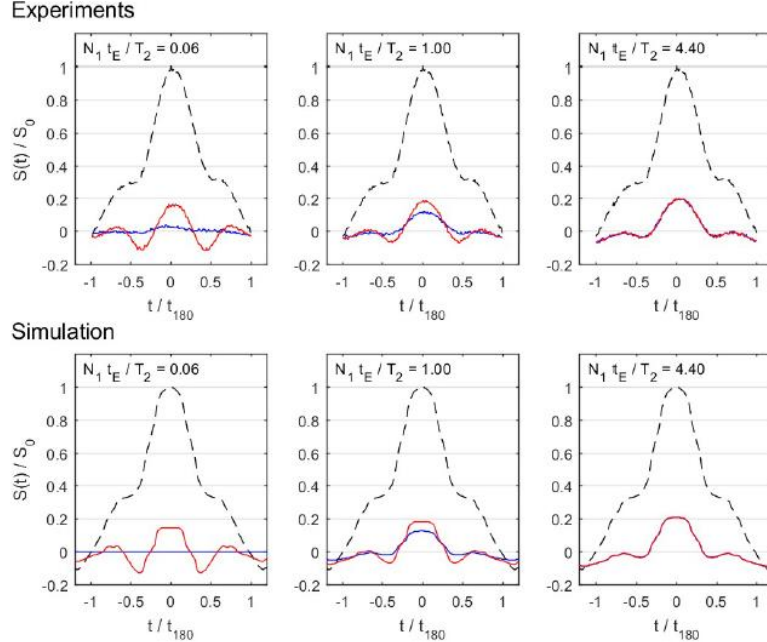


Figure B.12: The effect of phase alternation (PA) on the shape of the echoes at short wait times. Results are shown for $T_w/T_1 = 0.01$ and for three different CPMG lengths as indicated. The top panels show experimental results, the bottom panels show simulations. In each panel, the results with PA are shown in blue and without PA in red. As a reference, we also include the echo shape acquired at long wait time (i.e., $T_w/T_1 = 5$).

Figure B.13 shows a summary of the extracted amplitudes from the measurements on all three samples. In these cases, the duration of the initial CPMG sequence was always long compared to T_2 of the respective sample: $N_1 t_E / T_2 = 5.50$ for DI water, 4.3 for doped water, and 7.1 for the skim milk, respectively. The experimental results confirm the predictions that the T_1 kernel in inhomogeneous fields deviates from the standard form $1 - e^{-T_w/T_1}$ and has instead the general form of Eq. 11. As predicted, the offset parameter ϵ depends on the ratio of T_1 / T_2 , but not on the absolute value of these relaxation times. There is excellent quantitative agreement with the generalized kernel and the offset parameter given by Eq. 17.

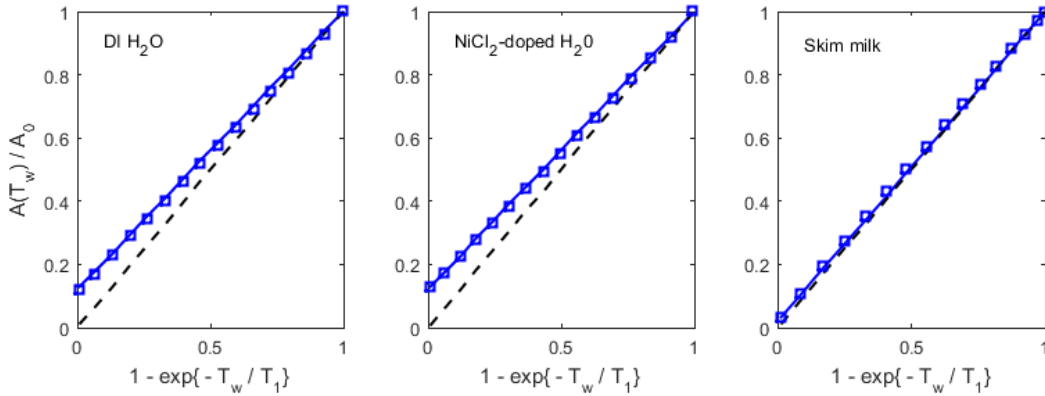


Figure B.13: Saturation recovery measurements for DI H_2O , $NiCl_2$ -doped H_2O , and skim milk. For all panels, blue squares represent the measured amplitudes, while the dashed black line and the blue line indicate the standard and modified saturation recovery kernel, respectively. "Ground truth" T_1 and T_2 for all samples were measured in advance without any gradient using standard inversion-recovery and CPMG sequences. These values were then used in the plotting of both standard and modified kernels.

B.6 Discussion and Conclusions

We have shown that the effect of inhomogeneous fields on saturation – recovery measurements can be quantitatively described by the modified T_1 kernel of Eq. 11 that includes the offset parameter. This offset parameter is a function of the field configuration, the relative duration of

the saturating CPMG sequence, and the T_1 / T_2 ratio. These dependencies can be characterized by the three parameters T_1 , T_2 , and η as given in Eq. 17. These parameters are specific for a given experimental configuration and we give explicit expressions for them. For the case of a gradient field and PA, the parameters are calculated to be $\alpha_1 = 0$, $\alpha_2 = 0.14$, and $\eta = 0.56$. We have used numerical simulations and experiments to confirm these analytical results.

Using a relatively short CPMG as the saturating sequence (e.g., $N_{1TE} / T_2 < 0.02$), the spectrum of M_z has both positive and negative components and the effect of incomplete saturation can then be effectively cancelled by alternating the phase of 90° pulse between the saturating and detecting CPMG sequence (Figure B.6 and Figure B.12). When the effective length of the saturating CPMG sequence is long compared with the relaxation time, a dynamic equilibrium state develops. The resulting steady state longitudinal magnetization M_z is then always positive and does not depend on the initial 90° saturation pulse. In this case, PA does not change the offset signal for a relative longer CPMG sequence as shown in Figure A.6 and A.12. Instead, it depends on the ratio of T_1 / T_2 , and drops as the ratio increases.

It is worthwhile to point out that, in theory, the off-resonance effect could be eliminated by using a large acquisition time window (e.g. $T_{acq} > 5 \times t_{180}$) for each CPMG echo, and integrating the time domain echo as the saturation recovery signal. This is essentially equivalent to taking the nominal center amplitude of the frequency spectrum (i.e., $\omega_0 = 0$), and exclude all of the off-resonance contributions. However, this approach is impractical and undesirable for at least two reasons, both related to the generally low signal to noise ratio (SNR) of stray field NMR measurements. First, the echo amplitude extracted by integration of the noisy signal over a long acquisition time results in a much lower SNR compared to an extraction based on matched

filtering. Second, it is typically necessary to further average or equivalently filter a large number of adjacent CPMG echo amplitudes in order to achieve adequate SNR. However, an increase in the acquisition time leads to an increase in the minimum echo spacing. This reduces the number of available echoes per unit time and thus further reduces the achievable SNR.

It is straightforward to extend the current analysis to more complicated field configurations and take B_1 distributions into account. The basic form of the modified kernel is unaffected, but the values of the three parameters α_1 , α_2 , and η will change. For example, for the logging tools described by Kleinberg et al. [17], the value of α_2 was found to be $\alpha_2 = 0.18$. This is a relative modest increase from $\alpha_2 = 0.14$ found for the case of a constant gradient B_0 and constant B_1 .

As an alternative to incorporating the contribution of off-resonance in the T_1 saturation recovery kernel, one could also attempt to minimize its contribution by applying a number of 'crusher' pulses at the end each CPMG saturation sequence. These crusher pulses are used to scramble the remnant M_z at the end of the saturation CPMG such that the incomplete saturation does not contribute to the signal generated by the following CPMG sequence. Further discussion and the optimization of such crusher pulses will be presented elsewhere.

In conclusion, we have analyzed T_1 saturation recovery measurements in grossly inhomogeneous fields. We have shown that, in these conditions, the off-resonance effect produces extra signal in the measurement. Using the standard T_1 kernel, this extra signal will be misinterpreted as a pseudo-fast longitudinal relaxation. We have derived a modified kernel that takes into account the off-resonance contributions. This modified kernel successfully describes the saturation-recovery experiments for a wide variety of parameters. Excellent agreement was found between analytical results, numerical simulations, and experiments.

B.7 References

1. F. Casanova, J. Perlo, B. Blumich (Eds.), *Single-Sided NMR*, Springer, 2011.
2. M. D. Hurlimann, N. J. Heaton, *NMR Well Logging*, in: *Mobile NMR and MRI: Developments and Applications*, Royal Society of Chemistry, 2015, pp.11-85.
3. H. Y. Carr, E. M. Purcell, Effects of diffusion on free precession in nuclear magnetic resonance experiments, *Phys. Rev.* 94 (1954) 630-638.
4. S. Meiboom, D. Gill, Modified spin-echo method for measuring nuclear relaxation times, *Rev. Scientific Instruments* 29 (1958) 688-691.
5. M. N. Miller, Z. Paltiel, M. E. Gillen, J. Granot, J. Bouton, Spin echo magnetic resonance logging: Porosity and free uid index determination, in: *Trans. SPE Annual Technical Conference and Exhibition*, (1990), p. SPE 20561.
6. G. Goelman, M. G. Prammer, The CPMG pulse sequence in strong magnetic field gradients with applications to oil-well logging, *Journal of Magnetic Resonance, Series A* 113 (1995) 11-18.
7. M. D. Hurlimann, D. D. Griffin, Spin dynamics of Carr Purcell Meiboom Gill -like sequences in grossly inhomogeneous B₀ and B₁ fields and application to NMR well logging, *Journal of Magnetic Resonance* 143 (2000) 120-135.
8. R. L. Kleinberg, Methods in the physics of porous media, nuclear magnetic resonance, in: *Experimental Methods in the Physical Sciences*, volume 35, Academic Press, 1999, pp. 337-385.
9. Y.-Q. Song, L. Venkatarmanan, M. D. Hurlimann, M. Flaum, P. Frulla, C. Straley, T₁-T₂ correlation spectra obtained using a fast two-dimensional Laplace inversion, *Journal of Magnetic Resonance* 154 (2002) 261-268.
10. M. D. Hurlimann, L. Venkataramanan, Quantitative measurement of two dimensional distribution functions of di_usion and relaxation in grossly inhomogeneous fields, *Journal of Magnetic Resonance* 157 (2002) 31-42.
11. A. E. Ozen, R. F. Sigal, T₁/T₂ NMR surface relaxation ratio for hydrocarbons and brines in contact with mature organic - shale reservoir rocks, *Petrophysics* 54 (2013) 11-19.

12. R. Kausik, K. Fellah, E. Rylander, P. M. Singer, R. E. Lewis, S. M. Sinclair, NMR relaxometry in shale and implications for logging, *Petrophysics* 57 (2016) 339-350.
13. B. Nicot, N. Vorapalawut, B. Rousseau, L. F. Madariaga, G. Hamon, J.-P. Korb, Estimating Saturations in Organic Shales Using 2d NMR, *Petrophysics* 57 (2016) 19-29.
14. M. Fleury, M.-F. Romero-Sarmiento, Characterization of shales using T1-T2 NMR maps, *J. Petroleum Science and Engineering* 137 (2016) 55-62.
15. M. D. Hurlimann, Diffusion and Relaxation Effects in General Stray Field NMR Experiments, *Journal of Magnetic Resonance* 148 (2001) 367-378.
16. M. D. Hurlimann, Optimization of timing in the Carr - Purcell - Meiboom - Gill sequence, *Magnetic Resonance Imaging* 19 (2001) 375-378.
17. R. L. Kleinberg, A. Sezginer, D. D. Griffin, M. Fukuhara, Novel NMR apparatus for investigating an external sample, *Journal of Magnetic Resonance* 97 (1992) 466-485.